

University of Alberta

RESERVOIR-ON-A-CHIP (ROC)

by

Bijoyendra Bera

A thesis submitted to the Faculty of Graduate Studies and Research
in partial fulfillment of the requirements for the degree of

Master of Science

Department of Mechanical Engineering

©Bijoyendra Bera

Fall 2011

Edmonton, Alberta

Permission is hereby granted to the University of Alberta Libraries to reproduce single copies of this thesis and to lend or sell such copies for private, scholarly or scientific research purposes only. Where the thesis is converted to, or otherwise made available in digital form, the University of Alberta will advise potential users of the thesis of these terms.

The author reserves all other publication and other rights in association with the copyright in the thesis and, except as herein before provided, neither the thesis nor any substantial portion thereof may be printed or otherwise reproduced in any material form whatsoever without the author's prior written permission.

To my parents

Abstract

This current work investigates pore structure of various reservoir-rock materials using state-of-the-art microscopy such as micro-computed tomography (micro-CT) and Focused Ion Beam-Scanning electron Microscopy (FIB-SEM). Novel sample preparation methods have been developed for such rock cores, in order to characterize and quantify the complex pore space. The evolution of the pores inside such a reservoir is captured, from nanometre to micron-scale pores. Based on the analysis, realistic pore networks have been designed, with varying pore connectivity and pore size, to resemble such oil-reservoirs to greater detail. Fabrication of this network has been achieved in silicon and quartz substrates, and design of microfluidic connectors have been performed for creating a complete microfluidic device. Thus, an entire section of an oil-reservoir has been miniaturized to the lab-scale and the device has been termed 'Reservoir-on-a-Chip' (ROC). Waterflooding experiments are performed in ROC along with preparation of recovery-curve.

Keywords: Enhanced Oil Recovery, Rock-core, oil-displacement, micro-CT, FIB-SEM, Pore network, Fabrication, Chip, Waterflooding, Recovery-curve

Acknowledgements

First, I would like to thank my supervisor, Dr. Sushanta K. Mitra for his guidance and encouragement during this work. He has not only introduced me to the research world, but infused me with an outlook and work-ethic, which I would be able to carry with me for my entire life. His technical inputs and thorough understanding of the discipline saw me through countless times, and his belief in me in difficult times has made it possible to complete this work. It has been a privilege to be able to learn from him, and work with him.

Without Dr. Douglas Vick's (National Institute of Nanotechnology, NRC) expertise and guidance in each step of characterization techniques, the work would never have started. I owe many thanks to Nikolaos K. Karadimitriou and Prof. S. Majid Hassanizadeh (Universiteit Utrecht, The Netherlands) for providing me with the design of pore network. I am grateful to Dr. David Moon (TIMP Laboratory, University of Calgary) for his crucial comments regarding micro-CT on Berea sandstone.

I am grateful to all the researchers and technical support staff at NRC facility, Nanofab and Mechanical Engineering Department workshop, University of Alberta especially Daniel Salomon and Martin Kupsta at NRC and Roger Merchand and Daniel Mooney at Mechanical workshop. A very special vote of thanks to Scott Munro at Nanofab, without whom the fabrication would never be done.

I am indebted to Naga Siva Kumar Gunda at MNT Lab, friend and col-

league, for being a great source of help during the last two years. Any future motivation to work as an experimental researcher on my part has been seeded by him. Prashant R Waghmare at MNT Lab has been the other great source of help, and it has been a nice opportunity to get to know him as a friend.

A special vote of thanks to Mehdi Rezaei Saray and Ryan Saunders at Advanced MEMS Design Lab, for always being patient with my enquiries and helping me out on many occasions, starting from lab supplies to technical drawing. Akshay Gunde at MNT Lab has been a great friend and colleague, the last two years have been least boring at work because of the fun moments shared with him. Other colleagues, especially Reeshav Chatterjee and Satya Sai Gajapathi, have made my work experience in these years a memorable chapter.

Last, and perhaps most importantly, thanks to my parents. They have made me realize that true source of inspiration can overcome the barriers of physical distance, in work and in life.

Contents

1	Introduction	1
1.1	Motivation	1
1.2	Problem Definition	2
1.3	Thesis Overview	3
1.3.1	Objective: Conceptual Map of Reservoir-on-a-Chip/ROC	3
1.3.2	Thesis Outline	3
2	Literature Review	6
2.1	Secondary and Tertiary Oil-Recovery	6
2.2	Characterization of Reservoir-rock Specimen	8
2.2.1	Micro-CT Images	9
2.2.2	Focused Ion Beam-Scanning Electron Microscopy (FIB-SEM)	10
2.3	Pore Network Model	12
2.4	Microfabrication of Porous Media and Experimentation	14
3	Characterization of reservoir rock: Berea sandstone ¹	17
3.1	Micro-CT on Berea	17
3.1.1	Materials: Sample Preparation	17
3.1.2	X-ray Imaging Method	18
3.1.3	Results	19
3.2	Focused Ion Beam on Berea	21
3.2.1	Materials: Sample Preparation	21
3.2.2	FIB-SEM: Internal Microstructure Imaging	22
3.2.3	Results of FIB-SEM	23
3.3	Three-Dimensional Reconstruction	23

¹Parts of this chapter have been compiled from the publication in *Micron*, 2011, **42** pp. 412-418

3.4	Concluding Remarks	29
4	Numerical Investigation of waterflooding using micro-CT images of Berea Sandstone core by Finite Element Method ²	32
4.1	Micro-CT Images	32
4.2	Image Processing	33
4.3	Numerical Simulation	34
4.3.1	Geometry of Porous Medium	34
4.3.2	Governing Equations	34
4.3.3	Boundary and Initial Conditions	38
4.3.4	Solution Technique	39
4.4	Results and Discussion	39
4.4.1	Validation of Numerical Model	40
4.4.2	Two-phase Flow: Waterflooding	43
4.5	Concluding Remarks	43
5	Characterization of nanometer scale pore structure in reservoir rock: Carbonate rock ³	46
5.1	FIB-SEM on Dolomitic Limestone	46
5.1.1	Material and Sample Preparation	46
5.1.2	Serial Sectioning of Region A	47
5.1.3	Results: Region A	52
5.1.4	Serial Sectioning of Region B	52
5.1.5	Results: Region B	55
5.2	Three-Dimensional Reconstruction	55
5.3	Characterization and Discussion	57
5.4	Concluding Remarks	60
6	Fabrication of pore-network structures in silicon and quartz substrates ⁴	62
6.1	Experimental Details	62
6.1.1	Pore-network Design	62

²Parts of this chapter have been compiled from the publication in *Energy*, 2010, **35** pp. 5209-5216

³Parts of this chapter have been compiled from the publication in *Journal of Microscopy and Microanalysis*, Paper # MAM-11-083, July 2011, *Under Review*.

⁴Parts of this chapter have been compiled from the publication in *Journal of Micromechanics and Microengineering*, Paper # JMM/394050/PAP/166956, May 2011, *Under Review*.

6.1.2	Materials and Fabrication Equipment	66
6.1.3	Silicon Micro-model Fabrication	67
6.1.4	Quartz Micro-model Fabrication	68
6.1.5	Drilling Holes for Inlet and Outlet Fluidic Ports	69
6.1.6	Bonding of Micro-models	69
6.2	Characterization and Discussion	70
6.3	Concluding Remarks	79
7	Reservoir-on-a-Chip: Waterflooding experiments ⁵	82
7.1	Realization of Reservoir-on-a-Chip (ROC)	82
7.2	Experimental Section	83
7.2.1	Waterflooding Experiments	83
7.3	Experimental Results	86
7.4	Concluding Remarks	87
8	Conclusions and Future Work	92
	References	104

⁵Parts of this chapter have been compiled from the publication in *Lab on a Chip*, Paper # LC-ART-06-2011-020556, June 2011, *Under Review*.

List of Tables

3.1	Pore Body Characteristics of the three reconstructed microstructures	28
4.1	Properties of fluids	40
4.2	Average velocities at boundaries for single-phase flow	40
6.1	Surface profile parameters of fabricated networks on silicon and quartz	77

List of Figures

3.1	Berea sandstone core	18
3.2	Micro CT on Berea sandstone sample (a) micro-CT image, distribution of the solid and void structures represented by black and white colors, respectively, inset shows an enlarged solid-void structure distribution. (b) Typically, large void structures (crater-like shapes) of size greater than $100\ \mu\text{m}$ (bottom inset) co-exist with the relatively small size pores of average size, ranging from $30\text{-}40\ \mu\text{m}$ to $70\text{-}80\ \mu\text{m}$ (top inset).	20
3.3	Misleading small-scale grains (caused by surface roughness, detector noise, and X-ray scattering effects) in the image suggest the presence of pores in the order of $3\text{-}5\ \mu\text{m}$, arrows point out reduced effective diameter.	21
3.4	FIB-SEM on Berea sandstone (a) Schematic of a standard Focused Ion Beam (FIB) set-up(b) specific arrangement of the ZEISS N-Vision 40 Crossbeam Workstation for the Berea specimen with the stage at 54°	22
3.5	FIB on Berea solid matrix (a) a single trapezoidal-shaped trench milled to depth $10\ \mu\text{m}$ (top right inset shows resultant trapezoid). (b) solid silica matrix after FIB milling without any presence of micro-pores (voids) (c) matrix surrounded by crater-like shapes and relatively smaller pores. Smaller pore structures are not readily noticed in this solid matrix after the first milling	24

3.6	Results: FIB on Berea sandstone (a) further milling on all the sides of the trapezoidal structure reveals a very thin section (inset on top left depicts the removal of material from three directions), absence of any micro-pores inside the matrix is evident (b)void structures present in interconnected network outside the solid matrices of silica, the larger structures (craters A) being 100-250 μm in size interwoven with solid matrix (B) and smaller void structures (C) of size 30-40 μm	25
3.7	Pore structure obtained from CT images using Avizo Fire 6.3 with (a) threshold value 200 and porosity 25.63%; (b) threshold value 206 and porosity 21.8%; (c) threshold value 220 and porosity 16.43 %	27
3.8	Three different cross-sectional views of the 3D reconstructed microstructure (Recon1, with thresholding value of 200), with XY, YZ and ZX sections at 1.52 mm, 1.52 mm and 0.4 mm, respectively	29
3.9	Variation of number of pore with the microstructure volume for 3D reconstructed microstructures	30
4.1	An image representing cross-sectional porous structure at an axial distance of 0.378 <i>mm</i> from the base was selected for the numerical analysis. The image depicts the porous structure using a range of pixel values. Black coloured regions represent solid grains and white coloured regions show pore space. . . .	33
4.2	(a) Pore structure obtained after image processing. White region represents solid grains while black region represents pore space. (b) The same image has been imported into COMSOL and an unstructured two-dimensional mesh is generated in the problem domain.	35
4.3	The representative computational geometries used for COMSOL simulations. All dimensions are in meters	36
4.4	Variation of velocity magnitude in the flow field depicted by a range of colours from Blue to Red. Blue regions represent low velocities while Red regions represent high velocities (in m/s) .	41

4.5	The variation of volume flow rate with the applied pressure gradient. Linear relationship observed in the graph validates Darcy's law. The value of absolute permeability calculated from the graph is 1.172 mD	42
4.6	Invasion of water in the pores at different time instants resulting in the displacement of oil.	44
4.7	Variation of volume of oil displaced by water with time in the pore spaces.	45
5.1	(a) Carbonate dolomitic limestone rock core (b) The carbonate rock specimen placed on a 45 ⁰ mount inside the FIB-SEM vacuum chamber.	48
5.2	Preparation of Region for FIB (a) Region A (rectangular peninsula), after material is removed from three sides by ion milling (b) Further ion polishing on the three sides of the site producing undercut at the bottom of the front section of Region A. . . .	50
5.3	(a) The front face of Region A after final polishing, with various pores and cracks visible (ranging from a few hundred nms to a few μ ms in size); inset figures show some of the nm-scale pores at higher magnifications. (b) Deposition of a sacrificial layer of platinum on the top surface, with fiduciary marks milled into the top of Region A.	51
5.4	Sample images obtained during FIB milling of Region A. (a) Pores revealed by serial sectioning (via ion milling) to a distance of 560 nm from the original front surface of Region A. Inset figures highlight the presence of submicrometre-scale pores and crack structures (on the order of a few hundred nanometres in size). (b) Pores revealed at 1260 nm from the original front surface, with insets highlighting nanometre-scale pores and submicrometre-scale cracks.	53
5.5	Preparation and sample images of Region B. (a) Region B, chosen 30 μ m below the surface of the specimen where a bulk pore was adjacent to the solid matrix. (b) Sacrificial Pt layer deposited on the top surface of this site along with fiduciary marks (as in Region A).	54

5.6	(a) Pores revealed by ion milling at a distance of 2.80 μm inward from the front surface, some of which are found to connect with the bulk pore located next to Region B. Insets show magnified views of nm- and μm -scale pores in the vicinity. (b) The image obtained at 5.1 μm inward from the front surface reveals various pores (2-3 μm in size) connecting with each other and also joining with the bulk pore on the outside surface. The inset shows a magnified view of some of the nanometre-scale pores.	56
5.7	Reconstruction of the pore spaces for Region B of the carbonate sample. (a) A reconstruction of the solid matrix of Region B (inverted from the views presented in Figure 5.6). (b) A reconstruction of the pore spaces in the same region (inverted view), with dead pores highlighted. Nm-scale and micrometre-scale pores are present in large numbers, and the connectivity of many of the pores with the outside bulk-pore is readily observable.	58
5.8	Nm-scale pores found to connect with μm -scale pores and then with the bulk pore outside the solid matrix; the colours in the figure depict the individual pore volumes	59
5.9	The variation of the number of pores with individual pore volume for the 3D reconstructed pore space	60
6.1	Design of a representative pore-network, with inlet and outlet regions and separate entrance and exit regions	64
6.2	Pores, throats and pore-throat connectivity in different networks (a) Network 1 (b) Network 2 (c) Network 3 (d) Network 4	65
6.3	Micromodels fabricated in (a) silicon (with covering layer of glass) (b) quartz (before bonding with the covering layer) . . .	70
6.4	SEM images of different networks etched on silicon; (a) Network 1; (b) enlarged view of pores and throats on etched silicon networks	71
6.5	SEM images of different networks etched on silicon; (a) Network 2; and (b) Network 3	73

6.6	SEM characterisation of vertical wall-profiles in silicon network micro-model; (a) near-vertical wall-profile obtained in network, fabricated on silicon (b) contour profile of wall in an isolated solid matrix	74
6.7	Entrance region of Fabricated network: Starting location of Network 2 from the inlet side	75
6.8	SEM images of etched quartz micro-model; (a) Network 1 etched on quartz; (b) enlarged view of Network 1 in SEM; (c) feature sizes measured for Network 1	76
6.9	SEM images of Network 3 and Network 4 of etched quartz micro-model; (a) Network 3; (b) various profiles in an enlarged section of Network 3 (c) entrance region of Network 4 and measurement of wall profile at the entrance region	78
6.10	Representative surface-profile characterisation of networks by surface profilometer. Figures depict variation of network depth along the width for silicon (a) at entrance region of Network 1(b) at a randomly chosen place in the Network 1	80
7.1	The conceptual flow-map for ‘Reservoir-on-a-Chip’	84
7.2	Schematic of the experimental set-up used in performing waterflooding experiments with ROC; inset illustrates the magnified image of ROC housed in a casing, placed under the microscope for flow visualization experiments.	85
7.3	Distribution of oil phase (green color) and water phase (blue color) in the pore network during waterflooding experiments. (a) The presence of oil phase at the start of the waterflooding process (t=0); (b) Relative positions of oil and water phases at t = 5 mins; (c) Relative positions of oil and water phases at t = 13 mins. The presence of trapped oil is observed at the later part of the waterflooding process	89
7.4	A different section of the pore network capturing the same dynamics of the oil and water phases at t = 10 min.	90

7.5 Fraction of oil recovered in terms of original oil in place (OOIP) by injecting water at a constant flow rate of 100 $\mu\text{l}/\text{min}$, which is analogous to recovery curve used in reservoir engineering (Hadia et al., 2007); Insets show images of oil (green colour)/water (blue colour) phases corresponding to different time instants during the waterflooding process. 91

Chapter 1

Introduction

1.1 Motivation

The last part of the twentieth century and this century have seen a huge scarcity of hydrocarbon based fuels. This has translated into finding solutions for optimal recovery of the precious hydrocarbon from the oil reservoirs. When primary oil recovery processes no longer produce significant oil due to the natural pressurization of the reservoir, secondary or tertiary oil extraction techniques have been adopted frequently. It involves the introduction of fluids/chemicals/polymers inside the reservoir for the displacement of the resident oil in the reservoir. Water-flooding methods have been adopted for last few decades for enhanced recovery and in recent years, CO₂ injection has also been contemplated due to its potential benefit in terms of storage and sequestration. The mechanism of fluid flow inside the pores of the reservoir is complicated due to the presence of various phases and their interactions with the solid rock matrix. Investigating fluid-flow properties in artificially made pore-structure has only limited scope, and in order to fully understand the transport mechanisms at this scale, one needs to have a better picture of the actual porous reservoir rock. Over the past decade, researchers have focused on numerical and experimental study of fluid-flow at pore-scale, based on real porous media or realistic rock structures. The objective of this work is to investigate the porous structure of some representative rock specimens, as well as to fabricate a porous medium (Lab-on-a-chip) where the pore-network geometrically resembles the characteristics found in these reservoir rocks. This thesis aims to provide a framework for experimentation with micro-scale fluid flow, where parameters and flow-properties can be related to realistic reservoir

flow conditions.

1.2 Problem Definition

Porous reservoir rocks (such as sandstone, carbonate) are subjects of precise microscopic characterization, since the knowledge of actual geometry at the smallest void structure of the medium (i.e., the pore-scale) would facilitate simulation of transport properties. If various oil-extraction related parameters such as capillary pressure, relative permeability are studied in this real pore-space, then methods of Enhanced Oil Recovery (EOR) can be improved. While state-of-the-art microscopy (for e.g., micro-computed tomography or micro-CT) has been used in numerous studies, there are various limitations of such studies pertaining to a single conventional method of pore-scale characterization. It is quite challenging to obtain the correct pore-scale information in terms of pore-connectivity, smallest pore-size and very importantly, pore-distribution etc. Pore-connectivity implies the manner in which void structures inside the porous medium are connected to each other, and is one of the major factors governing fluid transport. Pore-size and pore-distribution are other inherent characteristics of such reservoir-specimen and plays a significant role in deciding the suitable fluid for injection and relevant parameters during oil-displacement. Robust sample preparation techniques and characterization methodology would ensure a complete picture of the complex micro-structures of sandstone materials. Carbonate poses another type of problem for the researchers. Due to its sub micron-scale features, many of the standard microscopic methods are incapable of defining carbonate pore-structure. Exclusive sample preparation technique is required for such rock materials, where serial-sectioning of the sample is possible along with visualization at nanometre-scale. If the pore space data obtained in this manner is converted to a pore network (i.e., an integrated structure of larger spherical void spaces connected by thin constriction-like shapes), a scientific and realistic representation of oil-reservoir is obtained. Various numerical simulations can be performed on such a network and transport properties can be calculated. However, converting this network to a micro-fabricated model would be a very interesting task, since normally such miniaturization attempts are limited to random porous structure or network. Performing various fluid-flow or oil-displacement experiment

in such micro-model would actually capture the essence of oil-displacement in a smaller version of an oil-reservoir, with the advantage of observing the interaction of fluids/fluid-solid at pore-scale.

1.3 Thesis Overview

1.3.1 Objective: Conceptual Map of Reservoir-on-a-Chip/ROC

This cutting-edge microfluidic device, described in the previous section has been termed a Reservoir-on-a-Chip (ROC), drawing comparison with Lab-on-a-Chip (LOC). The idea behind coining this terminology is that, a whole reservoir from oil-field scale is brought to lab-scale experiments, without losing the exact pore-structure of the rock material. Advent of modern imaging techniques has made it possible to describe the pore architecture of the porous medium directly (Hazlett, 1995; Wilson et al., 2010; Wirth, 2009; Gunda et al., 2011). Along with X-ray tomography, serial-sectioning imaging techniques with resolution range in the scale of nanometers (for e.g., FIB-SEM) can be used for authentic characterization of these rock-cores. Precise quantification of porosity and pore-connectivity can be attempted by analyzing the various tomography data obtained from these methods.

Once the reconstruction of pore space is completed, it can be converted to a pore throat network with the help of practised methods of network extraction (Al-Kharusi and Blunt, 2007). This network would signify one of the more realistic representations of a porous medium. The next task would be to prepare a micro-model/microfluidic chip based on this network representation, with the various fabrication parameters designed such that the final outcome resembles an oil-reservoir. Waterflooding experiments can be performed in this ‘Reservoir-on-a-Chip’ (ROC) to ensure the feasibility of this term (and device) in various flow transport simulations.

1.3.2 Thesis Outline

The rest of the thesis has been organized in the following manner:

Chapter 2 introduces the various research works related to the steps de-

scribed in the previous sections. The chronological development of the discipline is looked upon, the wide range of works has been compared and the requirement and scope of developing further methodologies have been pointed out.

The characterization of Berea sandstone rock has been discussed in **Chapter 3**, starting with description of micro computed tomography (micro-CT) and Focused Ion Beam-Scanning Electron Microscopy (FIB-SEM) on sandstone specimen. Three-dimensional (3D) reconstruction has been performed based on the microscopy-data and subsequent quantification is reported.

Chapter 4 is a description of simulation of waterflooding in commercial package COMSOL. Instead of using a regular porous geometry as the domain of simulation, micro-CT images of sandstone have been incorporated in the COMSOL interface. Thus, this chapter discusses the numerical study of oil-displacement in a two-dimensional (2D) porous medium and corresponding parameters.

In **Chapter 5**, the pore-structure investigation of carbonate rock core using Focused Ion Beam has been reported. Analysis of the pore-structure for this rock sample, based on pore-space reconstruction, has been discussed in this chapter as well.

Chapter 6 discusses the design of several pore-networks, which would closely represent a porous medium occurring in the hydrocarbon-reservoirs i.e., a natural porous medium. The complete fabrication procedure of these networks on glass and quartz has been elaborated. In order to prepare these pore-networks as a complete micro-model, they have been closed with other layers with inlet and outlet ports. The results of analyzing the prepared micro-models with a scanning electron microscope (SEM) as well as a surface profilometer are presented in this chapter.

Chapter 7 introduces an experimental technique for visualization of oil-displacement process (with water as the displacing fluid) in the prepared micro-models, and discusses the realization of the novel concept of a ‘Reservoir-on-a-Chip’.

Chapter 8 discusses the main conclusions drawn from this work, as well as some suggestions about possible routes of future study based on the same motive.

Chapter 2

Literature Review

In the previous chapter, the problem related to efficient recovery of hydrocarbon resources from field/reservoir has been introduced. In this chapter, various studies are discussed, which have addressed this type of problem. The relevant works in context of reservoir-rock or porous medium, in general, are noted and hence, the scope of developing state-of-the-art microscopy and robust characterization methods for these realistic pore-spaces have been identified. Experimental studies involving fabrication of random porous medium have been summarized. The comparison of the related works has been gone through in detail, for designing a concrete path of achieving the concepts introduced in this study.

2.1 Secondary and Tertiary Oil-Recovery

A typical oil-field/reservoir extends a few hundred meters below the surface of the earth. This reservoir is porous in nature, and the size of the pores i.e., the void space in the reservoir can be as small as a few hundred nanometers to a few μms . For extracting resident oil from these reservoirs, normally one relies upon the natural driving mechanism due to pressure existing inside. This method of extracting oil is called ‘Primary Oil recovery’ and used widely for industrial purposes. However, the efficiency of this type of recovery is very poor as the pressure-force gradually decreases with time, and the production of resources declines. It is seen, that the primary recovery methods are only able to recover 30-40 % of total oil in a reservoir site. Hence, enhanced recovery processes (Enhanced Oil Recovery (EOR)) must be adopted which involves supplementary help from injected fluids (Ahmed, 2010). The fluids used at

this step of recovery are water or gas, and waterflooding (using water as the supplementary fluid) is a very popular and effective method for secondary recovery. The use of this method dates back to a few decades. In '80s, Pope (1980) proposed a generalized theory for water flooding based on Buckley and Leverett (1942) type of displacement and extended it to polymer flooding, carbonated water flooding or hydrocarbon miscible flooding. Bigg and Koch (1970) investigated the various production data across US in '70s and has shown that the proper implementation of water flooding can actually recover 800 barrels of secondary oil from 25 producing zones. Such detailed studies of waterflooding (Craig, 1971) have also carried out with special focus on oil-water flow properties, efficiency of oil-displacement and prediction of water flood performance. Based on the evaluation of waterflooding-performance, the economic feasibility of waterflooding in a certain site can be deduced (Jaber et al., 1999); while such studies can be extended for performance-prediction in an oil-field, where secondary recovery is yet to be attempted (Kaiser, 2009). The process of alkaline water flooding, where the pH of water is increased by injecting relatively inexpensive chemicals to invading water, is an interesting prospect in terms of performance and has been discussed in detail by Mungan (Mungan, 1981).

Once primary and secondary recovery options have been exercised in a place, for additional extraction of oil tertiary methods are considered. In tertiary oil recovery processes, miscible and immiscible gases including carbon dioxide (CO_2) and chemicals, surfactants etc. are used as flooding phases and even thermal energy is used in some cases to displace the oil. The use of CO_2 has also found applications in carbon sequestration i.e., the reduction of carbon in atmosphere by storing it in oil reservoirs (Ghomian et al., 2008) (Damen et al., 2005). A number of experimental and numerical studies has been performed by Sayegh and Fisher (2009) to predict oil recovery, by using miscible displacement between oil and CO_2 . The scope and performance of CO_2 flooding have been addressed in various studies as well (Alvarado and Manrique, 2010). Methods involving various chemicals (dilute surfactants, polymer etc.), water-alternated gas (WAG) and thermal injections (Liu et al., 2007; Thibodeau and Neale, 1998) are quickly becoming promising areas of exploration, based on the studies of their incremental recovery and economic nature (Babadagli, 2007).

The success of secondary and tertiary extraction methods is related to the interaction of various phases (oil/fluid/air) inside the reservoir, and the geometry of the void space along with the material properties of oil-containing rock plays a massive role in this. It is an established truth, that lithology i.e., characteristics of rock influences the efficiency of water-injection and other type of injections to a great extent (Thomas et al., 1989) and porosity and permeability are the principal factors governing this influence. Since the secondary and tertiary methods of recovery attempt to displace oil from the smaller (in order of a few μs) void structures (or pores), the complex interplay of displacing and displaced fluid in porous reservoir i.e., the underlying physical processes of oil-displacement occur at pore scale (Tiab and Donaldson, 2004). Hence, one must deal with the micro-scale porosity/ micro-structure of the rock material while investigating the transport properties of fluids in them.

2.2 Characterization of Reservoir-rock Specimen

Last two decades have observed increased interest on part of researchers to look into real porous materials, and characterize the pore-space in terms of a geometrically defined region. Instead of studying various transport phenomena in an ideal and regular pore geometry, real rock specimens offer a deep insight in the problems encountered in an oil-field. These types of reservoir-materials are mainly sedimentary rocks by nature and can be of various composition (sandstone, carbonate etc.). For this work, one sample sandstone (Berea sandstone) and one carbonate core (dolomitic) have been selected. Berea sandstone is the type of sandstone found near around Berea, Ohio, USA and has been named accordingly. Sandstone is made of silica and quartz, abrasive and brittle in nature, and often used as building materials. Oil-bearing carbonate reservoirs are found in abundance in Middle Eastern countries such as Oman and Saudi Arabia as well as in North America, and many of the carbonate reservoirs have dolomitic composition.

2.2.1 Micro-CT Images

The starting point for precise geometry description of such rock-cores is, undoubtedly, a clear image of the micro-structure for the porous rock sample. Various imaging techniques and microscopy are the most suitable methods for this micro-structure characterization. To date, non-destructive imaging techniques like micro-Computed Tomography (micro-CT) and X-ray tomography are used widely for this purpose (Hazlett, 1995; Kalender, 2006). Individual cross-sections of the porous sample is captured, using x-rays from a source at one side of the specimen and x-ray detector on the other side. During the imaging process, either the prepared sample or the x-ray source can keep rotating in steps of very small angles, in order to capture image of the next cross-section. This type of tomography imaging allows volume reconstruction of the specimen, when the cross-sections are put together and hence, finds a wide range of application in bio-medical imaging as well as material science (Schambach et al., 2010). Sandstone rock-cores have been investigated in various works using 3D micro-CT techniques. Verges et al. have reconstructed several pore-spaces of sandstone from computed tomography images and compared the results with that obtained from Mercury Intrusion porosimetry (MIP) (Verges et al., 2011). Various sedimentation simulations have been performed on the micro-CT data as well, for obtaining the most accurate digital representation of rock-core (or digital core) (Liu et al., 2009). Computation has also been performed on direct digitalized micro-CT images of core-fragments (Arns et al., 2005) for calculation of properties such as capillary pressure etc. Turner et al. have demonstrated investigation of drainage experiments in rock-cores using micro-CT images (Turner et al., 2004). It has been pointed out in the subsequent chapters and performed work that these micro-CT images contain certain artifacts during imaging at high resolution, which tend to misrepresent the pore-space.

Carbonate rocks pose difficulties in microstructural analysis because they have complex sedimentation histories, pre-existing fracture networks and large variations in pore sizes. Although carbonate sedimentary rock-cores have been investigated using micro-CT imaging method, the reconstructed pore-space in carbonates from these images is not reliable, as the minimum resolution of this technique is on the order of micrometres and the mean pore size in

dolomitic $[\text{CaMg}(\text{CO}_3)_2]$ core samples is often less than that (Okabe and Blunt, 2004). Similar to drainage experiment visualization in sandstone rock-core using micro-computed tomography, waterflooding in carbonate chalk cores have been characterized in some studies (Mogensen et al., 2001). Micro-CT images have been used for front-tracking of fluid-phase inside the core during performing this experiment. However, because of the intergrain porosity of carbonate rocks, the resolution required for useful imaging is often on the order of 20 nm with a field of view of 100 μm . To date, reconstructions of 3D pore spaces from micro-CT data have provided poor descriptions of the complex pore space and have led to unrealistic simulations of transport properties.

2.2.2 Focused Ion Beam-Scanning Electron Microscopy (FIB-SEM)

Focused Ion beam-Scanning Electron Microscopy (FIB-SEM) is one of the more advanced methods of destructive imaging methods and a state-of-the-art technique in microstructure characterization or site-specific topography analysis. The set-up uses focused beam of liquid-metal (generally Ga^+ ions) as well as charging electrons for imaging purpose. Determination of three-dimensional (3D) characteristics of materials (eg. Number of pore features per unit volume, pore connectivity, real feature shapes and sizes, information about spatial distribution etc.) has been a major key in realistic pore-structure characterization in recent research. While serial-sectioning methods used to be concerned with finding out the structure of organic and inorganic materials in macro-scale, Focused Ion Beam-Scanning Electron Microscope (FIB-SEM) applies this method in microstructure estimation and has been used extensively in the last decade for the determination of microstructure of various materials (Orloff, 2001), for e.g., electrode materials used in fuel cells (Barnett et al., 2007). Early works related to microstructure-analysis of porous materials using Focused Ion Beam include Holzer and others' work on ceramic objects like BaTiO_3 (Holzer et al., 2010). They also introduced the ideas related to larger trench sizes on both sides of the section in order to avoid shadow-imaging. Image recognition in control strips in relation to the automation of the whole process was also discussed. While previously characterization was mainly performed with two-dimensional information from sections obtained by Scanned Electron Microscopy (SEM), Transmission Electron Microscopy

(TEM) or Atomic force microscopy (AFM) up to atomic scale (Meyer et al., 2004) (Williams and Carter, 1996), FIB combined with Secondary electrons (SE) or Back scattered electrons (BSE) advanced the characterization process to certain extent (Principe, 2007). Energy-dispersive X-ray spectrometer (EDS) maps were analyzed in relation to FIB trenches (Kotula et al., 2006), while improved filters were used in image processing and extraction of significant data from the cross-sections (Russ, 1999) (Gonzales and Woods, 2002).

Literature suggests that Focused Ion Beam-Scanning Electron Microscopy (FIB-SEM) has been used for porous ceramic substrates (Wilson et al., 2006) and other geomaterials (Wirth, 2009), while electron back-scattered diffraction (EBSD) analysis along with FIB provide microstructure analysis for many metallic alloys. The texture and the orientation of the crystalline materials is best elucidated by EBSD. Brent Adams and others have discussed the EBSD technique for orientation imaging (Adams et al., 1993) and Robert Schwarzer reviewed automation of this method by computer-controlled SEM (Schwarzer, 1997). This method has been applied for three-dimensional structure and grain size determination of electrodeposited Co-Ni films (Bastos et al., 2008), study of large undeformable particle in hot-rolled Fe₃Al-based alloy (Konrad et al., 2006), ultrafine grained dual-phase steel (Calcagnotto et al., 2010) and many other metallic compositions. Such EBSD has also been extended to study the microstructure below a nanoindent in Cu single crystal (Zaafarani et al., 2006). In terms of porous reservoir rock samples, many clay-based rocks have pores in the the order of nanometers, and FIB-SEM along with cryo-SEM have been used very recently to study such mesoscopic pore structures (Holzer et al., 2004). One common example of using FIB-SEM as the tool of investigating microstructure is for solid-oxide fuel-cells (SOFC) like a mixture of LSM (La-Sr-MnO₃) and YSZ (Y₂O₃ZrO₂) (Wilson et al., 2010). There, the sample is impregnated with epoxy and the images to discriminate different phases are conducted by using inlens detectors (for capturing back-scattered electrons). Various important quantities like three-phase-boundary and tortuosity or interconnectivity have been computed from the images. Recently, Gunda et al. (2011) have looked into the microstructure of Lanthanum strontium manganite (LSM) with the help of FIB along with extensive image post-processing for studying porosity, internal surface area, conductivity and diffusivity as well as generated computational domains for calculation of effective transport prop-

erties. The success of the use of FIB-SEM for ceramic electrode materials like LSM-YSZ has motivated the studies described in following chapters to adopt this technique for investigating the pore structure of a rock sample.

Investigation of rock microstructure by use of FIB-SEM has been attempted in recent times, especially on carbonate rock cores (due to its sub-micron scale porosity). The successful ion milling of porous rock samples requires particularly precise milling times and low ion beam energies, which makes FIB-SEM a suitable method for microstructural investigations of many such materials. Many clay-based rocks have pore sizes in the order of nanometres, and FIB-SEM along with cryo-SEM have been used for these type of rocks. Tomutsa and Silin (2004) used FIB to serially section diatomite and chalk samples; they subsequently employed direct morphological analysis of the reconstructed pore space images to determine petrophysical properties such as pore size and capillary pressure. Sondergeld et al. (2010) performed FIB-SEM analysis on gas shales (as well as other sedimentary rocks) and measured porosities, morphologies and other characteristics. Knackstedt et al. (2009) analyzed reservoir rock structures (including reservoir sand and carbonates) by tomographic visualization processes (micro-CT and FIB-SEM); based on their imaging data, they suggested a numerical approach for studying the physical properties of porous rocks. Recently, Lemmens et al. (2010) performed FIB-SEM analyses on a carbonate specimen and then used automated mineralogy to determine petrological characteristics of the specimen (e.g., grain size, grain density and porosity). However, the investigation of carbonate rocks by such imaging techniques still remains a challenge, not only because of the difficulty in preparing samples for serial sectioning but also because of variations in the pore structure from the sample surface to the interior of the specimen. In this work, sample preparation methods have been proposed and performed for successful serial-sectioning of both sandstone and carbonate dolomite core specimens.

2.3 Pore Network Model

Once the first step of the geometry description i.e., the characterization of the micro-structure in such reservoir materials has been performed, the next task is to provide the pore-space a geometric shape, where various simula-

tions can be performed and flow properties can be measured. Pore Network Model (PNM) is commonly used for this purpose and applied to understand the fluid transport in pore scale. In this model, void space inside the porous rock surface is represented by a network of pores (or bulges) connected to each other by numerous constrictions (or throats). Fatt (Fatt, 1956a,b,c) proposed such network representation of pore space which later became a widely accepted mode for representation of porous media. In earlier studies, the pore-throat network were usually prepared based on numerical modelling and then flow-simulations have been performed. Reconstruction algorithms have been applied for generating disordered network and performing two-phase fluid-flow simulations (Oren et al., 1998). Lerdahl et al. (2000) extended these methods for three-phase fluid-flow and their interactions in a porous medium. Mani et al. developed such three-phase (mainly oil, water and air phases) pore-network models and studied the effects of various parameters (such as capillary pressure) on relative permeability (Mani and Mohanty, 1998; Fenwick and Blunt, 1998). These predictive features are mainly based on the application of conservation principles between the pores and the throats. Various wettability considerations and implementation of wettability alteration in the numerical models implied significant progress in PNM related studies (Blunt, 1998; Zhou et al., 2000). Hughes and Blunt (2001) extended this type of numerical studies for fractures in such porous medium. Dixit et al. (1999), in a very important study related to such modeling, have related such properties with oil recovery and consequently, such studies were extended for sandstone and other rock materials as well. Among various pore-level numerical studies in this context (as performed in Chapter 4), Ovaysi and Pini (2010) have performed direct pore-scale simulation of incompressible flow. Zaretskiy et al. (2010) performed transport simulations in 3D pore geometries.

Significant progress in this area has been made in the past couple of decades, as suggested by the review article by Blunt (2001), where PNM can be used to successfully predict oil recovery. As the imaging techniques have progressed, realistic rock structures have put under scrutiny for converting them to pore-throat networks (Dong and Blunt, 2009). This approach has facilitated the matching of property simulation results with similar data obtained from field-scale. Various algorithms (such as Maximal Ball etc.) have been proposed for transforming a real pore-space in a structured pattern of

pores and throats, with the co-ordination number (i.e., the manner in which pores are connected to the throats) depicting the variable porosities occurring in natural reservoir-rocks (Al-Kharusi and Blunt, 2007). PNM has further been used to determine certain properties like average pore occupancy in the field scale (Lovoll et al., 2005). A part of the fabrication described in present study has been related to design of various pore-networks resembling a real reservoir-rock micro-structure.

2.4 Microfabrication of Porous Media and Experimentation

Along with the numerical investigation of various fluid-flow conditions in a porous medium, development of efficient oil-recovery techniques require experimental techniques conceived and realized at lab-scale. These methods can then be optimized or scaled-up for possible application in the field-scale of oil-bearing reservoirs. Traditional lab-scale flooding experiments, known as core-flooding experiments, use a core from a sample reservoir-rock for experimentation and the pore-volume is calculated by using water. Once, the pore-volume is known, the core is completely filled with oil-phase, and then water (or other fluid characteristic of secondary and tertiary recovery processes) is injected. The collection of oil recovery data (Hadia et al., 2007) is the final outcome of these type of experiments. However, the fluid transport processes in a reservoir occur at a pore-scale, the smallest structural feature in such reservoirs. Hence, core-flooding experiment is not always sufficient for providing minute detail of fluid-phase interactions in oil-reservoirs. As a result, one has to rely on various micro-fabrication methods for creating a porous medium and performing experiments in it.

Micro-Electrical Mechanical System (MEMS) based microfabrication techniques, originally developed for semiconductor industry (van Zant, 2006), have become one of the principal tools in fabricating micro/nano-structures, relevant to different applications in engineering and applied science (Datta and Landolt, 2000; Romankiw, 1997). Advanced methods of lithography have brought new horizons in micro-machining techniques (Lochel et al., 1996; Lloyd and Taub, 1988). Earlier evidence of various flow-visualization experiments in micro-models exists (Chatnever and Calhoun Jr., 195), and later Lenormand

et al. made significant progress in multi-phase studies in fabricated micro-models (Bonnet and Lenormand, 1977). They continued with the fabrication of glass micro-models representing a porous medium, and performed immiscible displacements and numerically validated the data as well (Lenormand et al., 1988). They also extended such investigation of fluid transport in micro-models to characterize ‘viscous fingering’ effects as well as percolation (i.e., how the various fluid phases would move inside the fabricated micro-model) (Lenormand and Zarcone, 1989; Lenormand, 1989). While the earlier micro-models used to be predominantly glass ones, advances in micro-fabrication techniques have prompted cutting-edge chip fabrications on other substrates, such as silicon or polydimethylsiloxane (PDMS) (Martinoia et al., 1999; Smith et al., 1992; Hoffman et al., 2007). Suzuki et al. (2010) have described various sol-gel based methods for fabrication of artificial porous medium on PDMS. Entire microfluidic devices have been prepared on such polymer as well (Zhang et al., 2009), and Romoli et al. (2011) have demonstrated a laser-machining approach for such fabrication on PMMA substrates. With time and progress in the relevant methods, the researchers have attempted to fabricate a pore-network inside a micro-model, for capturing the physics relevant to geometry-effects inside the porous reservoir. Perrin et al. (2006) described various experimental studies related to Newtonian and non-Newtonian fluids inside a fabricated pore-network, Ferer et al. (2007) described the viscous fingering and capillary effects in such network and others reported experiments involving pressure-driven flow in these microfabricated networks (Fuerstman et al., 2003).

These networks, however, are mainly limited to straight, serpentine and combination of such regular geometric features. Numerically prepared randomly generated porous structure is usually incorporated in the microfluidic device by soft-lithography techniques and then experiments and visualization are performed. Often micro-models with glass beads are used for this purpose (Hatiboglu and Babadagli, 2010). Among examples of relevant studies on the random pore-networks, Oren and Pinczewski (1995) have performed three-phase flow experiments in oil-wet micro-models and van Dijke et al. (2006) have extended such experiments for water-alternating gas injection in oil-wet glass micromodels. Polymer flooding in glass micro-models (Broseta et al., 1995) has been studied as well, and Meybodi et al. (2011) have performed detailed investigation of displacement behaviours in this context. Lab-on-a-Chip (LOC)

applications i.e., a microfluidic device with all the components of performing the experiment inherent in the device are limited for this kinds of study, when it comes to realistic pore-network. In a more recent effort, a pioneering work by Berejnov et al. (2008) has represented the porous medium as a structured microfluidic network with prescribed geometries. In their experiments, they have performed investigation of fluid flow parameters and wettability in such network, by tuning surface properties. This can be classified as the first implementation of Lab-on-a-chip concept for energy recovery. Among fabricating realistic porous medium, Perrin et al. (2005) have achieved the closest realization, where they were able to create a two-dimensional etched micro-capillary pore on silicon substrate to investigate the velocity field within the pore space. Thus, the scope of fabricating a porous medium, which would be a scientific representation of a naturally occurring porous reservoir-rock, has motivated the ideology and methods of the work described in the following chapters.

Chapter 3

Characterization of reservoir rock: Berea sandstone ¹

The methodology for describing pore space of a naturally occurring reservoir-rock specimen has been described in Chapter 1 and Chapter 2. Based on that, the initial step of characterizing a rock-structure is chosen to be X-ray micro tomography. Berea sandstone has been chosen as the first representative sample of oil-reservoir materials, and micro-CT has been performed in the characterization facility of Tomographic Imaging and Porous Media Laboratory (TIMP), University of Calgary. Based on the conclusion drawn from micro-CT imaging, further state-of-the-art microscopy in form of Focused Ion beam-Scanning electron Microscopy (FIB-SEM) is performed on the same specimen (at National Institute of Nanotechnology, National research Council, Canada). The detailed methodologies and conclusion regarding pore-structure reconstruction and quantification are reported in this chapter.

3.1 Micro-CT on Berea

This section describes the sample preparation and experimental procedure followed for performing X-ray micro-computed tomography on Berea sandstone.

3.1.1 Materials: Sample Preparation

The micro-CT facility works on samples of very small dimension due to the high scan resolution. In this study, a working resolution of 3 μm is used.

¹Parts of this chapter have been compiled from the publication in *Micron*, 2011, **42** pp. 412-418

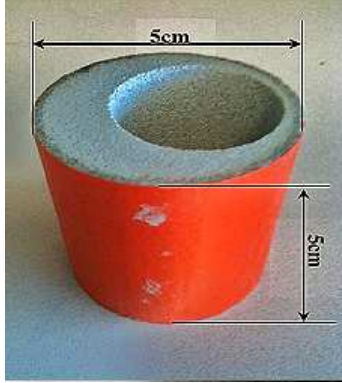


Figure 3.1 – Berea sandstone core

The final sample dimension is achieved by calculating the number of possible pixels in the scanned images and the sample size is taken as 3 mm x 3mm, which is extracted from a Berea sandstone core of approximately 5 cm X 5 cm dimension (Fig.3.1). A thin circular slice is cut off from this standard Berea sandstone core. Since, any normal rounding tool cannot be used due to the brittle nature of sandstones, an aluminium fixture is made. The fixture is circular and flat in nature with a circular hole in the centre with diameter equal to that of the final sample i.e., 3 mm. Application of pressure on the thin slice, while being held by the fixture, provides the cylindrical shape to the specimen required for micro-CT. The sample is rubbed against a sandpaper while it is still inside the aluminium fixture to obtain a polished surface. The polishing step is done while observing under a microscope to ensure maximum surface finish for better scanning quality.

3.1.2 X-ray Imaging Method

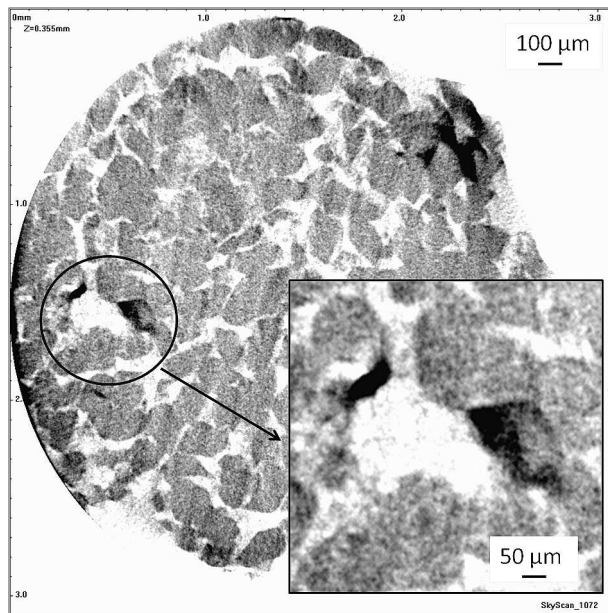
A Skyscan 1072 X-ray microtomograph is used for the parallel X-ray illumination. The X-ray produces shadow images i.e., two-dimensional projections of a three-dimensional sample for the horizontal cross-sections. The sample is exposed to the X-rays at 100 kV, 98 μ A for 3.5 seconds per exposure. While a single detector is dedicated to the X-ray projection at a particular horizontal cross-section, another detector captures the rotation of the sample for alignment of the next cross-section in the direction of the X-ray. In the present study, the angle of rotation of the specimen is 180° in steps of 0.9° .

3.1.3 Results

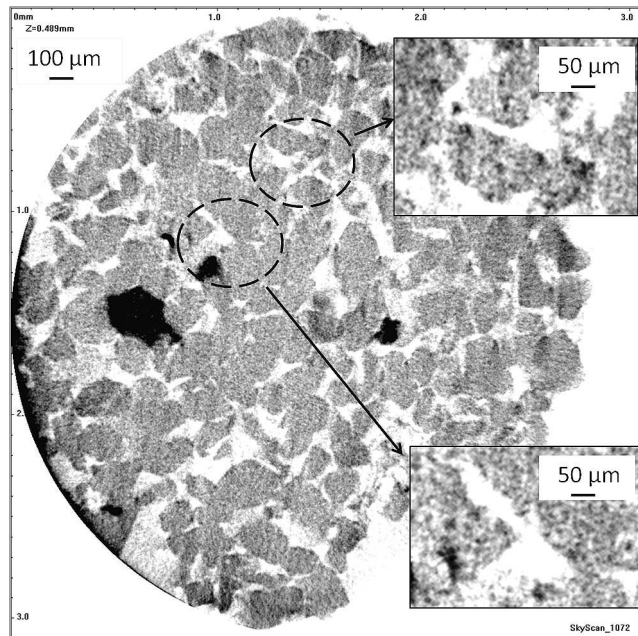
Series of images of the parallel slices with a separation distance of $6\ \mu\text{m}$ between the slices is obtained. The binary bitmap images clearly represent the solid matrix and the voids by their distinct contrast. It is found that, the void spaces consist of both large pores ranging over a number of sliced-images and small pores distributed over a couple of images in the X-ray projections. Sample images at different layers along the length of the specimen are shown (Figs.3.2(a), 3.2(b) and Fig.3.3). If one needs to track the void space (white color in these figures) along the length of specimen, it is found that such coherent structures (twelve such structures in this case) are repeated over the entire length of the specimen. These coherent structures signify bulk pores of size approximately $100\text{-}250\ \mu\text{m}$. These are almost crater-like giant pores distributed alongside the solid matrix. In parallel, smaller pores are present, with an average pore-size of $30\text{-}40\ \mu\text{m}$.

This arrangement of the solids and void spaces, however, presents only an incomplete picture of the porous nature of the material. Though the small-scale graininess (Fig.3.3) suggests the presence of additional pore structures in the order of $3\ \mu\text{m}$ to $10\ \mu\text{m}$, actually they may be due to various precision errors present during the micro-CT. Sandpaper is used as the polishing medium during the preparation of the sample. As a result, the surface roughness has not been removed completely and this results in different X-ray path lengths throughout the sample. Also, the current resolution of the micro-CT is set at $3\ \mu\text{m}$ for this sample, which is fairly close to the typical lowermost attainable resolution for any micro-CT system ($2.1\ \mu\text{m}$ in case of Skyscan 1072). At this resolution, detector noise is present, which gives rise to these grains, especially near the boundary. X-ray scattering effect is also responsible for these misleading grains.

Then, the next question that comes to mind is that whether such small pores in order of $3\ \mu\text{m}$ to $10\ \mu\text{m}$ which appear in micro-CT images exist in reality? Is Berea sandstone an integrated network of silica and pores entwined in overlapping matrices, or do they co-exist side-by-side? To answer these questions, another such sample of Berea sandstone is taken, which is milled with a FIB to look further inside its porous structure using SEM. It is to be



(a)



(b)

Figure 3.2 – Micro CT on Berea sandstone sample (a) micro-CT image, distribution of the solid and void structures represented by black and white colors, respectively, inset shows an enlarged solid-void structure distribution. (b) Typically, large void structures (crater-like shapes) of size greater than 100 μm (bottom inset) co-exist with the relatively small size pores of average size, ranging from 30-40 μm to 70-80 μm (top inset).

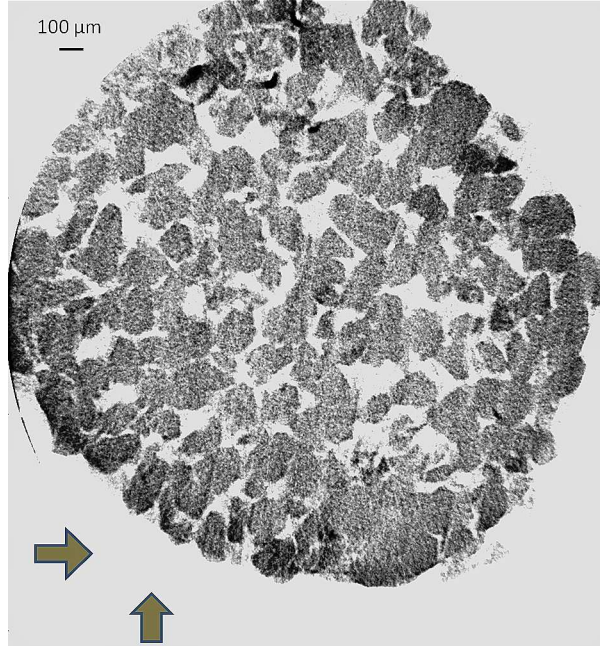


Figure 3.3 – Misleading small-scale grains (caused by surface roughness, detector noise, and X-ray scattering effects) in the image suggest the presence of pores in the order of 3-5 μm , arrows point out reduced effective diameter.

noted that during the comparison of the Pore Size Distribution (PSD) from two different methods, viz., micro-CT and FIB-SEM, the distribution varies notably for the same material, based on the specific definition of PSD (discrete or continuous) for these two separate methods. Such observations concur with FIB datasets and Mercury Intrusion porosimetry (MSI) results.

3.2 Focused Ion Beam on Berea

3.2.1 Materials: Sample Preparation

Berea sandstone samples typically exhibit surface roughness and are by nature brittle. In order to conduct material characterization on such sample inside a FIB-SEM vacuum chamber, a planarized surface is preferred. A Berea sandstone specimen (8 mm x 8 mm x 3 mm) was prepared for the FIB by polishing with help of precision lapping films (thickness up to 0.1 μm) in National Institute of NanoTechnology sample preparation laboratory. A conductive sputter-coating is done on the prepared Berea specimen with 10 nm of chromium to eliminate charging effects, followed by SEM imaging in order to verify the

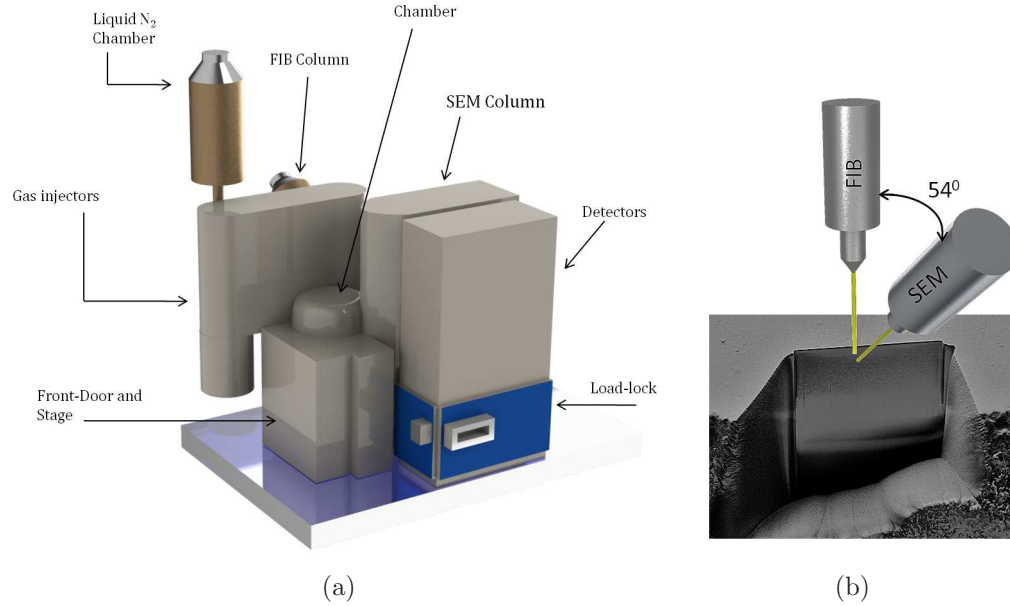


Figure 3.4 – FIB-SEM on Berea sandstone (a) Schematic of a standard Focused Ion Beam (FIB) set-up (b) specific arrangement of the ZEISS N-Vision 40 Crossbeam Workstation for the Berea specimen with the stage at 54°

feasibility of FIB milling and to select suitable milling sites.

3.2.2 FIB-SEM: Internal Microstructure Imaging

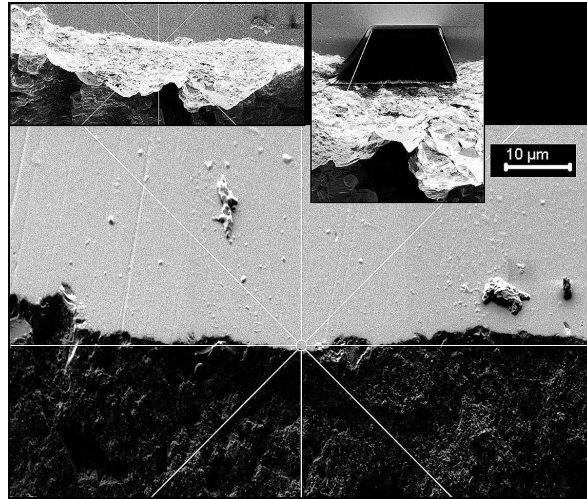
In this study, a ZEISS N-Vision 40 Crossbeam Workstation is used. The prepared sample is mounted with carbon tape in the Crossbeam workstation. A voltage of 30 kV and a current of 13 nA are used for depth-specific trench milling and further finer milling is achieved with a 300 pA probe current. Final polishing of thin section was performed with a probe current of 100 pA. An Everhart-Thornley (E-T) detector is used for revealing the topography at high resolution and Inlens detector is engaged for looking at the composition and the texture at the selected section of the specimen. Berea sandstone sample is exposed to the ion beam with the stage inclined at 54° to the horizontal (Fig.3.4(b)). A suitable site on the polished solid matrix is chosen and the FIB was used to expose a surface of dimensions 15 μm x 15 μm (Fig.3.5(a)). The removed material reveals a section, which is a solid matrix (Fig.3.5(b)) without the presence of any micro-pore (void) structures (implying void structure of size below 10 μm) inside this solid matrix, which is quite contrary to other porous materials like LSM-YSZ.

3.2.3 Results of FIB-SEM

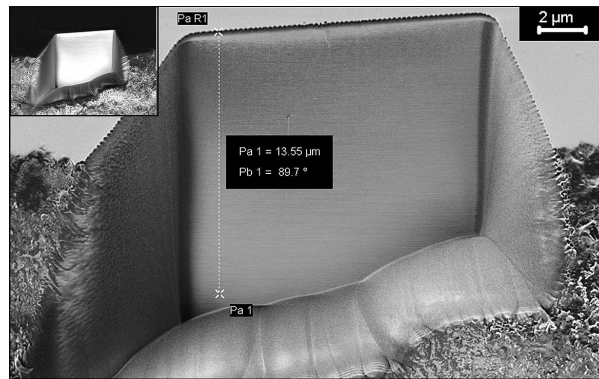
SEM images acquired at a lower magnification reveal that the solid matrix is surrounded by a variety of void structures, crater-like shapes and small pores, small pores having a minimum size in the order of $20\ \mu\text{m}$ - $30\ \mu\text{m}$ (Fig.3.5(c)). In order to investigate on this nature of the seemingly pure solid matrix, further milling is performed on all the sides of the previous trapezoidal structure with 30 kV and 1.5 nA current. Instead of the serial milling in a single direction, materials are removed from opposite directions to create a thin walled section; a standard technique used for the preparation of samples in transmission electron microscopy. Finally, a small probe current of 300 pA is used for obtaining a very thin section (Fig.3.6(a)) i.e., the wall is then polished to electron transparency. The image of resulting thin cross-section is captured using both the E-T and Inlens detectors and observed to contain a continuous matrix of homogeneous silica without any presence of micro-pores (void structure in the range $5\ \mu\text{m}$ - $10\ \mu\text{m}$) within the solid matrix. On reducing the magnification, we have an aerial view of the surface, consisting of many such solid matrices (Fig.3.6(b)). **A**, **B** and **C** in Fig.3.6(b) depict the individual existence of crater-like shapes, solid matrices and smaller pores in Berea sandstone, respectively. It can be reasonably argued that all the solid matrices would reveal similar continuous behaviour and micro-pores are generally absent within such matrices. The large void structures are of the order of $100\ \mu\text{m}$ to $250\ \mu\text{m}$ and they are very similar to crater-like shapes, as one observes in micro-CT images. The relatively small pores which are present between separate solid matrices vary (labelled as **C** in Fig.3.6(b)) in size, somewhere from 30 - $40\ \mu\text{m}$ to 70 - $80\ \mu\text{m}$. These pores are either connected with each other along the length of the specimen or they may even terminate into crater-shaped voids.

3.3 Three-Dimensional Reconstruction

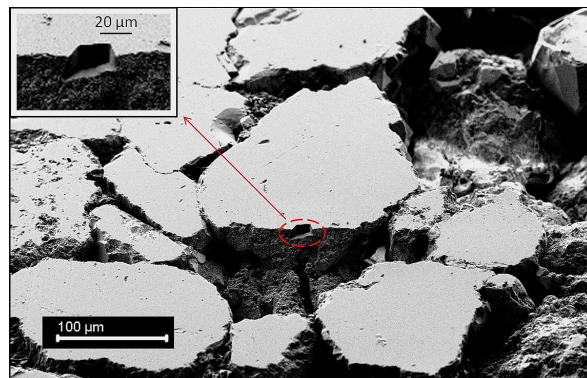
A three-dimensional reconstruction of the pore-space of Berea sandstone has been performed based on the micro-CT images of the sections, obtained through X-ray analysis and the key observations revealed from FIB-SEM study.



(a)

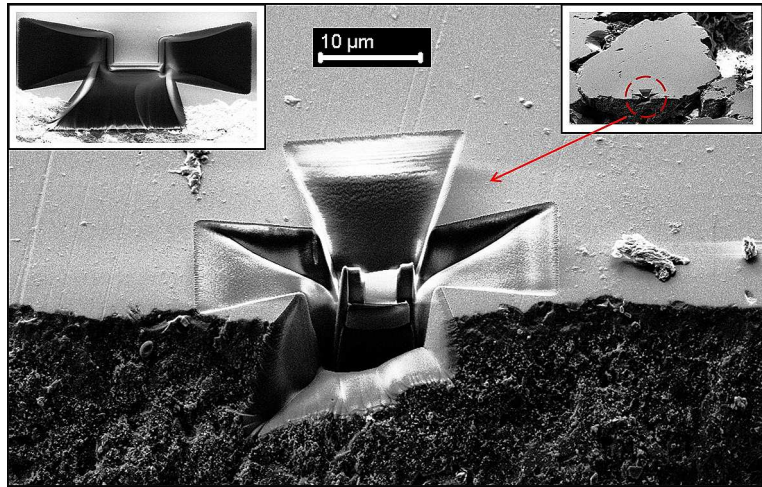


(b)

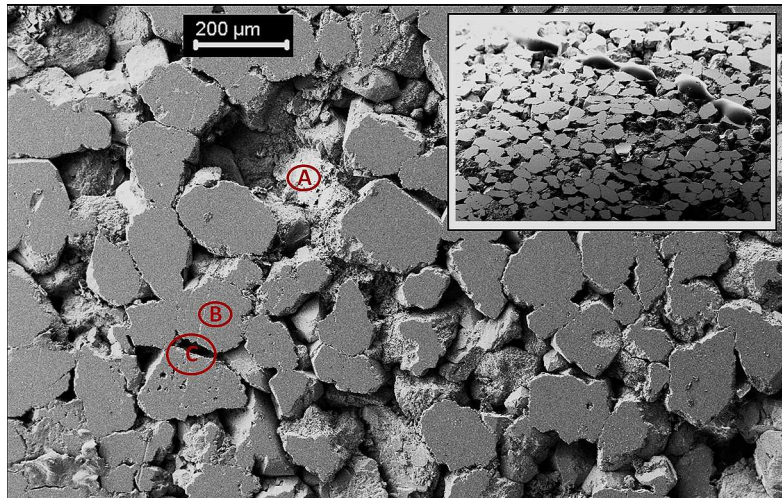


(c)

Figure 3.5 – FIB on Berea solid matrix (a) a single trapezoidal-shaped trench milled to depth $10\ \mu\text{m}$ (top right inset shows resultant trapezoid). (b) solid silica matrix after FIB milling without any presence of micro-pores (voids) (c) matrix surrounded by crater-like shapes and relatively smaller pores. Smaller pore structures are not readily noticed in this solid matrix after the first milling



(a)



(b)

Figure 3.6 – Results: FIB on Berea sandstone (a) further milling on all the sides of the trapezoidal structure reveals a very thin section (inset on top left depicts the removal of material from three directions), absence of any micropores inside the matrix is evident (b) void structures present in interconnected network outside the solid matrices of silica, the larger structures (craters **A**) being 100-250 μm in size interwoven with solid matrix (**B**) and smaller void structures (**C**) of size 30-40 μm .

For 3D reconstruction of Berea sandstone from the micro-CT images, Avizo Fire 6.3 commercial package is used. The reconstructed pore distributions have been depicted in Figs.3.7(a), 3.7(b), 3.7(c). Three different pore structures are obtained based on the different thresholding values during segmentation of pore and solid. Figure 3.7(a) is the resultant pore structure for a thresholding value of 200 while the following two reconstructions are obtained with threshold values of 206 and 220 respectively. The final reconstruction block has a dimension of (1.89 mm x 1.88 mm x 2.45 mm). For each reconstruction of the pore space, similar steps have been followed. First, the micro-CT images i.e., the individual slices are aligned in Avizo Fire 6.3. Separate filters are used for further detailing in the reconstructed 3D data. Median Filter 3d is used for removing any extra noise from the slices and Gaussian filter is used for smoothening effect. After the use of such filters, a few unwanted holes are observed in the images and hence morphological operations such as Opening and Closing are used for removing them. Finally the images are stacked and the three-dimensional reconstructions are obtained.

Before the characterization process from the CT images, however, various resolution parameters must be kept in mind. The pixel resolution for the CT images are $3.04 \mu\text{m}$ each in X and Y direction with 1024 pixels in each direction of matrix. The resolution in the Z direction is $6.07 \mu\text{m}$ based on the separation distance of the slices. So, the voxel size for the 3D data would be ($3.04 \mu\text{m} \times 3.04 \mu\text{m} \times 6.07 \mu\text{m}$). For CT images, the in-plane resolution (R) is given as:

$$R = \frac{FOV}{I} \quad (3.1)$$

where, FOV is the field of view and I is image acquisition matrix. In this case, the FOV is approximately 3 mm while the value of I is (1024x1024), and thus the resolution is close to $2.96 \mu\text{m}$ for the set of CT images. However, the spatial resolution is $5 \mu\text{m}$ and hence the justification of performing FIB on the sample, with much higher resolution, which is certainly capable of searching for smaller pore structure. Electron range is one of the important parameters related to FIB-SEM resolution, which can be calculated as (Goldstein et al., 2003):

$$R_{KO} = \frac{0.0276 \times A \times E_0^{1.67}}{Z^{0.89} \times \rho} \quad (3.2)$$

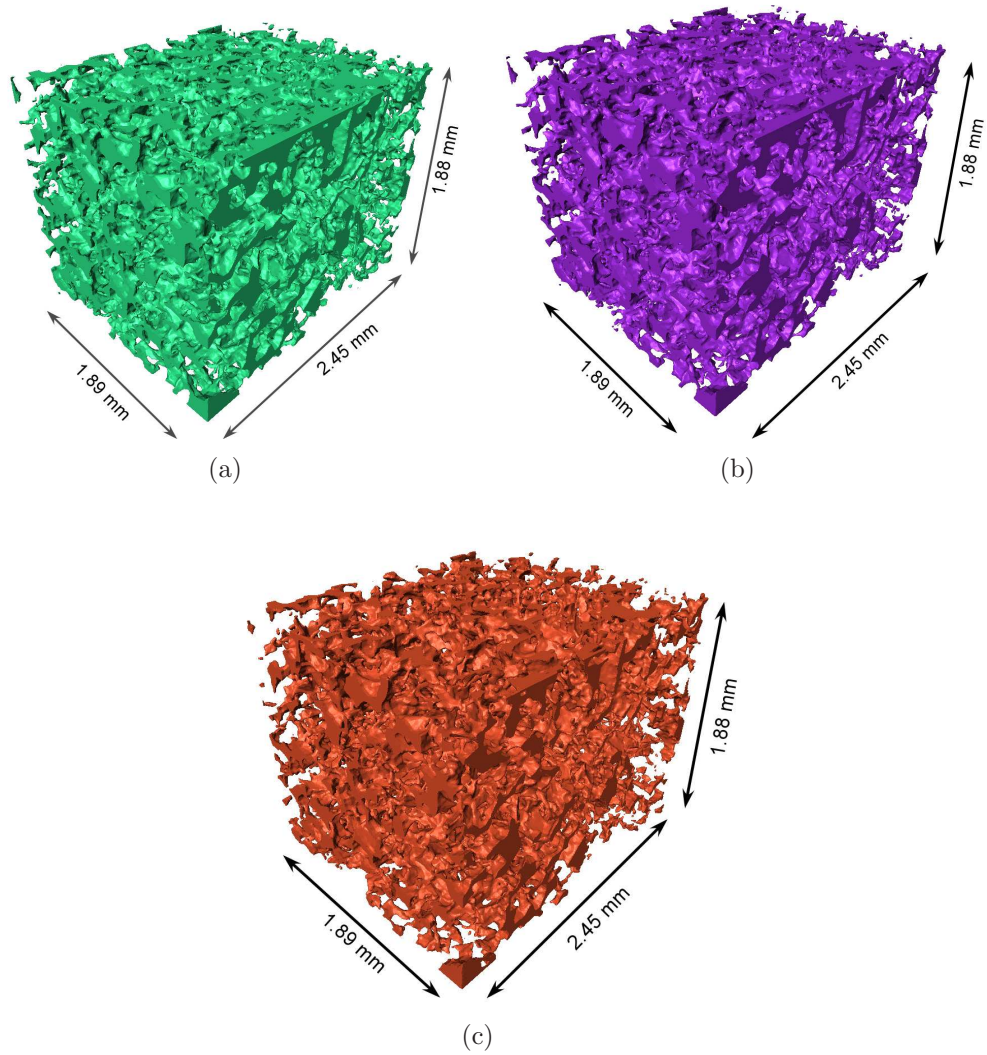


Figure 3.7 – Pore structure obtained from CT images using Avizo Fire 6.3 with (a) threshold value 200 and porosity 25.63%; (b) threshold value 206 and porosity 21.8%; (c) threshold value 220 and porosity 16.43 %

With the beam being tilted to an angle θ with respect to the base, the electron range can be modified as:

$$R_{\theta} = R_{KO} \times \cos \theta \quad (3.3)$$

Here, R_{KO} denotes the electron range (in μm), A is the effective atomic weight (in gm/mole) and Z is the effective atomic number of the sample, ρ the density (in gm/cm³), E_0 is the beam energy (in keV), R_{θ} is the effective electron range for tilted stage and θ is the angle of tilt. With the beam energy of 3 keV and 5.07 keV and tilt angle of 54^o, the effective electron range is in 200-400 nm. In this case, Inlens detector is used which considers a combination of Secondary electrons (SE) as well as the back-scattered electrons (BSE). So, effectively the working resolution of the FIB-SEM is in the range of nanometers.

From the pore structures of micro-CT image reconstructions, various quantifications of the data have been attempted. The number of pore bodies in each reconstruction and their volume have been calculated. The number of pore bodies for threshold values of 200, 206 and 220 are 3091, 2506 and 2216 respectively. The average pore size and the porosity values have been calculated from the obtained data in Avizo Fire 6.3. The porosity values are 25.63%, 21.8% and 16.43 %, respectively for the three different reconstructed volumes. Comparing the computed porosity with the commonly known porosity values, thresholding values in reconstruction can be estimated. Sections in three-dimensional space represent the pore structure from the reconstruction with thresholding value of 200, as shown in Fig. 3.8. For this sectional pore-distribution, XY, YZ and ZX slices have been considered at 1.52 mm, 1.52 mm and 0.4 mm respectively. The detailed pore-body characteristics for the three reconstructed microstructures are provided in Table 3.1.

Table 3.1 – Pore Body Characteristics of the three reconstructed microstructures

Pore body volume	Recon1	Recon2	Recon3
Maximum Volume (μm^3)	3.4x10 ⁷	3.8x10 ⁷	1.84x10 ⁷
Average Volume (μm^3)	7.32x10 ⁵	7.7x10 ⁵	6.46x10 ⁵
Porosity (%)	25.63	21.8	16.43

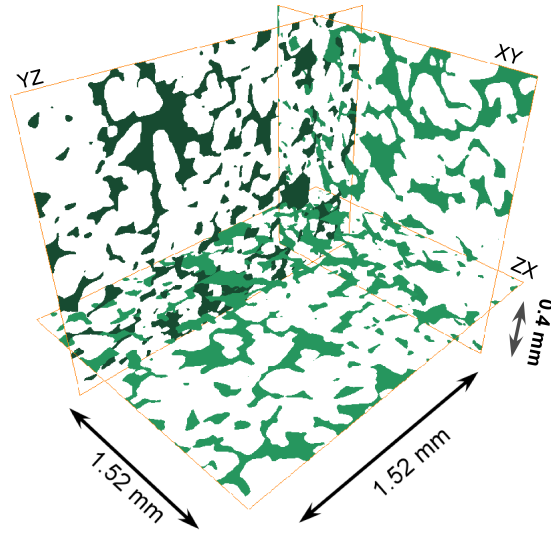


Figure 3.8 – Three different cross-sectional views of the 3D reconstructed microstructure (Recon1, with thresholding value of 200), with XY, YZ and ZX sections at 1.52 mm, 1.52 mm and 0.4 mm, respectively

Figure 3.9 depicts the variation in the number of pores with the microstructure volume for the three microstructure reconstructions. The average pore-volume for thresholding values 200, 206 and 220 are $7.32 \times 10^5 \mu\text{m}^3$, $7.7 \times 10^5 \mu\text{m}^3$ and $6.46 \times 10^5 \mu\text{m}^3$ respectively. It is observed that the maximum pore bodies are within the volume range of $10^7 \mu\text{m}^3$ and the number of pore-bodies decreases exponentially as one increases the pore-volume further. This corresponds with the pore-connectivity observed in FIB-SEM data, where it is seen that crater-like shapes (of size $100 \mu\text{m}$ to $250 \mu\text{m}$) are connected through smaller pores (of size $30\text{-}40 \mu\text{m}$) and not directly to other crater-like shapes. The absence of pore bodies in larger volume (Recon3, threshold value 220) signifies the departure of threshold value from realistic pore space distribution, based on which more suitable threshold values for reconstruction can be estimated.

3.4 Concluding Remarks

Berea sandstone is one of the principal oil-bearing rocks and the characterization of its microstructure is intrinsic for the understanding of various geological processes ranging from enhanced oil recovery to carbon capture and

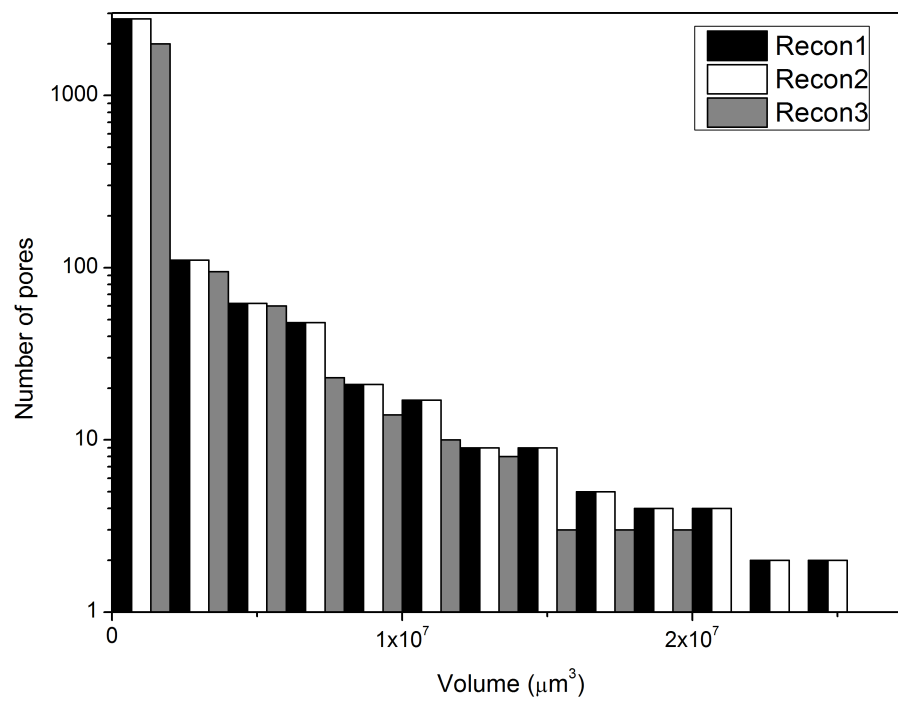


Figure 3.9 – Variation of number of pore with the microstructure volume for 3D reconstructed microstructures

storage. A new approach has been presented, which is a combination of two principal methods used for the determination of microstructures, viz., micro-Computed Tomography (micro-CT) and Focused Ion Beam-Scanning Electron Microscopy (FIB-SEM), to scrutinize the microstructure of Berea sandstone in terms of solid-void structure distribution. Also, for the first time, FIB-SEM has been used to characterize Berea sandstone samples.

Large crater-like voids have been identified and relatively smaller pores from the micro-CT section images along with presence of small-scale grains impersonating void structures in that scale have been noticed. The reasons of such small-scale grains are X-ray path length variation, detector noise and the scattering effects, which are typical characteristics of such X-ray images. To investigate further on the solid-void structures, an N-Vision40 Crossbeam Workstation has been used. The milling and subsequent image capturing clearly reveals pure solid matrices, free of micro-pores running inside them. It also revealed that, the pores are entwined with each other, without entering into the solid matrix and they sometimes end up as much larger voids. Some of these voids are as large as $250 \mu\text{m}$, which are labelled as crater-like shapes, while the relatively small pores are of the range $30\text{-}40 \mu\text{m}$. Further, the micro-CT images have been processed to obtain a representation of the pore space. The volume distribution of the pore space has been calculated with different thresholding values taken into consideration. Porosity values have been calculated from the size distribution for the reconstructed images.

The absence of micro-pores ($<30 \mu\text{m}$) inside the solid matrix is a conclusive picture of the microstructure for Berea sandstone. The observation is quite contrary to the common understanding of the Berea microstructure from micro-CT images only, where it is believed that such micro-pores do co-exist along with small pores. It is to be noted that the Berea sample taken for this study is very homogeneous and hence the micro-structure extracted from micro-CT and FIB-SEM studies hold true for the entire specimen. However, there may exist certain variation in pore morphology from specimen to specimen, and one needs to perform FIB-SEM studies over a number of samples to obtain a statistically reliable microstructure information.

Chapter 4

Numerical Investigation of waterflooding using micro-CT images of Berea Sandstone core by Finite Element Method ¹

In this chapter, pore scale analysis of oil-displacement by water is presented by using existing Finite Element techniques in COMSOL Multiphysics 3.5a. Berea sandstone is considered as a representative porous medium for a typical oil-reservoir. The pore structure has been extracted from the micro-CT images of sandstone sample of Chapter 3, and two-phase fluid flow is studied in this realistic pore space with water as the invading phases and oil as the displaced phase.

4.1 Micro-CT Images

The preparation of the sandstone sample and extraction of pore-space images using micro-computed tomography were discussed in Chapter 3. A few random images are chosen from the series of micro-CT images for incorporating them as problem domains in *COMSOL Multiphysics 3.5a*. However, certain image processing steps are required before defining these images as real two-dimensional (2D) pore-space.

¹Parts of this chapter have been compiled from the publication in *Energy*, 2010, **35** pp. 5209-5216

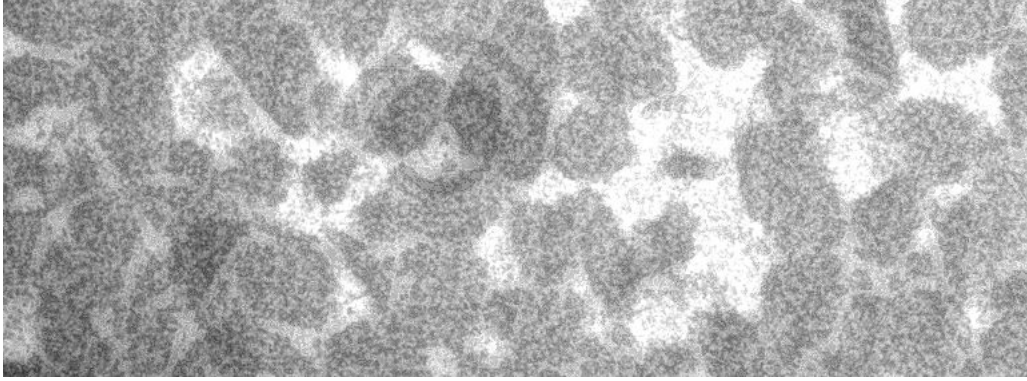


Figure 4.1 – An image representing cross-sectional porous structure at an axial distance of 0.378 mm from the base was selected for the numerical analysis. The image depicts the porous structure using a range of pixel values. Black coloured regions represent solid grains and white coloured regions show pore space.

4.2 Image Processing

One of these random images has been shown in Fig.4.1. It represents a two-dimensional pore structure at an axial distance of $378\ \mu\text{m}$ from the base of the core with a range of pixel values from 0 (white) to 255 (black). The white regions depict void spaces or pores and the black regions depict solid grains. The two-dimensional images of the pore-space in Berea sandstone have been obtained by exposing X-rays of the micro-CT at different horizontal sections along its vertical axis. Similar two-dimensional images can be obtained by changing the axis of micro-CT, when the vertical sections of the rock sample are exposed to the X-ray. In this study, an assumption has been made such that the pore space remains similar in nature for both these cases. However, if one desires, simulations of the displacement of resident oil by water can be performed on the images of the vertical sections. For the sake of simplicity and to demonstrate the efficient use of such pore-scale geometries in numerical simulation, in this study the simulations are restricted to two-dimensional images.

There is a considerable amount of variation in the pixels of the image over a very short distance, making the flow domain extremely complex. Taking into account the computational limitations, a section of the image is extracted from the original image. This image is processed in open source image processing software ImageJ for noise reduction, binary conversion and simplification. As shown in Fig.4.2(a), the final processed image distinctively defines a single

continuous region as the pore space which has been used as the domain for flow simulation. Similarly, based on these steps, other images are processed to obtain different porous geometries. These images are stored as an array of pixels in MATLAB and then with the help of COMSOL-MATLAB interface, they are converted to computational domains and incorporated as computational geometries for this study.

4.3 Numerical Simulation

The computational geometry, governing equations and numerical techniques adopted for solving the two-phase flow in porous media are presented in this section.

4.3.1 Geometry of Porous Medium

The geometry of the porous medium is shown in Fig.4.3. This geometry has been imported from processed image of the micro-CT scan. The maximum dimensions along the X and Y axes are $730 \mu m$ and $450 \mu m$, respectively. Five different boundaries have been considered for the purpose of flooding through the porous medium. These boundaries are identified in the figure.

4.3.2 Governing Equations

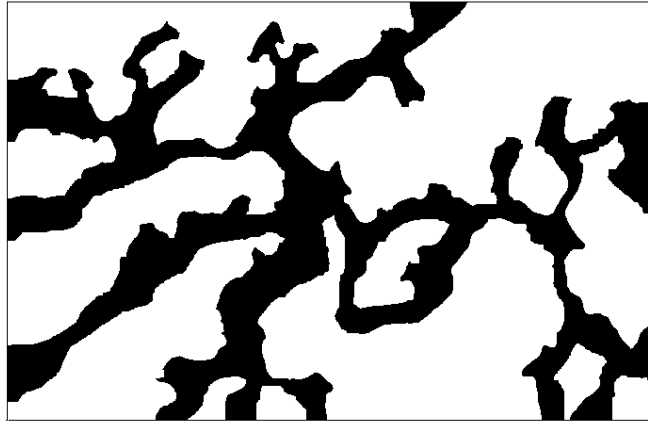
The equations used for developing the mathematical model for flow through the pore geometry are presented here.

Continuity equation

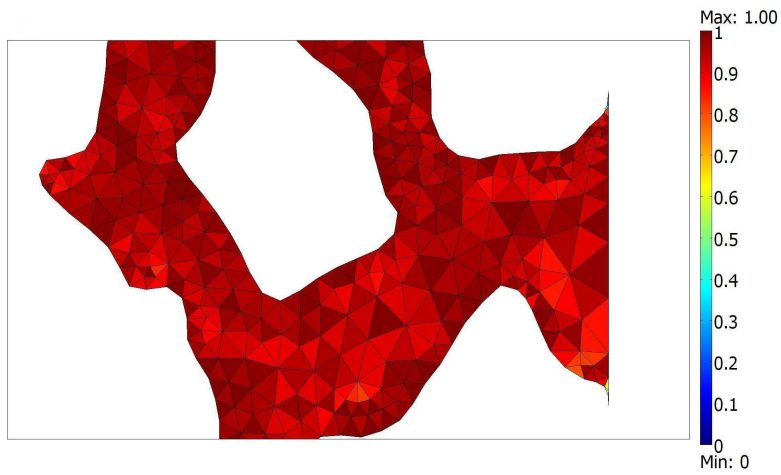
The Continuity equation represents conservation of mass for fluid flow. For an incompressible fluid, the continuity equation can be written as Eq.4.1 (Panton, 2005).

$$\nabla \cdot \mathbf{v} = 0 \tag{4.1}$$

Here \mathbf{v} represents the velocity of fluid flow. The fluid is assumed to be a continuum and incompressible.

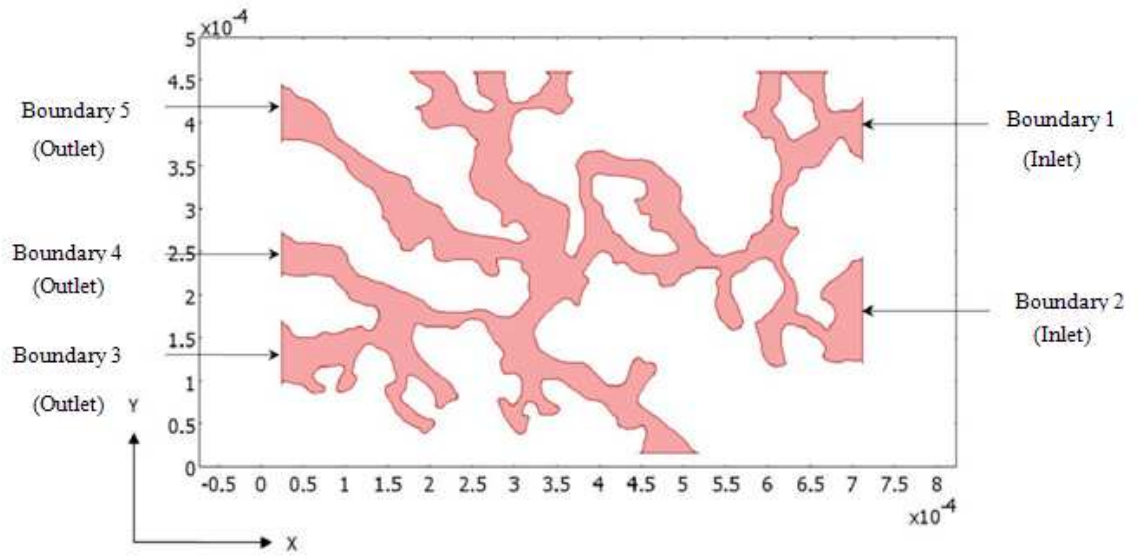


(a)

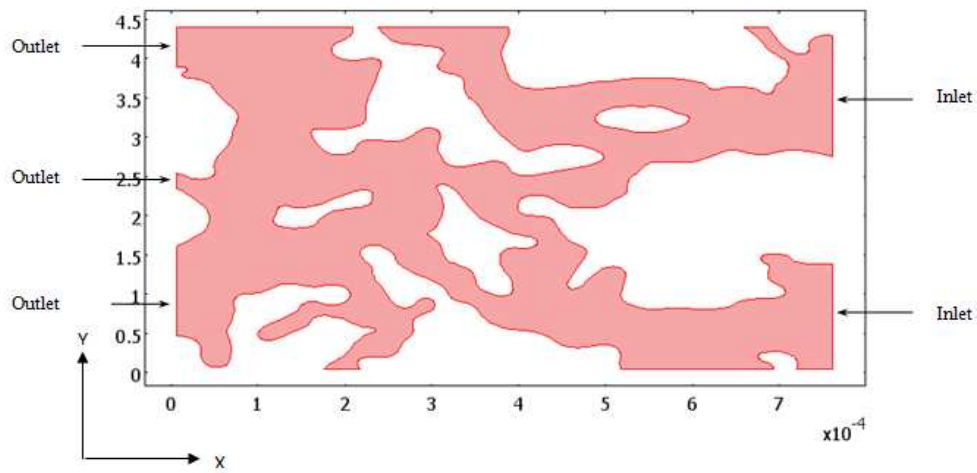


(b)

Figure 4.2 – (a) Pore structure obtained after image processing. White region represents solid grains while black region represents pore space. (b) The same image has been imported into COMSOL and an unstructured two-dimensional mesh is generated in the problem domain.



(a)



(b)

Figure 4.3 – The representative computational geometries used for COMSOL simulations. All dimensions are in meters

Navier-Stokes equation

Navier-Stokes equation represents conservation of momentum for the fluid flow. For an incompressible fluid, this can be written as (Panton, 2005),

$$\rho \left[\frac{\partial \mathbf{v}}{\partial t} + (\mathbf{v} \cdot \nabla) \mathbf{v} \right] = -\nabla p + \rho \mathbf{g} + \mu(\nabla \mathbf{v} + \nabla^T \mathbf{v}) + \mathbf{F}_{st} \quad (4.2)$$

Here \mathbf{v} is velocity of fluid flow, ρ is density of fluid, μ is dynamic viscosity of fluid, p is pressure, \mathbf{g} is acceleration due to gravity and \mathbf{F}_{st} is the term representing interfacial tension force. Fluid is assumed to be incompressible and Newtonian and forces due to gravity are neglected since the entire fluid volume is assumed to be at the same gravitational potential.

Interfacial Tension

Interfacial tension between two fluids in Eq.4.2 is calculated according to the CSF model proposed by (Brackbill et al., 1992).

$$\mathbf{F}_{st} = \sigma \kappa \delta \mathbf{n} \quad (4.3)$$

Here σ denotes the surface tension coefficient, κ denotes the curvature of the fluid-fluid interface and \mathbf{n} is the normal to the fluid-fluid interface. Surface tension is considered to be acting normal to the interface. The interfacial curvature κ , given in Eq. 4.4, is calculated as (Brackbill et al., 1992)

$$\kappa = \frac{1}{|\mathbf{n}|} \left[\left(\frac{\mathbf{n}}{|\mathbf{n}|} \cdot \nabla \right) |\mathbf{n}| - \nabla \cdot \mathbf{n} \right] \quad (4.4)$$

Level Set method

Transient two dimensional numerical simulation of waterflooding in the porous medium is performed by using Level Set method. Fluid volume consists of two immiscible and incompressible fluids which are represented by the auxiliary level set function ϕ . This function is defined such that its value is greater than zero where one of the fluids is present, less than zero for the complimentary volume where other fluid resides and equal to zero at interface of the two fluids. It can also be used to track the interface between the two fluids. The value of level set function is determined by solving an additional passive transport equation.

$$\frac{\partial \phi}{\partial t} + \mathbf{v} \cdot \nabla \phi = \gamma \nabla \cdot \left[\epsilon \nabla \phi - \phi(1 - \phi) \left(\frac{\nabla \phi}{|\nabla \phi|} \right) \right] \quad (4.5)$$

In Eq.4.5, γ denotes the amount of reinitialization or stabilization of the level set function ϕ and ϵ determines the interface thickness between the two fluids. In general, ϵ is half the characteristic dimension of the smallest cell in the discretized mesh of the computational geometry, as shown in Fig.4.2(b). For the present study, the value of ϵ is taken as $5 \mu m$ in order to obtain proper interface resolution.

4.3.3 Boundary and Initial Conditions

Boundary and initial conditions used for the analysis are presented here. Initially, the fluid occupying the pore spaces is oil. Waterflooding takes place through boundaries 1 and 2, as shown in Fig.4.3. Oil is displaced through boundaries 3, 4 and 5. In this study, the inlet or outlet boundaries have been selected in a manner, keeping in mind the actual waterflooding processes. Water is injected from one particular direction of the oil-reservoir. The bulk flow inside the porous media takes place in a specific direction, and accordingly, the outlets for the displaced oil are going to be in the other direction with respect to the inlet. All the solid-fluid interfaces are treated as wetted walls. The normal component of the velocity at the wall vanishes, which is given by,

$$\mathbf{u} \cdot \mathbf{n}_{wall} = 0 \quad (4.6)$$

However, there is a finite slip at the wall, which is imposed for the tangential component of the velocity at the wall through a frictional force formulation. A frictional force is added to the surface elements, which can be written as Eq.4.7.

$$\mathbf{F}_{fr} = \frac{\mu}{\beta} \mathbf{u} \quad (4.7)$$

Here \mathbf{F}_{fr} is the frictional force, μ is the dynamic viscosity, β is the slip length. The value of β is equal to the value of the mesh element size of a boundary element. This is considered as a default value to achieve numerical stability in *COMSOL* simulations with wetted wall boundary condition. The surface normal is calculated in accordance with the contact angle which is provided as an input to the simulation.

The pressure boundary conditions are applied at inlet and outlet boundaries in order to maintain a constant pressure gradient across the porous medium for the fluid flow to take place. Pressure of 1 Pa (gauge) is applied at inlets and 0 Pa (gauge) at outlets. These values are consistent with the length scale over which the pressure gradient is applied which, in this case, is approximately $100 \mu\text{m}$. Thus, the imposed pressure gradient for the simulations is 10^4 Pa/m or 0.1 atm pressure per unit length. The volume fraction of water at inlets and that of oil at outlets is assigned to be unity.

4.3.4 Solution Technique

A commercial finite element based software COMSOL Multiphysics (3.5 A) developed by COMSOL Inc. is used for the simulations. The computational geometry is discretized into number of elements which consists of two-dimensional unstructured mesh, as shown in Fig.4.2(b). The number of elements in the mesh is 6968. The solver uses a finite element based code to calculate the value of velocity, pressure and level set function at each node point connecting two or more elements. A linear system solver PARDISO (Parallel Direct Solver) (Schenk and Gartner, 2004) has been used here. A relative tolerance of 0.01 and an absolute tolerance of 0.001 have been assumed for the time discretization scheme. The time-stepping method uses Backward Differentiation formula (BDF) to determine each time step. Waterflooding starts at the instant $t = 0 \text{ s}$ and the simulations are allowed to run for a period of $t = 10 \text{ s}$. Due to the complexity of the geometry in the micro-scale and the various boundary conditions imposed to the computational domain, *COMSOL* simulations require a minimum of 48 hours of CPU time to obtain a converged solution for a ten second displacement process. Hence, considering the computational limitations, all the displacement simulations are performed for a period of 10 seconds only. Physical properties of oil and water are listed in Table 4.1.

4.4 Results and Discussion

The validation of the numerical model and the results of the displacement simulations for waterflooding are presented in this section.

Table 4.1 – Properties of fluids

Property	Water	Oil
Density ($\frac{kg}{m^3}$)	1000	800
Dynamic Viscosity ($Pa - s$)	0.001	0.075
Interfacial Tension (N/m)	0.0216 (oil-water)	-
Contact Angle	120 ⁰ (oil-water)	-

4.4.1 Validation of Numerical Model

The numerical model is validated by verification of Darcy’s Law for single-phase flow through the computational geometry shown in Fig.4.2(b). Fluid enters the pore space from boundaries 1 and 2 and exits from the boundaries 3, 4 and 5. The fluid flow is pressure driven with a constant pressure gradient maintained across the pore structure.

The variation of velocity magnitude throughout the pore space is presented in Fig.4.4. The average velocity magnitude over the entire domain is $1.33 \times 10^{-6} m/s$. Some regions of high velocity can be observed within the fluid space. The average velocities and the volume flow rates at the five boundaries are listed in Table 4.2. It can be observed that the volume flow rate at boundary 1 ($1.66 \times 10^{-10} m^3/s$) and boundary 5 ($1.07 \times 10^{-10} m^3/s$) is an order of magnitude greater than the corresponding flow rates at the other boundaries. Hence, it can be concluded that these boundaries act as the primary inlet and outlet for the flow domain, respectively. This observation is explained by the presence of regions of constricted cross-section or bottlenecks in the vicinity of boundaries 2, 3 and 4. In spite of the presence of two inlets and three outlets for the flow, 74.19% of the total volume flux through the domain takes place through a single inlet and outlet.

Table 4.2 – Average velocities at boundaries for single-phase flow

Boundary	Average Velocity (m/s)	Volume Flow Rate (m^3/s)
1	1.4×10^{-6}	1.66×10^{-10}
2	4.87×10^{-7}	6.083×10^{-11}
3	2.63×10^{-7}	1.96×10^{-11}
4	4.6×10^{-7}	2.44×10^{-11}
5	1.5×10^{-6}	1.07×10^{-10}

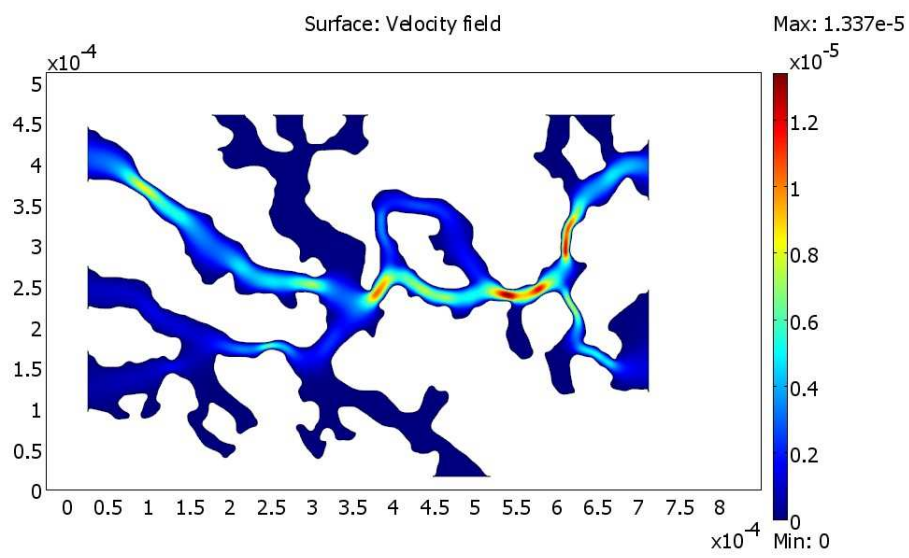


Figure 4.4 – Variation of velocity magnitude in the flow field depicted by a range of colours from Blue to Red. Blue regions represent low velocities while Red regions represent high velocities (in m/s)

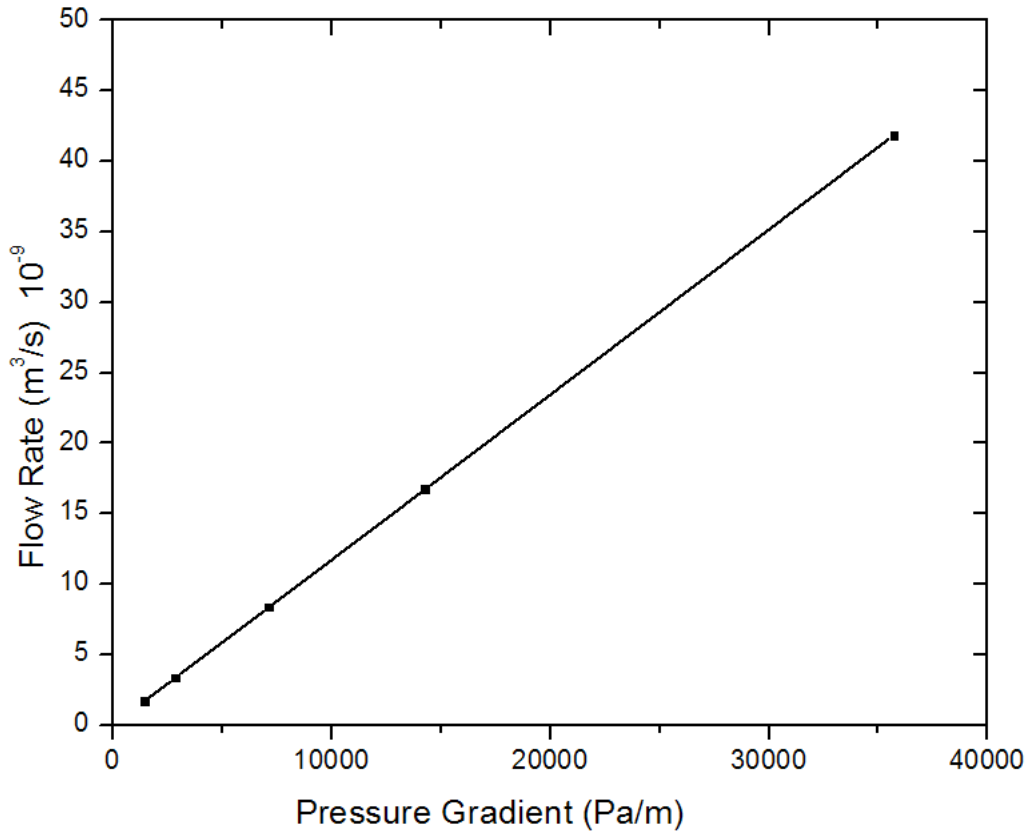


Figure 4.5 – The variation of volume flow rate with the applied pressure gradient. Linear relationship observed in the graph validates Darcy’s law. The value of absolute permeability calculated from the graph is 1.172 mD

Calculation of absolute permeability Numerical analysis of a single-phase flow through a porous medium is performed. In order to validate the mathematical model, a parametric study is performed by varying the pressure gradient across the porous structure and calculating the corresponding flow rates through it. Figure 4.5 represents a variation of these two quantities. It is observed that flow rate varies linearly with the applied pressure gradient. This validates Darcy’s law for the present computational geometry representing the porous structure . The value of the absolute permeability (k) obtained for this case is 1.172 mD . This value of absolute permeability is less than the corresponding measured value of Berea sandstone core used in various sample preparations. An extremely small length-scale of the actual pore space has been considered in the COMSOL simulations, and hence the smaller value of k is explained.

4.4.2 Two-phase Flow: Waterflooding

Two-phase flow simulations are performed for water-oil and the results of these simulations, resembling water flooding in real oil-reservoirs, are provided in the following section. The mathematical model used for the analysis of single-phase flow has been extended further by performing a simulation of two-phase flow of oil and water in two representative computational geometries, as shown in Figs.4.3 (a) and (b), respectively. The purpose of this analysis is to visualize the displacement of resident oil in the pores by the invading phase, which is water in this case. Equations governing the mathematical model are the Continuity and Navier-Stokes equations. Additionally, the level set function has been solved to track the oil-water two-phase interface.

Figure 4.6 shows the invasion of water within the pores of the sandstone sample at different time instants for the computational geometry shown in Fig.4.3(a). Water is present in the pores where the value of density is equal to 1000 kg/m^3 . The remaining pore spaces are filled with oil. The intersection of these two regions can be viewed as the oil-water interface. Position of this interface at various time instances is computed. It is observed that a continuous displacement of oil takes place for a time period of 10 seconds. No separation of the interface is observed. Hence, water has a tendency of moving as a continuous flow front during water flooding.

In order to compare the magnitudes of displacement of oil by water in the different pore geometries, the volume of the displaced oil by the invading fluid water at different time instants are calculated for the two representative geometries in Figs.4.3(a) and (b). In Fig.4.7, it is observed that for the two pore spaces, the volume of oil displaced in 10 seconds follow a separate pattern. In one of the geometries, considerably larger volume of oil is displaced than the other. This displacement depends upon the geometry of the pore space. More number of bottlenecks imply increased resistance for fluid flow, and hence, less oil is displaced in that pore geometry.

4.5 Concluding Remarks

In the present chapter, numerical investigation of waterflooding in a berea sandstone core sample is performed at the pore scale using the high resolution

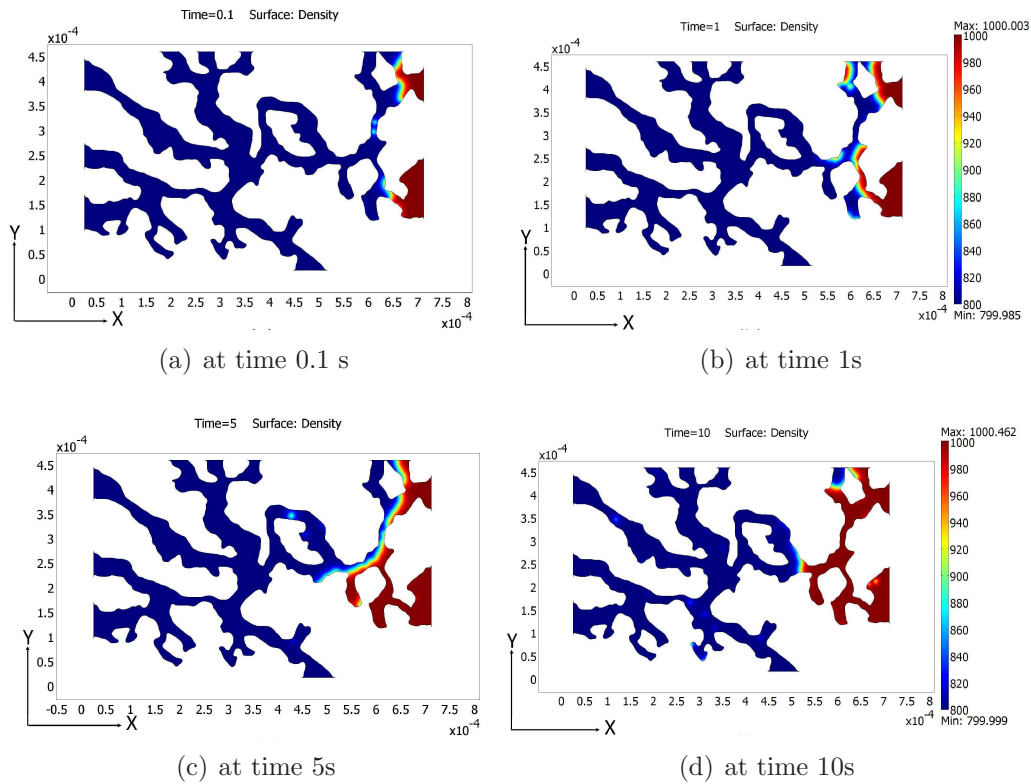


Figure 4.6 – Invasion of water in the pores at different time instants resulting in the displacement of oil.

micro-CT images. Traditionally, these pore-scale simulations are conducted using Pore Network Model and Lattice Boltzmann Method. However, in this work a relatively simpler technique based on finite element method has been implemented where the displacement of oil by water is investigated within the pore structures of a realistic porous geometry derived from the processed micro-CT images. The interface between the two immiscible fluids (i.e., oil-water) has been identified by incorporating the Level Set method within the finite element formulation. The present numerical method has also been validated against single-phase flow. It is found that during waterflooding, the continuous displacement of oil takes place predominantly at preferential inlet and outlet pores. Through this formulation it has been shown that finite element based solver coupled with Level Set method can be an easy and effective tool for the study of imbibition processes which are important for oil recovery.

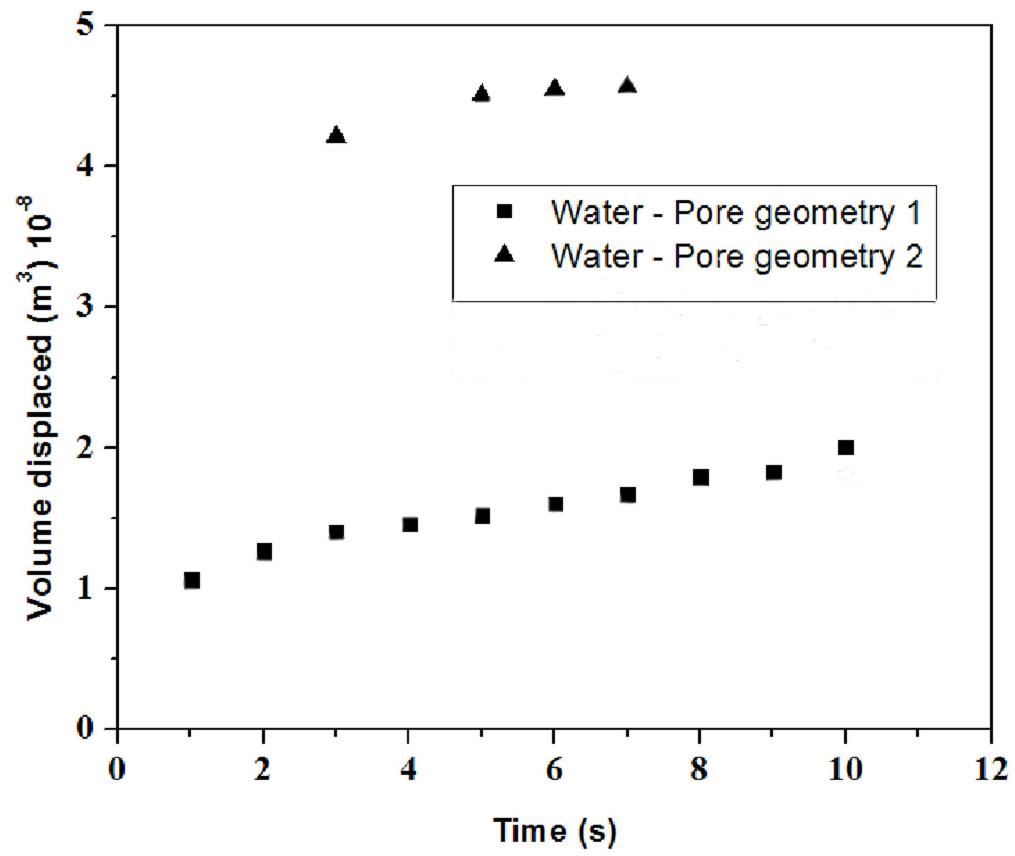


Figure 4.7 – Variation of volume of oil displaced by water with time in the pore spaces.

Chapter 5

Characterization of nanometer scale pore structure in reservoir rock: Carbonate rock ¹

Authentic representation of a pore network based on realistic pore spaces would require more characterization than a single reservoir-rock specimen. As explained in the previous chapters, carbonate sedimentary rock (especially dolomitic limestone) is a widely occurring reservoir specimen. Also, it has been demonstrated by literature review in Chapter 2, that due to the various inherent properties of a carbonate rock, it is more challenging to address the smallest features of a dolomite sample. In this chapter, exclusive sample preparation in FIB-SEM and subsequent characterization is carried out for a carbonate rock specimen. Similar to Berea sandstone, pore space reconstruction and quantitative analysis have been performed for this type of material as well.

5.1 FIB-SEM on Dolomitic Limestone

The preparation of limestone sample from a core, followed by FIB-SEM on selected sites of the sample are discussed in this section.

5.1.1 Material and Sample Preparation

A carbonate core from Turkey was chosen as a representative of porous reservoir rock. To avoid any drift while FIB milling, the final specimen must be

¹Parts of this chapter have been compiled from the publication in *Journal of Microscopy and Microanalysis*, Paper # MAM-11-083, July 2011, *Under Review*.

made compatible with the sample mount. Hence, an 8 mm x 8 mm x 4 mm flat section was sawn off the core. Dolomitic limestone rock is brittle and has a high degree of surface roughness. To meet the requirements of the vacuum chamber in a focused ion beam facility, lapping films of varying size (down to 1 μm) were used on the carbonate specimen to obtain a highly polished surface finish. The sample was then coated with a layer of conductive material to ensure that charging effects did not occur during the collision of the ions or electrons with the specimen. A Denton Gold Sputter Unit was used to sputter a 100 nm layer of gold on the carbonate specimen. Silver paste was used to ground this conductive layer.

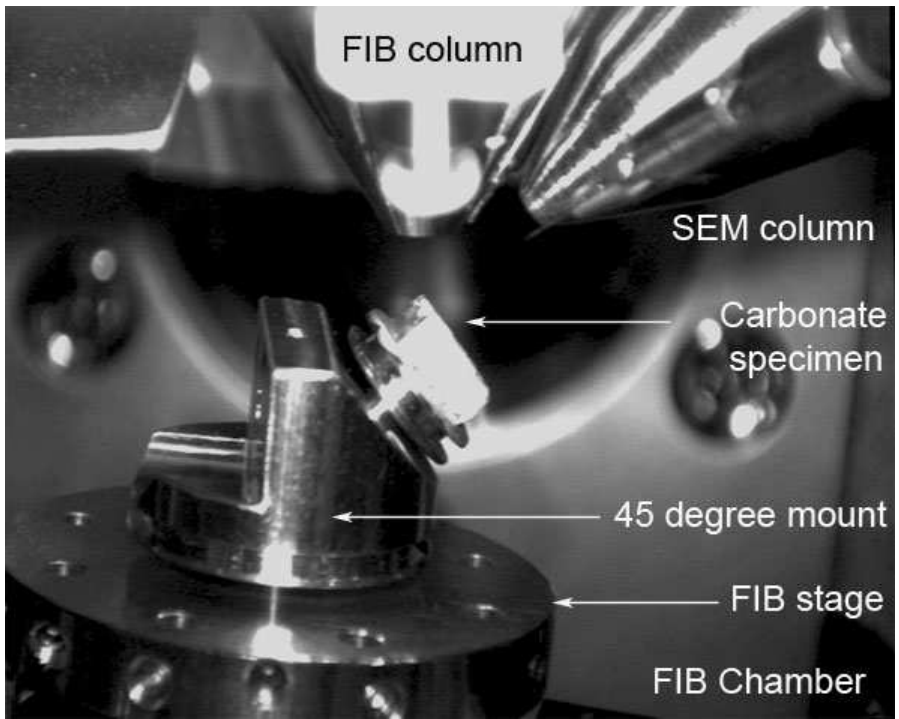
For serial sectioning and imaging, a ZEISS NVision 40 Crossbeam Workstation was employed. Initial attempts to ion mill specific sites of the sample resulted in less depth of trenching and lower resolution than expected. Instead of using the standard sample stage inclination of 54° in the FIB-SEM, a specific mount with a fixed tilt of 45° was selected. The specimen was mounted on this ‘single-specimen mount’, and subsequently the mount was inclined by another 9° so that the total inclination was still 54° . This method was followed so that the edge of the polished surface of the carbonate sample would be directly facing the gallium ion column in the set-up; therefore, charging ions could collide directly with the selected site, reflecting a minimum amount of ions back from the surface, and proper milled surface is obtained. At the same time, the complete surface of the specimen faces the SEM column, and proper imaging during milling is possible. Since we can rotate the inclined stage, this arrangement facilitates looking at various sides of the selected region from all angles. Figure 5.1 shows the carbonate sample mounted inside the FIB-SEM chamber. Two separate sites in this sample, Region A and Region B, were selected for serial sectioning by ion milling.

5.1.2 Serial Sectioning of Region A

After the completion of specimen mounting, the first site for serial sectioning (Region A) was chosen on the top surface. This site was chosen for its reduced roughness over an area corresponding to the size required for milling. Direct FIB milling of a chosen site is very difficult for carbonate samples, and hence extensive sample preparation was performed. Material was first removed from three sides of the chosen area using a probe voltage of 30 kV and probe current



(a)



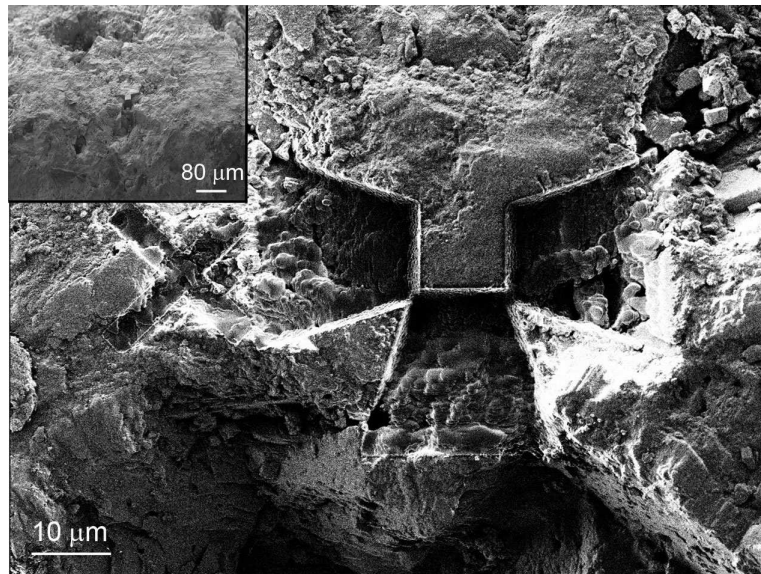
(b)

Figure 5.1 – (a) Carbonate dolomitic limestone rock core (b) The carbonate rock specimen placed on a 45⁰ mount inside the FIB-SEM vacuum chamber.

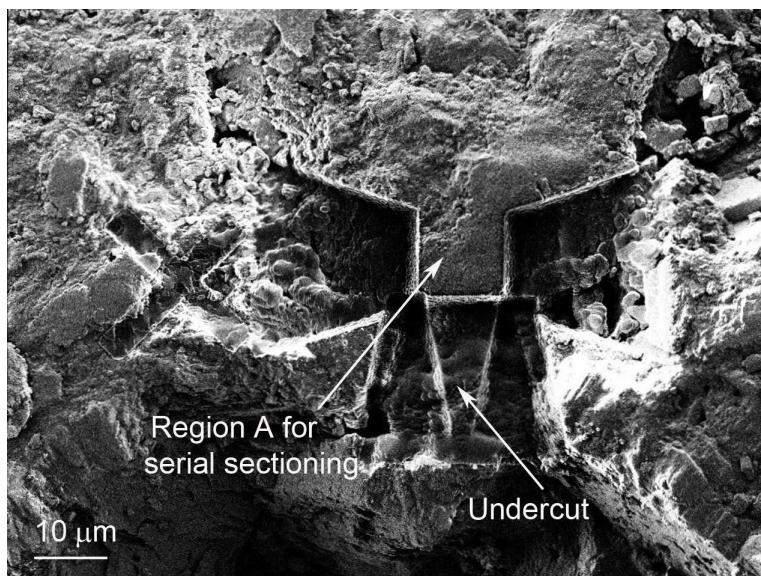
of 13 nA. At each step, an Everhart-Thornley (E-T) detector in the SEM was used to inspect the topography at high resolution and an In-lens detector in the SEM was used to determine the texture of the site. Removing material on three sides allowed an exclusive site to be singled out for serial milling. Figure 5.2(a) shows the area of interest: a $15.90 \mu\text{m} \times 13.70 \mu\text{m}$ rectangular section. The inset shows a view of the overall area at reduced magnification. The depth of Region A available for serial milling was $4 \mu\text{m}$.

A considerable amount of roughness on the front surface of Region A (caused by the trenching process) was reduced by further ion polishing to ensure smooth milling. To remove the roughness in the site walls as well as the undercutting in front of the site, all three sides of the trench were polished at the same probe voltage of 30 kV but with a reduced probe current of 150 pA. The polishing process created an undercut in all three parts of the trench (Fig.5.2(b)), with the more pronounced undercut occurring in front of the surface of Region A. Using the same probe, the undercuts were smoothed by further ion polishing on all three sides of the Region A block (especially in the area near the front surface). The final polish reveals the presence of pores on the prepared front surface, as shown in Fig.5.3(a).

A sacrificial layer is required for FIB serial sectioning to prevent lateral damage to the pore connectivity structure during milling. If there is a protective layer at the top of the carbonate specimen, then any lateral damage is confined to this coating and no pore connectivity data is lost. In addition, we could make alignment marks on this layer without distorting the integrity of the specimen. Images of FIB-milled sections are relatively difficult to align during reconstruction of the pore spaces (because of small displacements in the direction of the ion probe and the corresponding capture of SEM image during serial sectioning). If alignment marks are present and are prominent even after milling, the images of the sections can be aligned with more confidence. The material deposition mode of the NVision40 system was used to coat platinum to a depth of 700 nm on the top surface of Region A (at a voltage of 30 kV and a current of 150 pA). Once the material had been deposited, the probe current was reduced to 80 pA and four adjacent '+' marks were placed on both sides of the Pt-covered surface. Figure 5.3(b) shows the complete prepared sample along with the deposited Pt coating and the fiduciary marks.

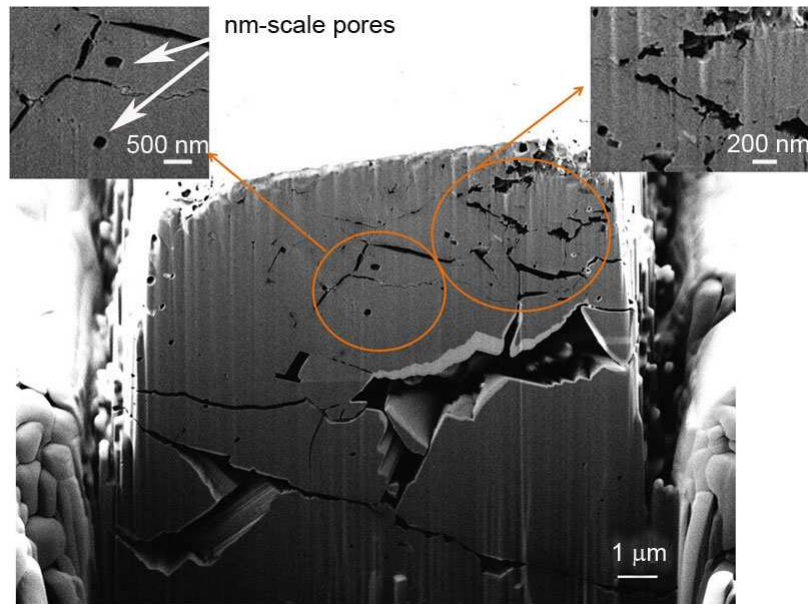


(a)

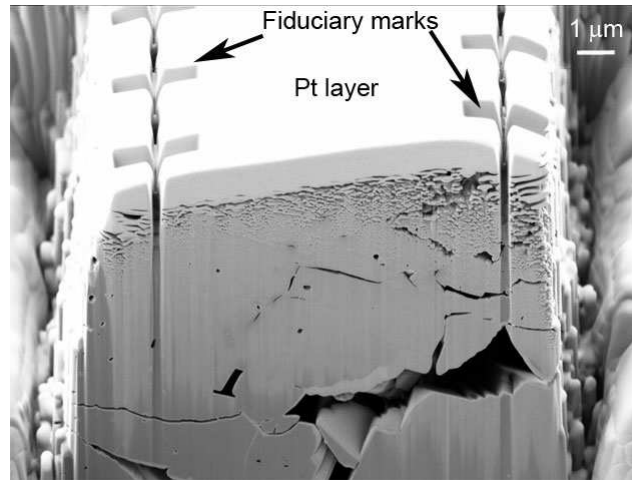


(b)

Figure 5.2 – Preparation of Region for FIB (a) Region A (rectangular peninsula), after material is removed from three sides by ion milling (b) Further ion polishing on the three sides of the site producing undercut at the bottom of the front section of Region A.



(a)



(b)

Figure 5.3 – (a) The front face of Region A after final polishing, with various pores and cracks visible (ranging from a few hundred nms to a few μms in size); inset figures show some of the nm-scale pores at higher magnifications. (b) Deposition of a sacrificial layer of platinum on the top surface, with fiduciary marks milled into the top of Region A.

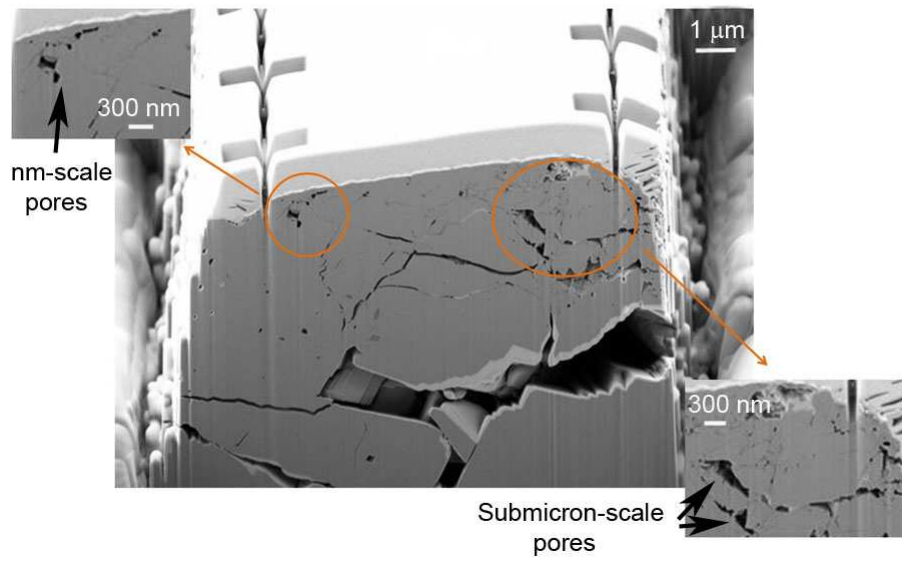
5.1.3 Results: Region A

Milling was performed on the prepared region, layer by layer from the front side of the block inwards. Serial sectioning images of the carbonate microstructure were captured simultaneously by SEM. The Ga^+ ion beam of the FIB was operated at 30 kV and 150 pA. A total of 100 two-dimensional images was captured in the series. The milling resolution was 10 nm, but the SEM images were collected after each second pass of milling, i.e., after each 20 nm and all images were captured using a secondary electron signal detector operating at a voltage of 1-2 kV. Figures 5.4(a) and 5.4(b) show examples of the sections obtained during the serial milling of Region A, revealing microstructure in two different slices. We found void structures within the solid matrix, and the length scale of such structures varied from a few hundred nanometres to 3-4 μm . We also observed that Region A contained continuous crack structures that crossed through a number of sections, with some of the larger cracks being 10-15 μm in length. Often, these cracks connected with porous void structures within the matrix. This type of connectivity was observed throughout the milled sections, with the larger cracks having a tendency to emerge into the bulk pores outside the solid matrix.

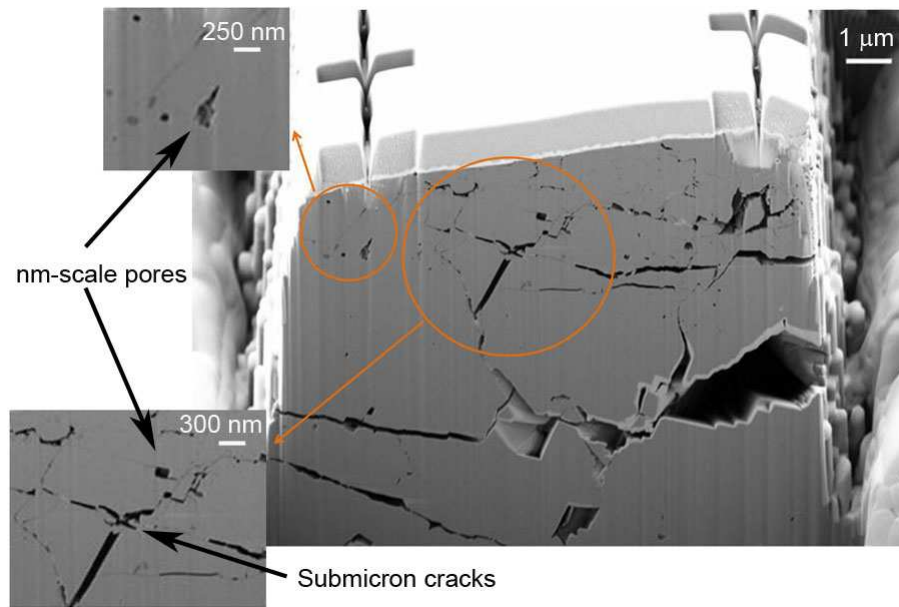
5.1.4 Serial Sectioning of Region B

Crack structures commonly occur in sedimentary rocks and contribute significantly to the porosity and pore connectivity. Since Region A is on the surface of the carbonate specimen, some of the observed cracking might have been generated by the surface polishing process. To avoid any such cracking, a different site (Region B) was chosen approximately 30 μm below the upper surface of the specimen. Region B was also chosen such that the solid matrix at this site is adjacent to a bulk pore or larger void space (Fig.5.5(a)). Thus, we could investigate the pore structure not only where it would be unaffected by our sample preparation methods but also where we could directly observe whether the smaller structures inside a solid matrix were connected with the adjacent larger bulk pores.

This site is prepared in the same manner as Region A (Fig.5.5(b)). The

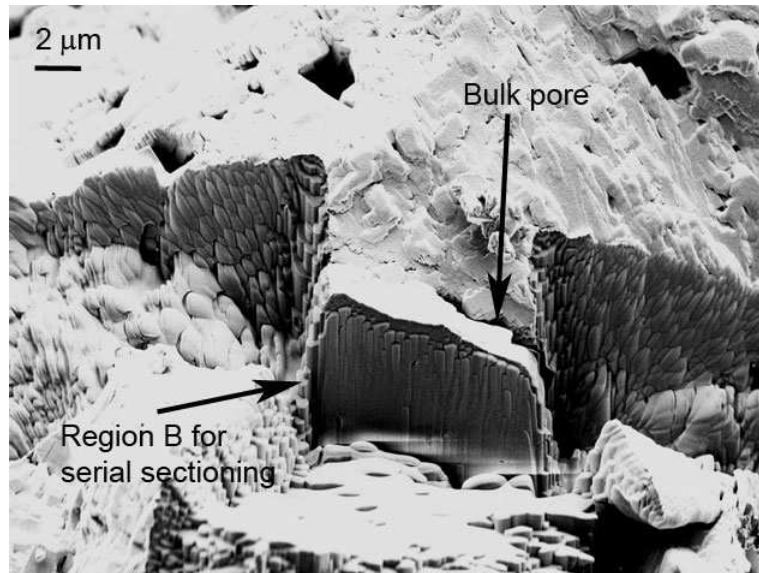


(a)

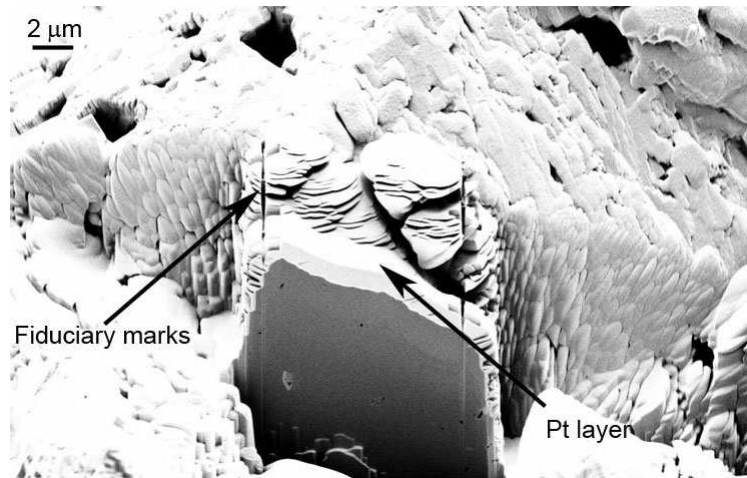


(b)

Figure 5.4 – Sample images obtained during FIB milling of Region A. (a) Pores revealed by serial sectioning (via ion milling) to a distance of 560 nm from the original front surface of Region A. Inset figures highlight the presence of submicrometre-scale pores and crack structures (on the order of a few hundred nanometres in size). (b) Pores revealed at 1260 nm from the original front surface, with insets highlighting nanometre-scale pores and submicrometre-scale cracks.



(a)



(b)

Figure 5.5 – Preparation and sample images of Region B. (a) Region B, chosen 30 μm below the surface of the specimen where a bulk pore was adjacent to the solid matrix. (b) Sacrificial Pt layer deposited on the top surface of this site along with fiduciary marks (as in Region A).

final prepared site had a width of 20.49 μm and height of 15.63 μm , with depth of 5.56 μm available for serial sectioning. The preparation of site was completed by the deposition of a Pt layer (640.3 nm thick using a 150 pA probe current) and the subsequent inscribing of ‘+’ shapes as fiduciary marks on top of the Pt layer. Milling of this section was performed at 30 KV and 50 pA, capturing 163 images in the first pass of milling and 93 images in the second pass. The first pass removed 3.28 μm of material and the second a further 2.28 μm . Figures 5.6(a) and 5.6(b) show examples of the various pore structures encountered during the milling of this section.

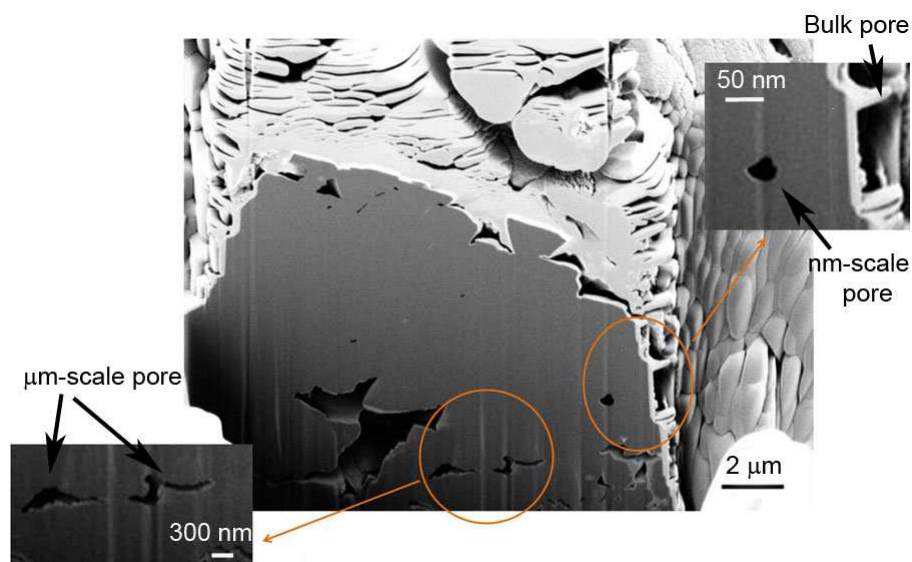
5.1.5 Results: Region B

In Region B, we found small pore structures on the order of 100-200 nm in size. As the milling approached the bulk void structure at the far side of the sample region, pore structures tended to merge within the solid matrix to form voids that were 5-7 μm in size. These large pore structures were found to subsequently propagate towards the bulk pore. The milling of successive slices in Region B clearly showed that many pore structures within the solid matrix were not only connected with the bulk pore but were also connected with each other as well. Some nanometre-scale pore structures, however, did not end up in the bulk pore and did not connect with the pore structures inside the solid matrix. These structures are the isolated or dead pores that are commonly encountered in such porous rock materials.

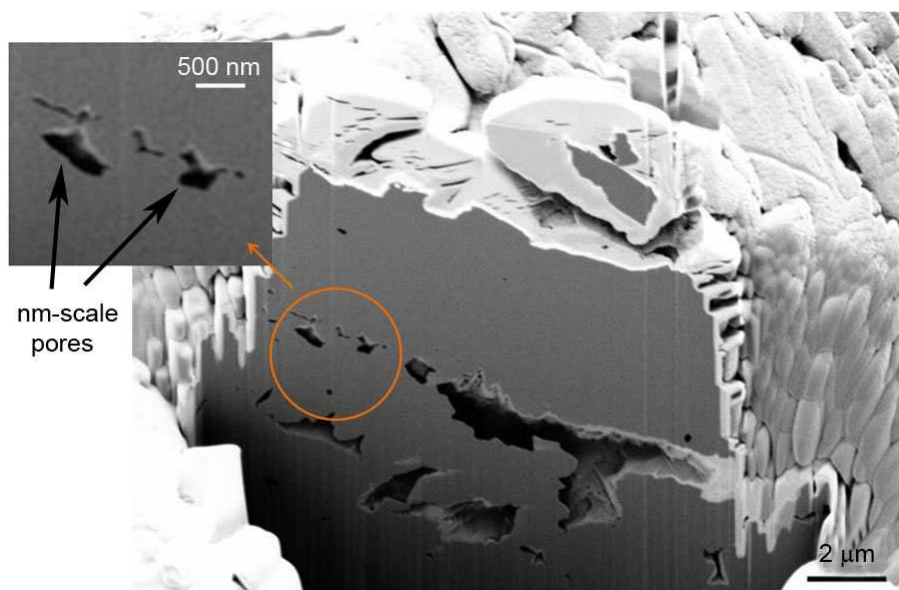
5.2 Three-Dimensional Reconstruction

A 3D reconstruction of the pore space of this carbonate sample was performed to allow the characterization and analysis of pore data. A commercial visualization and image analysis package (Avizo Fire, Visualization Sciences Group, Burlington, MA, USA) was used for this purpose. The operation in each step was carefully chosen and optimized to obtain the most realistic representation of the pore space.

The first step of this reconstruction is the alignment of the two-dimensional images before stacking, using reference points (such as the fiduciary ‘+’ marks on the Pt layer). In the alignment process, corresponding pixels in the series of images were matched to remove errors arising from small deviations in charg-



(a)



(b)

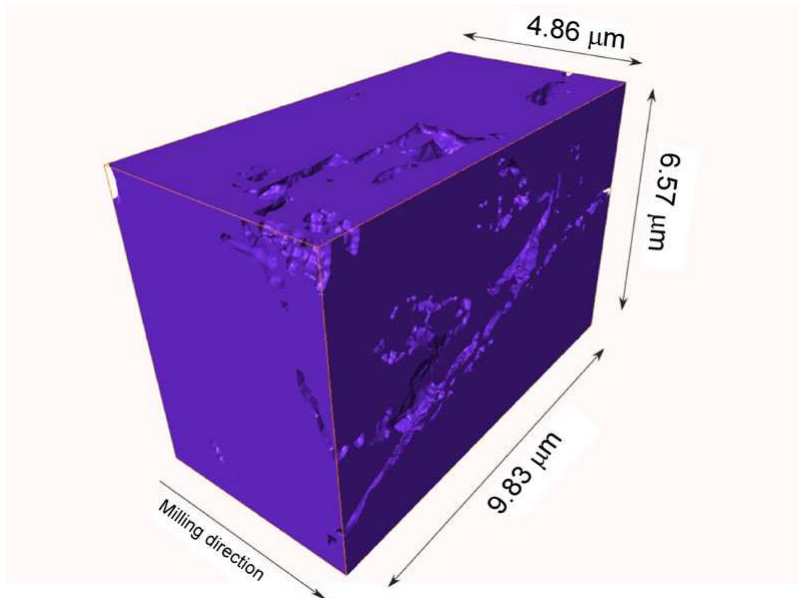
Figure 5.6 – (a) Pores revealed by ion milling at a distance of $2.80\ \mu\text{m}$ inward from the front surface, some of which are found to connect with the bulk pore located next to Region B. Insets show magnified views of nm- and μm -scale pores in the vicinity. (b) The image obtained at $5.1\ \mu\text{m}$ inward from the front surface reveals various pores ($2\text{-}3\ \mu\text{m}$ in size) connecting with each other and also joining with the bulk pore on the outside surface. The inset shows a magnified view of some of the nanometre-scale pores.

ing electrons during capture of images and from drift in the sample during milling operation. After aligning the images, a region of interest was selected in them to define the final volume of reconstructed pore space. During serial sectioning, a gradual reduction of resolution and contrast in these images occurred due to the various factors in a dual-beam system (such as detector noise and curtaining). Hence, proper thresholding of pixel values in the images is required to obtain a reconstruction that was not affected by the inherent distortions of the dual-beam system. A pixel value was assigned to each part of the reconstructed image to discriminate between the solid matrix and a pore. A 2D histogram segmentation technique was then used to distinguish between pixels depicting solid space and pore space. In this method, the gradient magnitude for each image was calculated and the corresponding histogram with respect to intensity was plotted. Gamma correction identifies the solid and pores based on this histogram of respective intensities, and watershed method is applied for the final segmentation of solid and pores. Morphological operation like Closing and Median3d Filter are applied on this final series of images to remove spurious holes (i.e., any pore that were not part of the actual pore structure data of the rock sample.). Figure 5.7(a) shows the reconstructed solid space of the Region B, and Fig.5.7(b) depicts the corresponding pore spaces. In our reconstruction, the voxel size is 10 nm x 10 nm x 20 nm and the final reconstruction block has dimensions of 9.83 μm x 6.57 μm x 5.86 μm .

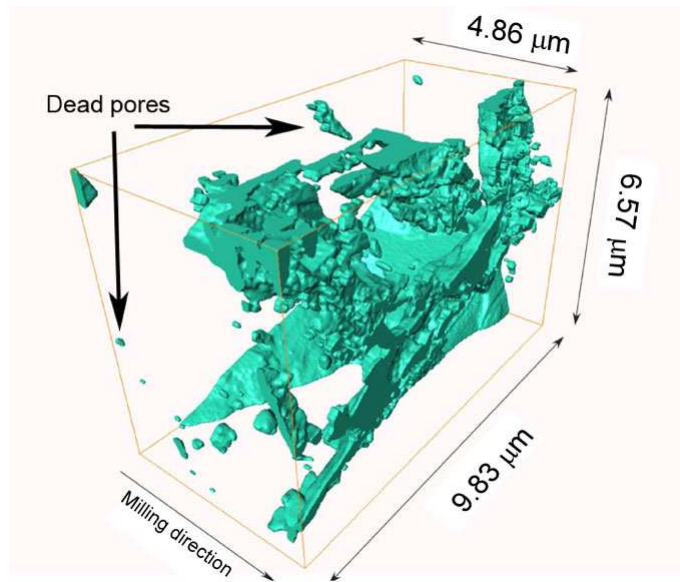
5.3 Characterization and Discussion

Various parameters, including the working resolution and electron range of the FIB system, must be kept in mind during the characterization of the reconstructed pore space. These parameters arise principally from the imaging method adopted and the corresponding equipment used for that purpose. In work related to Berea sandstone, in Chapter 3, it has been discussed in detail how such parameters would affect the perceived microstructure of reservoir rocks.

We calculated that the overall porosity of the reconstructed volume from Region B was 15.29%. According to Hatzor et al., the bulk porosity of such rock samples is $7.98 \pm 5.4\%$ (Hatzor et al., 1999), which is reasonably close to



(a)



(b)

Figure 5.7 – Reconstruction of the pore spaces for Region B of the carbonate sample. (a) A reconstruction of the solid matrix of Region B (inverted from the views presented in Figure 5.6). (b) A reconstruction of the pore spaces in the same region (inverted view), with dead pores highlighted. Nm-scale and micrometre-scale pores are present in large numbers, and the connectivity of many of the pores with the outside bulk-pore is readily observable.

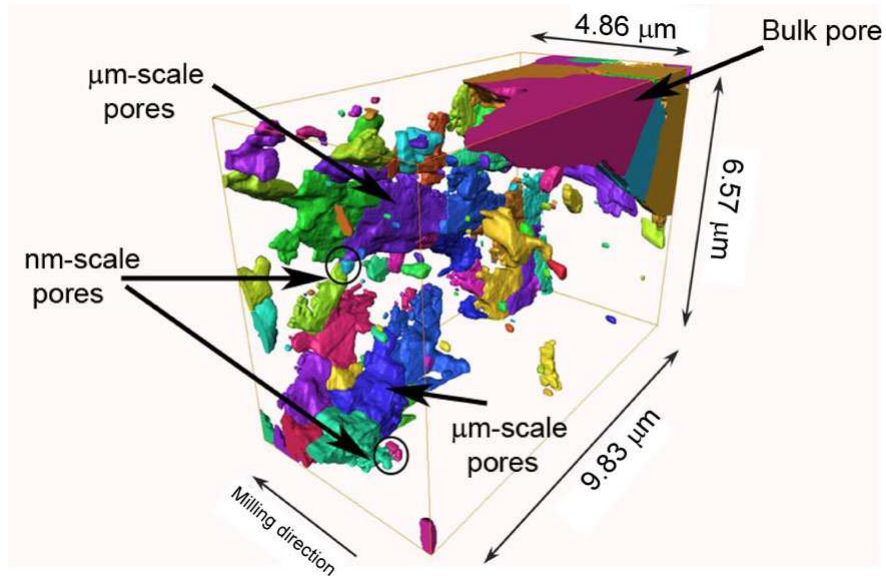


Figure 5.8 – Nm-scale pores found to connect with μm -scale pores and then with the bulk pore outside the solid matrix; the colours in the figure depict the individual pore volumes

the value found in our small sample volume. Our three-dimensional reconstructions (Figs. 5.7(a) and 5.7(b)) showed that nanometre-scale pore structures inside the solid matrix were connected to micrometre-scale structures, which in turn were connected to the larger void structures residing outside the solid matrix. Figure 5.8 shows the connectivity of nanometre-scale pores with the micrometre-scale pores and the bulk pore, clearly indicating the emergence of nanometre-scale pores into adjacent larger pores. The minimum volume of pore bodies in the reconstruction was calculated to be 2000 nm^3 , whereas the maximum pore volume for Region B was $9.55 \mu\text{m}^3$. The presence of pore volume numbers inside this wide range signifies the connectivity among nanometre-scale pores as well as these pores joining the micrometer scale pores.

The variation of number of pores with the individual pore volume has been plotted in Figure 5.9. We observed that the maximum number of pores occurs within the nanometre range of pore volumes (i.e., less than $1 \mu\text{m}$ in size) and that pores over $3 \mu\text{m}^3$ were scarce. This indicates that nanometre-scale pores are likely abundant inside the solid portions of dolomitic limestone samples. Also, many of these nanometre-scale structures were connected with each other and merged into micrometre-scale structures, which in turn tended to

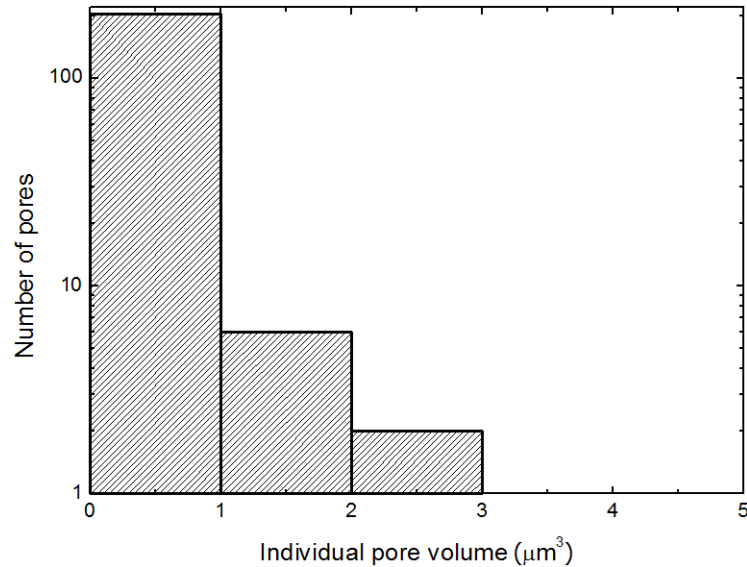


Figure 5.9 – The variation of the number of pores with individual pore volume for the 3D reconstructed pore space

connect themselves with the bulk pore outside a solid matrix. Thus, the reconstructed data corresponded well with the serial-sectioning images, confirming the suitability of the segmentation method used in the reconstruction work.

5.4 Concluding Remarks

Carbonate rocks are one of the principal porous rocks found within oil reservoirs, and understanding their complex microstructure will play a crucial role in developing new methods of extracting the resources. We have presented an in-depth study of the pore structure of a dolomitic carbonate sample analyzed by focused ion beam scanning electron microscopy. Novel sample preparation methods were adopted to explore the nanometre-scale pore structure hidden within the solid sections of the rock. Two different regions were prepared based on their position in the rock sample, and serial sectioning of these regions was performed. The serial sectioning revealed porous structures and cracks ranging in size from nanometres to micrometres within the specimen. Many of these pores and cracks connected with each other and joined with the bulk pore outside the solid matrix. Some smaller structures (on the order of nanometres)

were found to be dead pores, a common phenomenon in such sedimentary rock samples. Reconstruction of the milled region was performed to identify the solid and pore spaces and to analyze the trends in pore connectivity. We were able to calculate the porosity of the reconstructed region along with the smallest and largest pore volumes. Thus, this study provides the first conclusive picture of the pore structure in dolomitic limestone carbonate rocks.

Chapter 6

Fabrication of pore-network structures in silicon and quartz substrates ¹

Once the characterization of various reservoir-rock specimen has been completed, the next step would be fabrication of a micro-model which would capture the geometry of the characterized pore-space. In order to achieve that, the reconstructed pore space should be represented as a pore network consisting of pores and throats. This design of the network and the fabrication of ‘Reservoir-on-a-Chip’ micro-models are addressed in this chapter. The two-dimensional network has been designed by N. Karadimitriou and S. Majid Hassanizadeh at Universiteit Utrecht.

6.1 Experimental Details

This section discusses the design of various pore-throat networks based on the characterization of reservoir-rock cores and the subsequent fabrication of the networks.

6.1.1 Pore-network Design

A key step in the microfabrication process is to fabricate a mask which has the appropriate features replicating a porous medium. To this effort, a 2D pore-throat network has to be designed based on the realistic reconstructed

¹Parts of this chapter have been compiled from the publication in *Journal of Micromechanics and Microengineering*, Paper # JMM/394050/PAP/166956, May 2011, *Under Review*.

pore space of reservoir-cores. It is observed that Delaunay triangulation is a suitable way to represent a typical porous medium in terms of number of pores, throats and their connectivity (Heiba et al., 1986). In this type of triangulation, the length of a throat is defined as the difference between the distance separating the pore-centres and the summation of the individual pore radius. The width of a throat is assigned such that it is always less than (not more than 90%) the smallest pore it is connected to. Two of the related criteria is considered during the design of the width (i.e., the size) of the pore and throat: The pore or throat size in such design should be small enough to introduce capillary flow, but at the same time it should be large enough for probing under microscope. Hence, the mean pore size of the designed networks are varied from 40 μm to 70 μm . The throat-size approximately equal to 40 μm is chosen for better capillary effects with some compromise to imaging capabilities. The throat-size closer to 70 μm would offer less capillary effects coupled with enhanced imaging capabilities.

Once the mean pore size has been selected, choosing the size distribution of pore and throat in the network is the next step of the design. In this work, a log-normal distribution has been chosen initially, which is one of the best representation of a porous medium. However, one of the disadvantages of a log-normal distribution is the inherent narrow shape-profile (Dahle and Celia, 1999). As a result, the size of the throats in the network would be similar to each other. The entrance pressure of fluid in such a throat depends upon its size, and hence same size throats will lead to same entrance pressure, resulting in a faster filling of network by the fluid under experimental conditions than what is observed in reality. Hence, to avoid such anomalous capillary transport, a beta distribution (Keefer and Bodily, 1983) along with the log-normal distribution has been used while designing the size-variation of pores and throats. Beta distribution offers a wider variation in the size of the throats and as a result a wide range of entrance pressure would be achieved during experiments.

Four separate networks with varying number of pores and throats have been designed to reflect the variable porosity and complex geometry of a real sedimentary rock, normally encountered in the oil-reservoirs. The four networks are referred to as Network1, Network 2, Network 3 and Network 4,

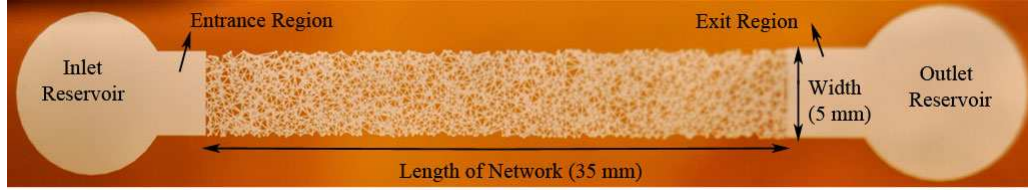


Figure 6.1 – Design of a representative pore-network, with inlet and outlet regions and separate entrance and exit regions

respectively. Network 1 has the least dense structure, with 2000 pores and 6000 throats, with the mean pore size at $40 \mu\text{m}$. For Network 2, the mean pore size remains the same, with the number of pores and throats increased to 3000 and 9000 respectively. In Network 3, keeping the number of pore and throats same as in Network 2, the mean pore size is increased to $70 \mu\text{m}$. Network 4 has a mean pore size of $50 \mu\text{m}$ with 6000 pores and 20000 throats, representing an extremely dense network. It is to be noted that as the number of pores increase from Network 1 to Network 4, the mean distance between two adjacent pores would decrease (from Delaunay triangulation principle). Based on this, the mean pore size has been changed accordingly, so that there is not too many overlapping pores.

Delaunay triangulation routine in Matlab (Mathworks Inc., Natwick, MA, USA) is used for generating the networks. Based on the triangulation steps, the co-ordinates of the pore centres are chosen, and the networks are created. The output from the Matlab routine, in form of pore-throat network, has then been imported to AutoCAD (Version 2010, Autodesk Inc., San Rafael, CA), by using LISP (List processing language). Further, the AutoCAD file containing the imprint of the network is modified to accommodate the inlet and outlet ports and suitable entrance and exit regions located at either side of the original pore network. Figure 6.1 represents the final design of the pore network (Network 1); which consists of the pore-throat structure (35 mm in length and 5 mm in width), rectangular entrance and exit regions (5mm length and 5 mm width) and circular inlet-outlet regions (10 mm diameter). Figure 6.2 ((a), (b), (c) and (d)) illustrates the nature of distribution of pores and throats in the four networks.

Depth of the ROC is another major design consideration, and in this work

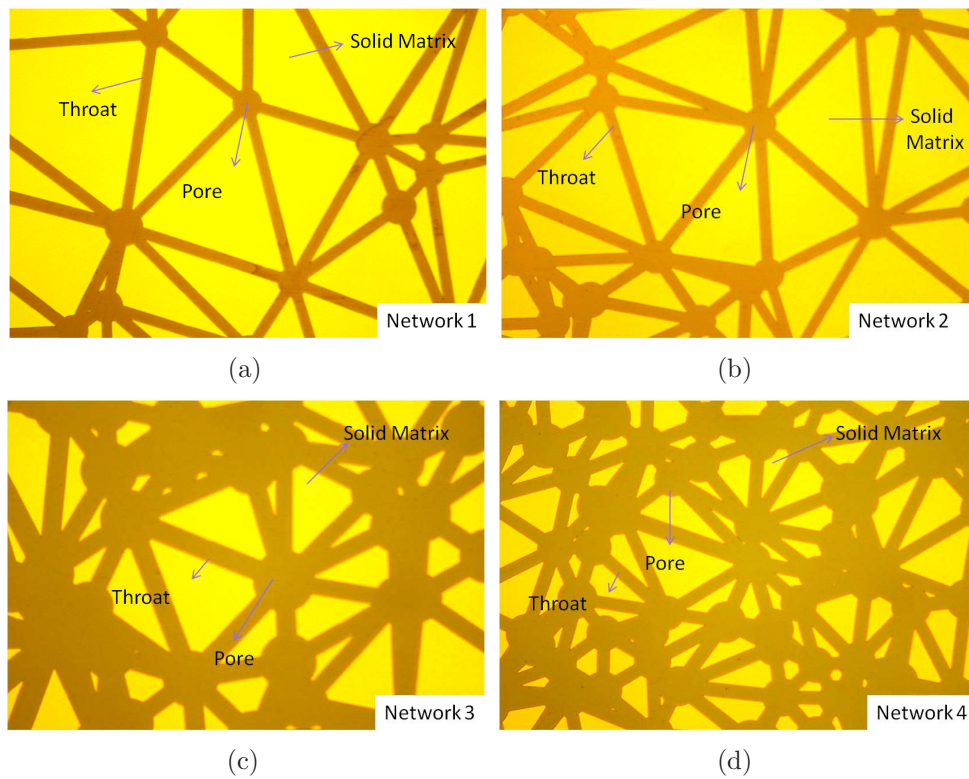


Figure 6.2 – Pores, throats and pore-throat connectivity in different networks
 (a) Network 1 (b) Network 2 (c) Network 3 (d) Network 4

all the networks have been etched to a depth of 40 μm . Thus, the depth of the network is equal to the mean pore size of the networks in Network 1 and Network 2, and the value is also close to the design in Network 3. As a result, during the experiment, the etched depth would not be considerably smaller compared to pore and throat sizes, and hence, is not the dominant factor in determining capillary effect in the experiments. Also, during experiments, visualization of the fluid flow-front is only possible in two dimensions: the length and the width of the network. It is not possible to observe the fluid movement along the depth of the network. Since the depth is same as the mean pore size (for first two networks), we can assume that the fluid movement in the third dimension (i.e., along the depth of ROC) would be similar to that observed in the other two dimensions. Thus, the resultant micro-model from the two-dimensional (2D) network design can be used as an equivalent of a three-dimensional (3D) porous medium/ reservoir during the experiments.

6.1.2 Materials and Fabrication Equipment

The pore-network design, discussed in the previous section, has been used to micro-fabricate the designed structures in (i) silicon (4" diameter circular, 0.5 mm thickness, Silicon Valley Microelectronics Inc., Santa Clara, CA, USA) and (ii) quartz (4" diameter, 0.5 mm thickness, Sensor Prep Services Inc., Elburn, IL, USA). A positive photomask is used for silicon substrates, while a negative one is used for quartz substrates. The photomasks are fabricated on glass (125 mm x 125 mm square plate and 2 mm thick) with chrome coating. L-Edit (Tanner EDA, Monrovia, CA, USA) is used for exporting the pore-network design to the pattern generators (Laser Writer LW405 for positive pattern and Heidelberg DWL-200 for negative pattern of the design) and subsequently the photomasks are fabricated. The covering layer for silicon micro-model is Borofloat glass (100 mm x 100 mm square, 1mm thick) whereas quartz (4" diameter circular substrates, Mark Optics, CA, USA) is used as a covering layer for quartz micro-model. Solitec Spinner along with a CEE Hotplate (Brewer Science Inc., Rolla, MO, USA) is used for spin-coating the photo-resist (HPR506, Fujifilm Electronic Materials Inc., Mesa, Arizona, USA /KMPR 1025, Microchem Corp., Newton, MA, USA) on the wafers and followed by a baking step. Lithography process is performed with a UV mask aligner (ABM Inc., Scotts Valley, CA, USA). Developer 354 and SU-8 developer solution (Microchem Corp., Newton, MA, USA) are used for developing HPR 506 and

KMPR 1025 photoresist, respectively. Inductively Coupled Plasma Reactive Ion Etching (ICPRIE) is used for dry-etching the substrates with the desired pattern on silicon (STS, Newport, UK) and quartz (Alcatel AMS 110, Alcatel, Annecy, France). For removing excess photoresist from the substrates after etching, a Barrel Etcher (Branson/ IPC 3000C) is used. An abrasive water-jet machining station (2652 JetMachining Center, OMAX, Kent, WA, USA) is used for drilling holes in covering layers to provide the fluidic connections to the micro-models. SUSS Bonder (CB6L, SUSS Microtec, Garching, Germany) is used for anodic bonding of silicon to glass and muffle furnace is used for annealing quartz to quartz.

6.1.3 Silicon Micro-model Fabrication

The silicon substrates are piranha-cleaned in a standard piranha solution (H_2SO_4 and H_2O_2 in 3:1 ratio) for 30 minutes and then dried. Coating the substrates with a layer of hexamethyldisilazane (HMDS) ensures a good adhesion between the photo-resist and silicon. Therefore, the silicon wafers are placed in HMDS Oven (Yield Engineering System/YES, Livermore, US) for 17 mins.

A 2.5 μm thick layer of positive photo-resist HPR 506 is spin-coated on the substrates. After spin-coating, the substrate is dehydrated at 115°C for 1.5 min on hotplate as post-spin bake or soft-bake. Then the substrates are kept in open atmosphere for about 30 min, in order to ensure re-hydration for proper exposure and developing of photo-resist during lithography. The positive photomask is used in lithography, and the exposed wafers are developed in Developer 354 for 35 seconds.

STS ICPRIE is used for anisotropic etching of silicon substrates. This method uses SF_6 as the principal gas or etch-gas and C_4F_8 as deposition gas. SF_6 present in the ICPRIE system provides the etchants i.e., F^- ions while C_4F_8 stabilizes the excess of F^- ions, in order to prevent any form of undercut in the desired network. In this process, an etch rate of 4.95 $\mu\text{m}/\text{min}$ has been achieved and a total number of eight cycles is selected, to obtain an approximate final etch-depth of 40 μm . Each cycle consists of etching and then switching of the active gas from SF_6 to C_4F_8 for subsequent deposition. After etching, as the first step of removing photoresist, the etched substrate

is kept in an acetone solution for about an hour. Then, any further presence of resist is completely removed by using a Barrel Etcher for oxygen plasma cleaning. Subsequently, the depth of the micro-model is measured in surface profilometer (Ambios XP 300, Ambios Technology Inc, Santa Cruz, CA, USA) and the average depth of the etched networks is found out to be 40.93 μm .

6.1.4 Quartz Micro-model Fabrication

Quartz wafers are piranha-cleaned and dried in similar manner as silicon wafers. For lithography, negative photoresist KMPR 1025 is used. A 15 μm thick KMPR layer is spin-coated on the substrates. Soft-baking time for quartz wafer is considerably longer than silicon wafers and therefore, these wafers are kept at 100⁰C in hotplate for 10 mins.

Further, the substrates are exposed to UV light under the negative photomask for 17 seconds. Also, post-exposure bake (PEB) is required before developing when using negative photoresists, to complete the photo-reaction initiated during exposure. Hence the exposed wafers are kept in hotplate at the temperature of 100⁰C for 3 minutes. Then, the exposed substrates are developed with SU-8 developer solution for 90 seconds, in order to remove all unexposed photoresist. The substrates are hard-baked in HMDS oven for about 4 hours at 120⁰C.

Alcatel AMS 110 glass etcher is used for the dry-etch of quartz substrates. The etch-gas in Alcatel is C_4F_8 , in an environment where Helium (He) and Argon (Ar) gases are also present. For silicon etching, the etch-gas is SF_6 and no free radical is formed during etching from this etch-gas. Some CF_2 radicals, however, are formed by the deposition gas C_4F_8 . But in the case of silicon etching, a switching always takes place between these two gases (SF_6 and C_4F_8), and when the deposition gas C_4F_8 is inert, these CF_2 radicals are removed. For glass etching, C_4F_8 is the sole producer of F^- ions and CF_2 radicals are formed in the process. Since, this etch-process is continuous, separate time must be assigned for removal of these radicals, else the etching is affected. Hence cleaning steps are associated in Alcatel with every pass of etching and, unlike STS ICPRIE silicon etch, the cycle time for glass dry etch is considerably long.

For the dry-etch of quartz in this work, an etch-rate of $0.4 \mu\text{m}/\text{min}$ (approx.) is achieved. This etch-rate is considerably slower than the etch-rate achieved in STS ICPRIE used for silicon, which contributes to more number of cycles for obtaining the intended depth of $40 \mu\text{m}$. After a total of 10 cycles of etching (each cycle consists of 10 min etch-time or $4 \mu\text{m}$ etch-depth), the substrate is removed from Alcatel. The substrate is left at cold piranha for approximately 24 hours and then treated to O_2 plasma for 30 min, for complete removal of photoresist KMPR 1025. The depth of etching is measured at various locations of the network with the surface-profilometer and it is observed that the average depth is $41.70 \mu\text{m}$.

6.1.5 Drilling Holes for Inlet and Outlet Fluidic Ports

Fabricated micro-models on silicon and quartz, based on the design of pore-network are open networks. For experimental investigation, often a closed micro-model is preferred. It is accomplished by designing a cover layer for this micro-model which consists of holes of 2 mm diameter (on a 1 mm thick substrate), as inlet and outlet ports, as shown in Fig. 6.3(a). Each micro-model has one inlet and outlet on its covering layer, located centrally with respect to the reservoir. The volume of the reservoir along with that of the inlet/outlet port is larger than the volume of the network, and hence, with a suitably chosen volume flow rate, one would achieve laminar flow in the entire pore-network.

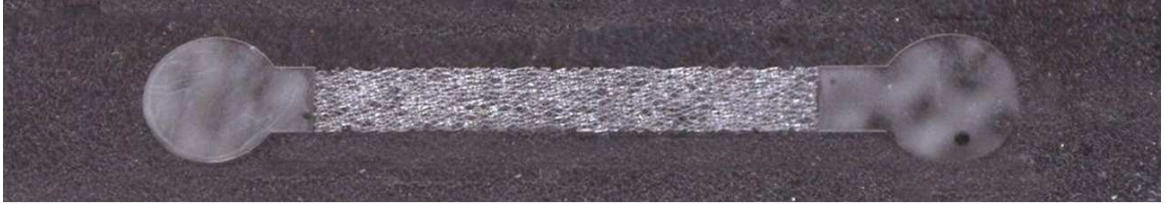
Borofloat glass is selected as the covering material for silicon, and holes are drilled using abrasive water-jet machining process. For quartz substrate, the material of the cover layer is also quartz, as quartz provides better wetting properties, which may be required for performing experiments with the fabricated pore-network.

6.1.6 Bonding of Micro-models

Both the bottom layer with fabricated pore-network and the covering top layer are piranha-cleaned again in similar composition as before (H_2SO_4 and H_2O_2 mixture in 3:1) and are left in this solution for prolonged period (3 hrs.), to make both layers hydrophilic. Anodic bonding of the top layer of glass (with



(a)



(b)

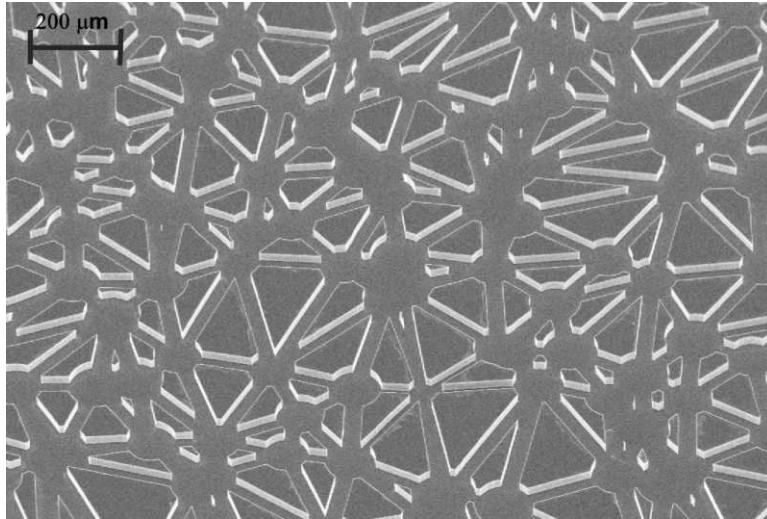
Figure 6.3 – Micromodels fabricated in (a) silicon (with covering layer of glass)
(b) quartz (before bonding with the covering layer)

inlet and outlet holes) is performed in SUSS Bonder with the bottom layer of silicon containing the pore-network. A diamond-saw dicing facility is used for cutting the four networks in four separate micro-models. Figure 6.3(a) shows one of the silicon micro-models, with glass covering layer, while Fig.6.3(b) shows the bottom layer of one of the quartz micro-models (before bonding). Leakage test with water is performed on the closed micro-models, to ensure the feasibility of these chips for conducting micro-scale fluid-flow experiments.

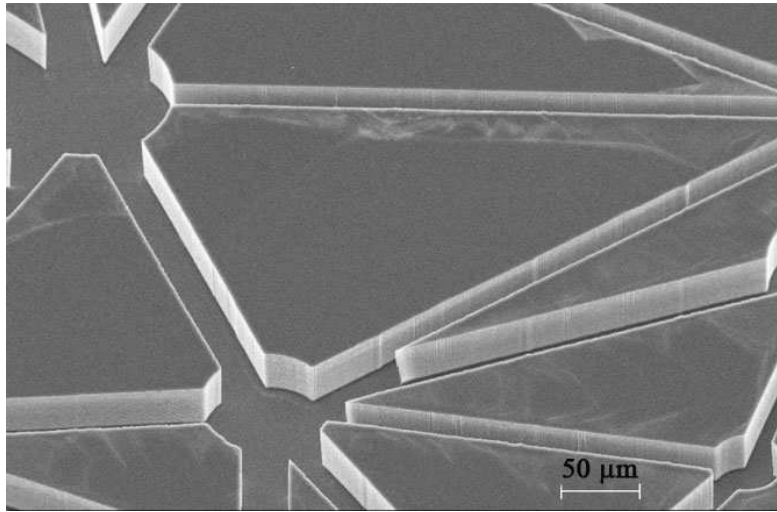
6.2 Characterization and Discussion

Both silicon and quartz network-features are characterized in Scanning Electron Microscope (ZEISS, Germany), before they are bonded with the respective covering layers. The precision of the network is noticed, and subsequently, the pore and throat-size at various places are measured. Also, the depth of etch has been measured at various locations, and compared with the average depth measured in a surface profilometer.

Figure 6.4(a) shows the SEM image of Network 1 etched on silicon substrate. It is observed that the designed pore-structure has been reasonably replicated in the fabricated configuration. Regions with circular cross-section



(a)



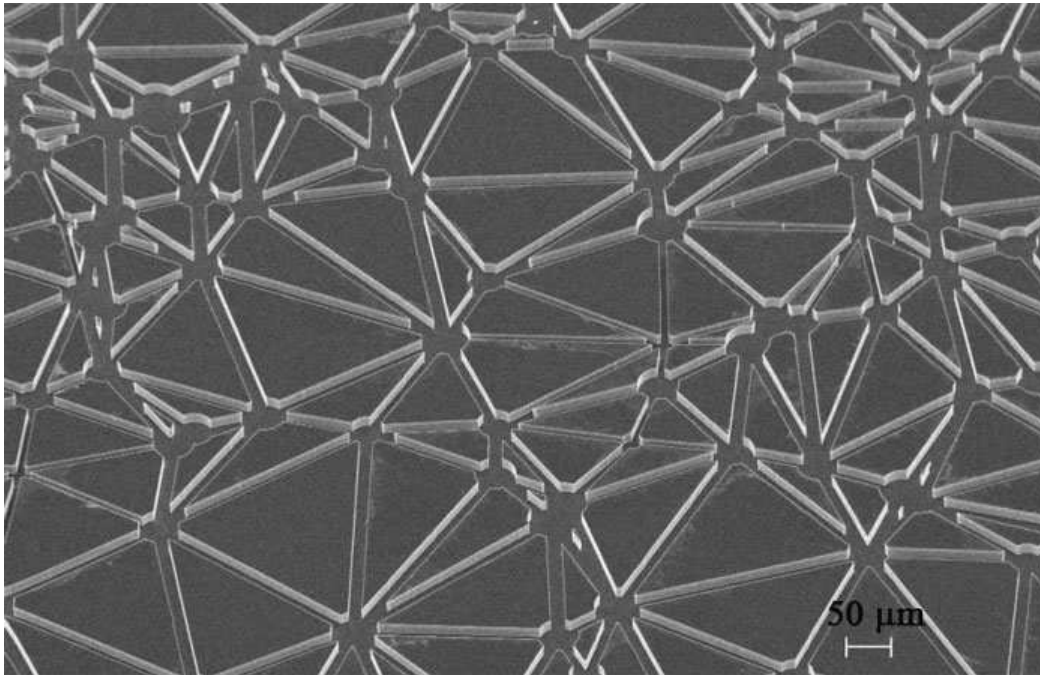
(b)

Figure 6.4 – SEM images of different networks etched on silicon; (a) Network 1; (b) enlarged view of pores and throats on etched silicon networks

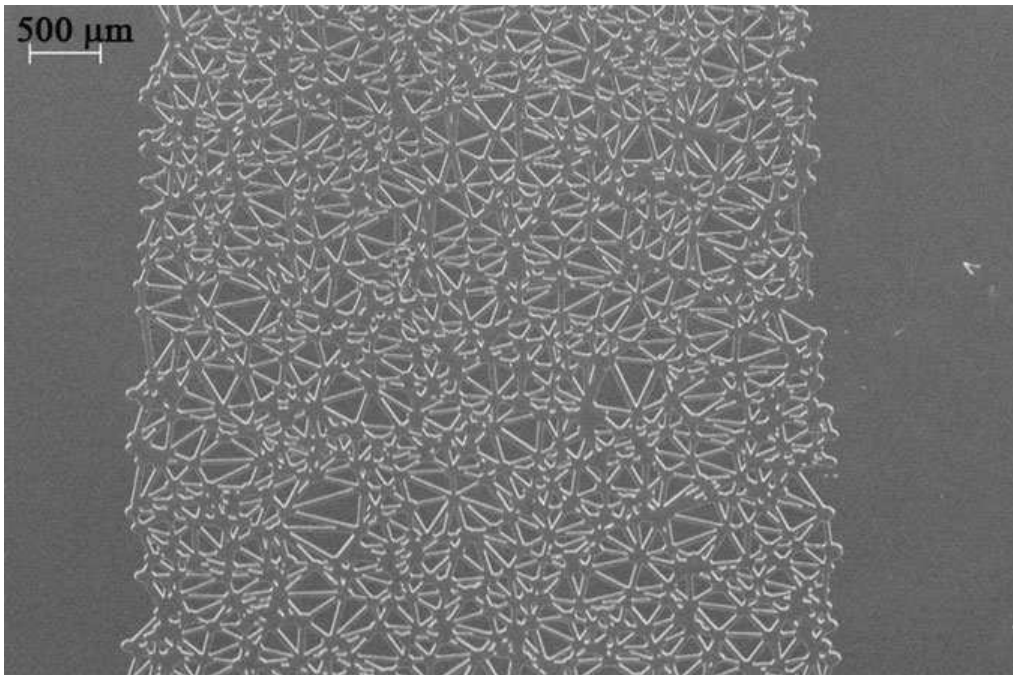
signify the pores, while smaller void shapes with rectangular cross-section denote the throats. A pore in the fabricated micro-model is connected to other pores by these throats (as shown in Fig.6.4(b)), sometimes through a single throat, or by a series of connected throats. Thus, the four fabricated networks with varying number of pores and throats reflect the pore-structure in a reservoir rock, through its complex nature of pore-connectivity. Such complexity of interconnected pore-network is observed in reality by careful characterization of reservoir sample, as conducted by researchers. Figure 6.5(a) shows Network 2 fabricated in silicon (with 3000 pores and 9000 throats) and Fig.6.5(b) represents the most dense network, Network 4, with maximum number of pores (6000) and throats (20000).

The vertical profile of the walls in the pore-network structure is one of the primary goals of this fabrication process. As measured from the SEM images, the walls are reasonably perpendicular to the pore-network base. Figure 6.6(a) shows the angle measured at a random location of the network, and it is found to be almost vertical. Figure 6.6(b) represents the SEM image of an isolated unetched section (depicting a solid matrix in the porous medium) between the etched parts, and the measured vertical inclination for this wall is 84.5° . It is exceedingly difficult to achieve a vertical profile in the wall of such isolated structures, due to presence of ‘undercutting’ during the fabrication process. As a result of undercutting, there is more etching at the bottom of the wall and that produces slanting walls for the pore-network. However, through careful fabrication procedures outlined earlier, it can be concluded that vertical walls in the pore-network are obtained by this silicon microfabrication technique. The Entrance regions play an important role for performing experiments with micro-models and Fig.6.7 shows the entrance region of the fabricated pore network (Network 2). As expected for these regions, vertical conformity of the walls are also obtained.

Similarly, the characterization of the quartz micro-models is performed with SEM. Figure 6.8(a) shows Network 1 etched on quartz substrate, with the enlarged view of the same network provided in Fig.6.8(b). It is observed that the designed pattern of pores and throats are transferred reasonably well to this micro-model. Measurement of the pore/throat structure at randomly chosen areas has been carried out in this network (as shown in Fig.6.8(c)).

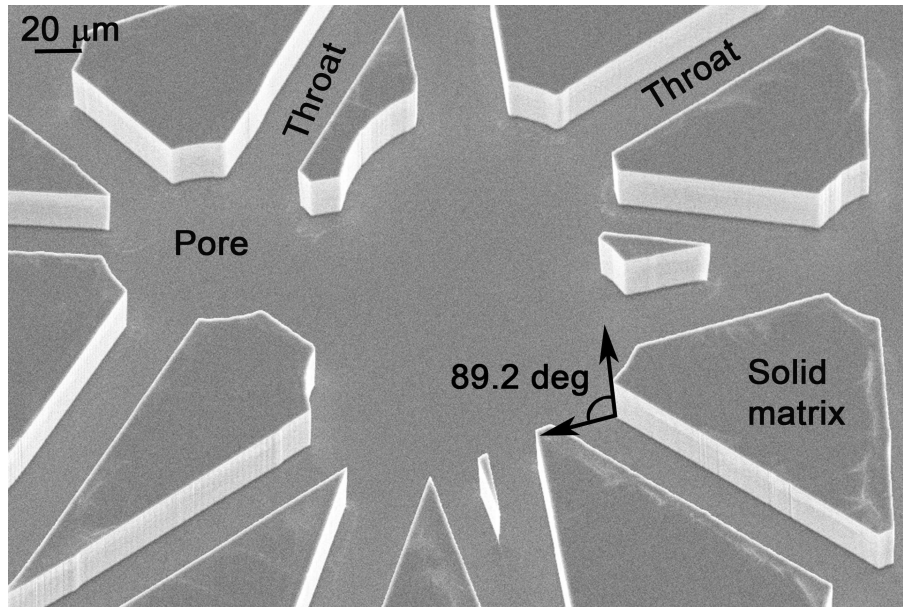


(a)

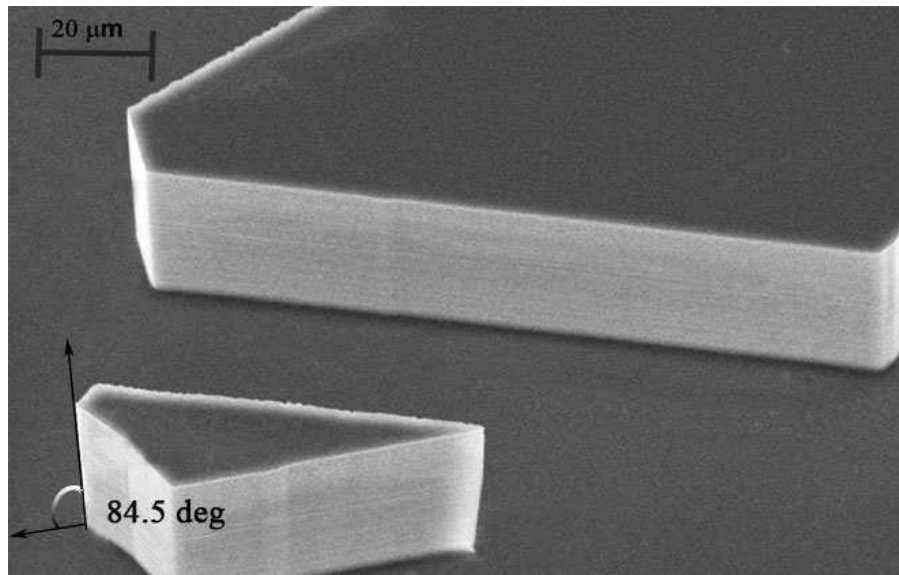


(b)

Figure 6.5 – SEM images of different networks etched on silicon; (a) Network 2; and (b) Network 3



(a)



(b)

Figure 6.6 – SEM characterisation of vertical wall-profiles in silicon network micro-model; (a) near-vertical wall-profile obtained in network, fabricated on silicon (b) contour profile of wall in an isolated solid matrix

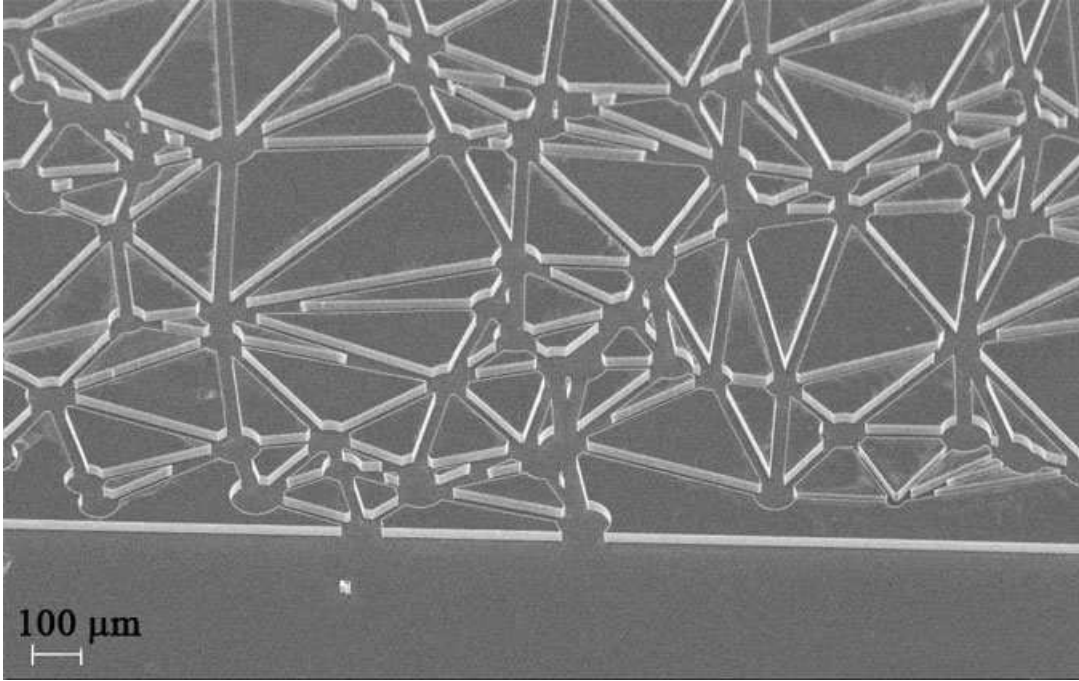
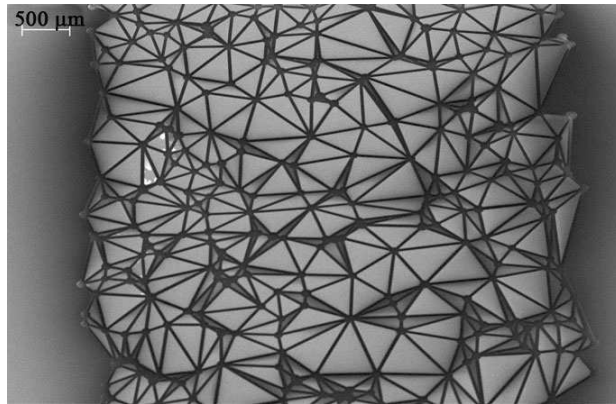


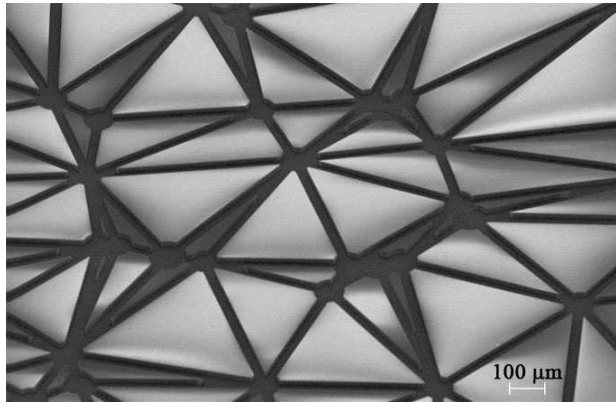
Figure 6.7 – Entrance region of Fabricated network: Starting location of Network 2 from the inlet side

The average size of such structures is approximately equal to the designed mean pore size of $40\ \mu\text{m}$. For all fabricated quartz networks, the wall-profile is measured and they are observed to be close to vertical (for e.g., 90.2° as shown in Fig.6.8(c)).

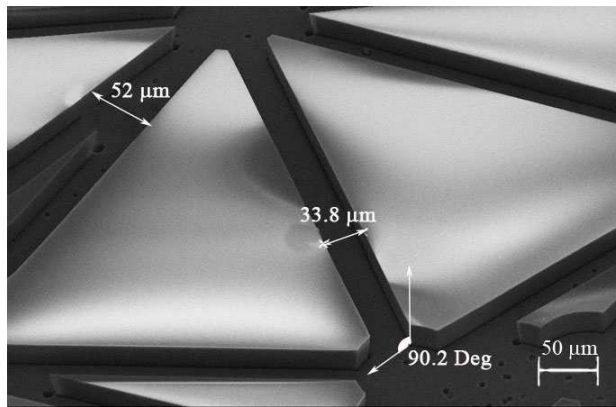
Figure 6.9(a) shows magnified SEM image of Network 3, depicting the pores and their connectivity. As in previous cases of Networks 1 and 2, the wall-profile in this network is found to be almost vertical (for e.g., 89.2° as shown in Fig.6.9(b)). Figure 6.9(c) shows the SEM image of the entrance region in Network 4. It is observed that the design is suitably replicated and the vertical wall-profile is maintained throughout the network. One such representative angle, measured in the region between the inlet reservoir and the pore-network, is 90.6° , as shown in Fig.6.9(c). Pitting effects are pronounced in these quartz micro-models with corroded holes present in the etched regions. This phenomenon is common in quartz fabrication, and since the size of these pitted holes are much smaller compared to the dimensions of the network, it does not increase the volume of the network significantly.



(a)



(b)



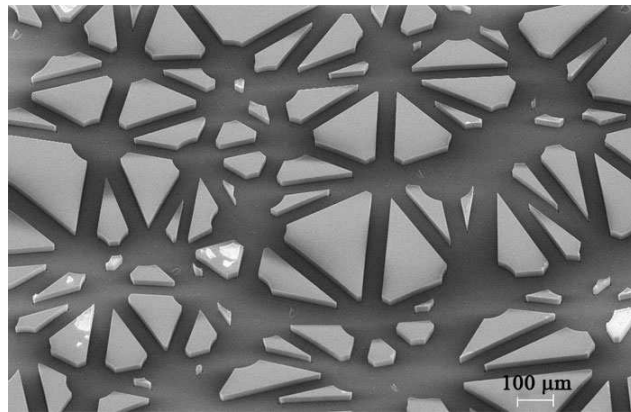
(c)

Figure 6.8 – SEM images of etched quartz micro-model; (a) Network 1 etched on quartz; (b) enlarged view of Network 1 in SEM; (c) feature sizes measured for Network 1

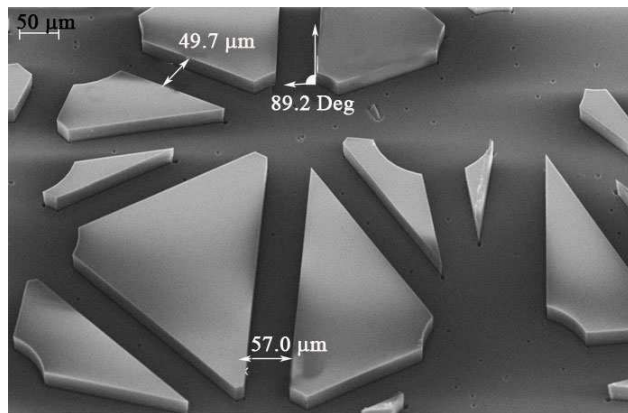
Both silicon and quartz micro-models are characterised using a surface profilometer. Parameters like mean depth of the network, width of the networks and also surface roughness of etched features are measured. The final depth is slightly higher than the desired $40 \mu\text{m}$. This small deviation can be attributed to the increased etch-rate during the etch-process, especially in quartz. The longer than usual etch-time in Alcatel increases the F^- ion density, and with time, this excess presence of ions increases the etch-rate. The roughness in the micro-model is measured in terms of average roughness and this roughness is observed to be in the order of 6-10 nm. Hence, it can be concluded that the roughness of the network is minimal compared to the depth of etching. These parameters are measured at several points (inlet and outlet regions, reservoirs and especially within the network) and average values are calculated. Table 6.1 compares the average values of these parameters for silicon and quartz micro-models. The higher value of roughness in quartz, signifies the presence of the corroded pits. Figure 6.10 represents an example of surface-profile for Network 1 in silicon micro-model. Figure 6.10(a) shows the profile at entrance region of this network, and as desired, the depth remains constant throughout the width of the network. Figure 6.10(b) shows the surface-profile inside the network, and a larger variation of depth is observed in this case, with the deepest trench roughly at $42 \mu\text{m}$. Some features are at a lower depth than the desired depth of $40 \mu\text{m}$. It is to be noted that these features have much smaller width than those with a depth nearer to $40 \mu\text{m}$. The aspect ratios at these locations are very high and due to the limitation in stylus size of the profilometer, it is not possible to traverse these sections accurately.

Table 6.1 – Surface profile parameters of fabricated networks on silicon and quartz

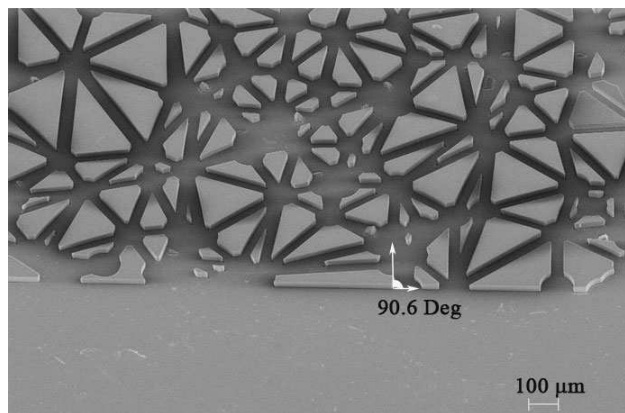
Material	Network	Width(mm)	Mean Depth (μm)	Average Roughness (nm)
Silicon	1	4.89	40.44	4.54
	2	4.95	40.76	6.17
	3	4.96	41.44	6.24
	4	4.96	41.10	6.67
Quartz	1	4.92	41.70	8.77
	2	4.87	41.27	9.26
	3	4.89	42.03	9.23
	4	4.98	41.68	9.93



(a)



(b)



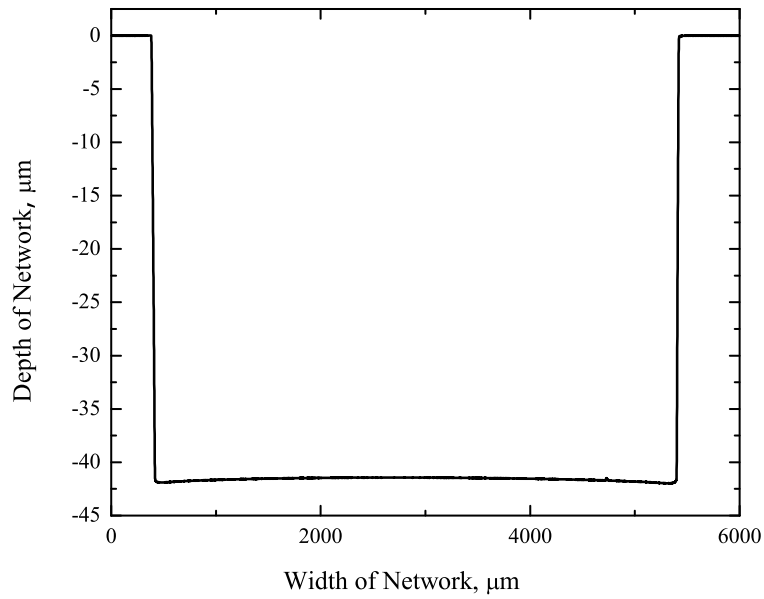
(c)

Figure 6.9 – SEM images of Network 3 and Network 4 of etched quartz micro-model; (a) Network 3; (b) various profiles in an enlarged section of Network 3 (c) entrance region of Network 4 and measurement of wall profile at the entrance region

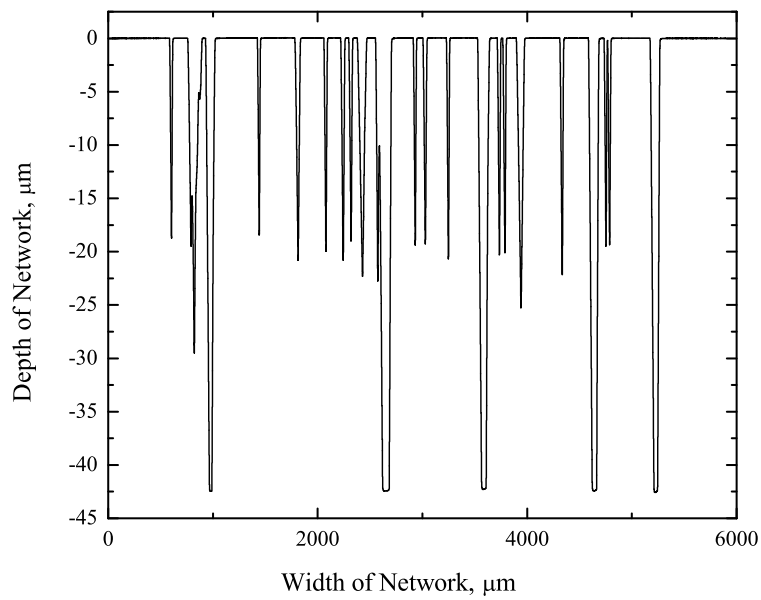
The time required for fabricating these micro-models in silicon, is relatively less than the quartz micro-models. Also, the silicon fabrication procedure is a cost-effective method of realizing realistic pore-networks with precisely designed structures. The quartz fabrication, on the other hand, achieves a depth of 40 μm for such a complex network, whereas the common practice for etched models in quartz is to limit the depth to a few microns. It is difficult to achieve vertical wall-features with wet-etching (both in silicon and quartz), as ‘under-cutting’ would affect the wall-profile in silicon, and isotropic etching would fail to produce desired features in quartz. Hence, dry etching techniques have been followed throughout this work. Compared to silicon, it is expected that the quartz micro-models would offer better visualization of fluid flow through the pore-network, due to their optical transparency, if these micro-models were to be used in fluidic experiments.

6.3 Concluding Remarks

In this chapter, fabrication of silicon and quartz micro-models using dry-etching techniques has been described. The pore-networks in these micro-models signify real reservoir-rock pore-structures, with different number of pores and throats to signify the complex nature of such structure. Four different networks are fabricated with number of pores varying from 2000 to 6000, while the number of throats varies from 6000 to 20000. Anisotropic etching in ICPRIE helps to achieve vertical wall-profiles, and hence, the fabricated pore-networks are approximately 40 μm deep. Covering layers with inlet-outlet ports for these micro-models have been designed and fabricated. Glass and quartz covering layers have been bonded with silicon and quartz network layers, respectively. Scanning electron microscopy is performed to characterise the micro-models. It is observed that pore structures have been replicated with reasonable accuracy, with their size close to that of designed pore-network. Various parameters of etched network, such as mean depth, average roughness have been measured using surface profilometer and these parameters have been compared for networks on silicon and quartz. It is noted that the silicon micro-model is a cost-effective way for fabricating different realistic pore-networks. Quartz micro-models, on the other hand, is fabricated with a depth of approximately 40 μm and provides optical advantages during visualization of fluid-flow experiments. The fabrication recipe developed in



(a)



(b)

Figure 6.10 – Representative surface-profile characterisation of networks by surface profilometer. Figures depict variation of network depth along the width for silicon (a) at entrance region of Network 1 (b) at a randomly chosen place in the Network 1

this work can be successfully applied to fabricate such complex pore-network structures representing natural porous media in silicon and quartz.

Chapter 7

Reservoir-on-a-Chip: Waterflooding experiments ¹

The successful fabrication of pore network microfluidic device described in Chapter 6 has been evaluated in this chapter. Waterflooding experiments in ‘Reservoir-on-a-Chip’ fabricated on silicon substrates have been described , to displace resident oil phase.

7.1 Realization of Reservoir-on-a-Chip (ROC)

In this section, the realization of the conceptual map for fabricating Reservoir-on-a-Chip (described in Chapter 1) is re-visited. In Chapter 3 and Chapter 5, the characterization of reservoir-rock cores using methods such as micro-computed tomography (micro-CT) and Focused Ion Beam-Scanning Electron Microscopy (FIB-SEM) has been demonstrated. These well-defined methods are followed for investigating the pore space in a sandstone/carbonate dolomitic core, some of the principal oil-bearing rock specimens. The pore space of these naturally occurring reservoir-rock materials has been quantified in terms of porosity, pore connectivity between pores of various shape and size as well as pore-volume distribution.

Once FIB-SEM is used to characterize the internal micro-structure, the obtained pore-structure data has been reconstructed by using the image analysis softwares (for e.g., Avizo, Tomography etc.). The obtained three-dimensional (3D) reconstructed pore-space is a result of extensive image-processing steps,

¹Parts of this chapter have been compiled from the publication in *Lab on a Chip*, Paper # LC-ART-06-2011-020556, June 2011, *Under Review*.

which capture the most realistic representation of a reservoir. Using maximal ball algorithm (Al-Kharusi and Blunt, 2007) and triangulation (Heiba et al., 1986), this pore-space has been converted to a network containing pores and throats. Such network representation of the porous reservoir is more realistic than adhoc attribution of pores and throats to a pore network model or representing the porous medium as packed bed of spheres or sand grains. A section of this pore-network can be selected, in order to obtain a two-dimensional (2D) network, which has been transferred into a microfabrication process. Appropriate microfluidic connectors can be designed on the microfabricated chip for subsequent experiments related to water flooding.

Thus, keeping intact the essence of a real reservoir-rock, the pore-network is fabricated on silicon substrate based on the state-of-art microfabrication techniques. The details of the fabrication of this microfluidic device (micro-model) has been discussed in detail in Chapter 5. This novel device has been termed ‘Reservoir-on-a-chip’ (ROC). Figure 7.1 illustrates the conceptual mechanisms of converting a reservoir-rock specimen to an ROC, which facilitates the investigation of the pore-scale transport pertaining to oil recovery processes in reservoir engineering.

7.2 Experimental Section

A complete realization of the ‘Reservoir-on-a-Chip’ can be achieved once the fabricated ROC is used to perform recovery experiments, analogous to those done in traditional core-flooding and reported micro-model experiments. In this section, the water-flooding experiments with ROC, and the subsequent recovery data have been discussed.

7.2.1 Waterflooding Experiments

The experimental set-up for waterflooding with ROC (Fig.7.2) includes a microscope (180x magnification, 1.3M pixel CMOS image sensor, ViewSolutions GE-5, Howard Electronic Instruments Inc., El Dorado, KS) for visualization of oil/water phases in the ‘Reservoir-on-a-Chip’. The ROC is placed inside a custom-made casing, with microfluidic connectors attached, for controlling fluid flow and efficient visualization. We illuminated the ROC using light source from the top to capture high-resolution videos and images of fluid trans-

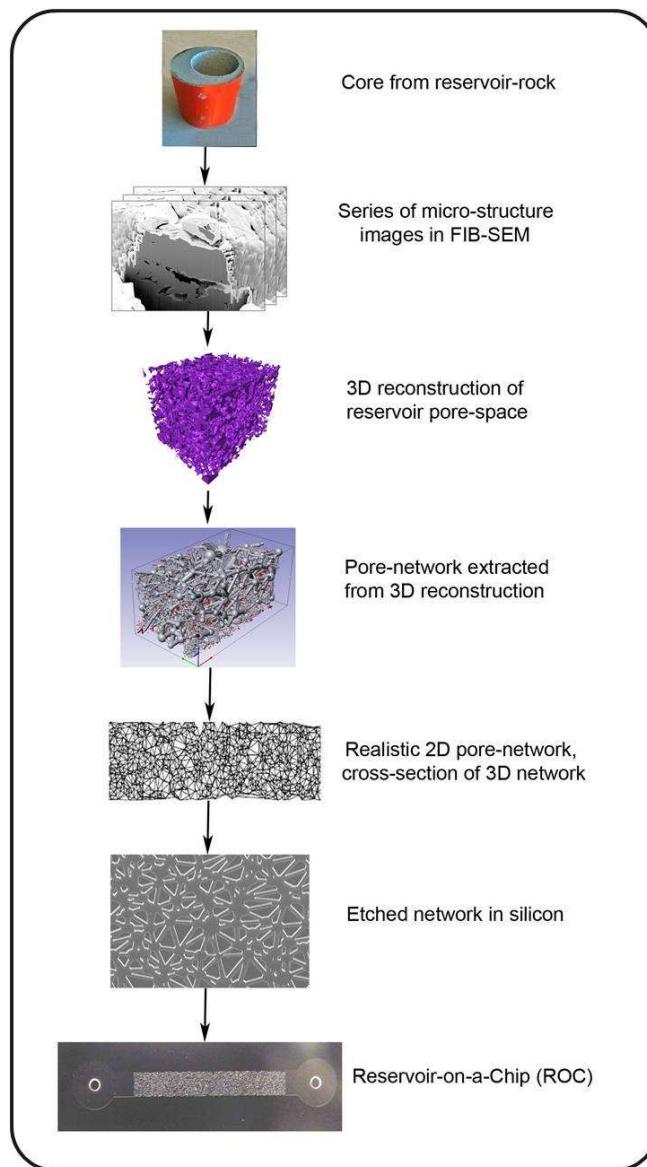


Figure 7.1 – The conceptual flow-map for ‘Reservoir-on-a-Chip’

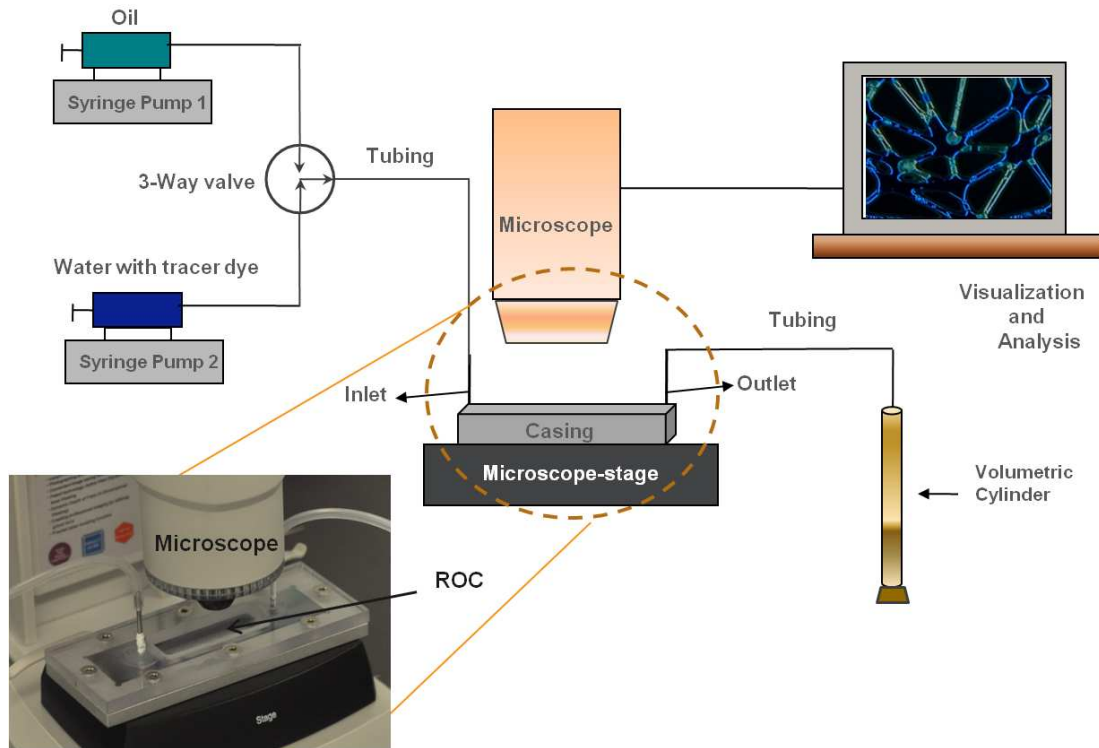


Figure 7.2 – Schematic of the experimental set-up used in performing water-flooding experiments with ROC; inset illustrates the magnified image of ROC housed in a casing, placed under the microscope for flow visualization experiments.

port within the network. M1 lubricant oil (L.S. Starrett Company, Athol, MA; specific gravity ~ 788 at 15.5° C, viscosity ~ 2.2 cSt) has been used as the oil phase to be displaced by water. For properly distinguishing the oil/water interface during the fluid transport, a blue tracer dye (Bright Dyes, Promag Enviro systems Inc., Burnaby, BC) is mixed with deionized water. Two syringe pumps (Harvard Apparatus, MA) have been used for controlling oil/water flow rates in this experiment. A 3-way valve is used to connect the syringe pumps to the inlet port of ROC, for selective injection of oil/water phases. For collecting the volume of displaced oil, a precision volumetric glass cylinder (Corning Inc., NY) is connected to the outlet of ROC for measuring the displaced oil from the ROC during waterflooding.

Using the syringe pump, oil is introduced in the ROC at a constant injection rate of $50 \mu\text{l}/\text{min}$ and continued until the chip is completely filled with oil.

Various ‘dead volumes’ in relation to the microfluidic connections and tubing are calculated. The total quantity of resident oil in the ROC is calculated by subtracting the dead volumes from the total injected oil volume. In the next step, DI water containing the tracer dye is injected at a rate of $100 \mu\text{l}/\text{min}$ in the ROC. In this process, water displaces the resident oil from the ROC. The volume of displaced oil is measured in the collecting cylinder and compared to the original volume of resident oil present in ROC.

7.3 Experimental Results

The images of waterflooding experiment have been taken at various places of the network and at different magnifications, in order to understand the average trend of fluid transport at these locations. Figure 7.3 shows a series of images at one such specific network location taken before and during waterflooding. Figure 7.3(a) shows the network completely filled with oil phase (denoted by the green color). Once waterflooding is initiated, oil slowly gets displaced due to the injection pressure and the water phase enters the network. Figure 7.3(b) is the image at the same location of the network at a later instant of time (5 min from the start of waterflooding), with the oil/water interfaces visible due to the optical contrast between oil and blue tracer dye. Green colour in the image represents oil phase, while blue colour represents water. Oil seems to be present in some pore-throats although invading water phase had already passed these locations. Hence, water is not able to displace oil from each pore and throat uniformly, which mimics the natural waterflooding process one observes in the reservoir-scale.

The oil/water interfaces at the same network location but at a later instant of time (13 min from the start of waterflooding) is shown in Fig.7.3(c). In this image, we notice the presence of similar characteristics of oil/water phases as in the previous figure. The detailed displacement process captured in the video shows that the velocity of oil displacement from throats has reduced with time. There are certain throats under observation, where the movement of the fluids is no longer occurring and stagnant phases of oil/water are noticed. The stagnant phases imply that those pockets of resident oil phases will not be displaced by water flooding alone and they require other tertiary or enhanced recovery schemes, as observed in a practical oil reservoir. The first drop of

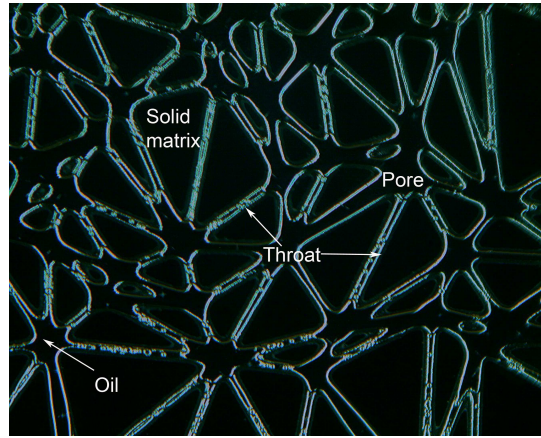
water at the ROC outlet is observed at the time instant, which corresponds to Fig.7.3(c). This process is often referred as ‘breakthrough’ in reservoir engineering. From that time onward, both water and oil phases are found at the outlet of ROC. Pockets of air are also present in the pore network, which could have been introduced during changing the source syringe pump in the 3-way valve. Figure 7.4 represents the oil/water phases present at another location in the network during the experiment, at a time-instant of 10 min from the start of waterflooding. Similar characteristics of displacement as that of the previous location can be observed, such as, stagnant phases in throats etc.

Based on the volume data of total displaced oil, the fraction of recovered oil is calculated. According to the design of the ROC, the total volume of inlet and the entrance region is considerably larger than the network volume. As a result, with the chosen injection rate of oil and water, we obtain laminar flow inside the network. A characteristic curve comparing the fraction of oil recovered with the injected water volume is presented in Fig.7.5. This plot is similar to a recovery curve in traditional core-flooding experiments. In this case, Original Oil in Place (OOIP) denotes the volume of oil inside ROC, before waterflooding starts. We observe a linear pattern at the beginning of waterflooding (up to about 500 μl of water injection), implying that the invading water phase displaces the resident oil in the same rate as its injection. However, as more volume of water is injected with time, the fraction of oil recovered is comparatively less, which has been explained in terms of trapped volume of oil. The maximum fraction of oil recovered by this stimulated waterflooding process is about 65%, which corresponds to values obtained in typical core-flooding experiments (Hadia et al., 2007).

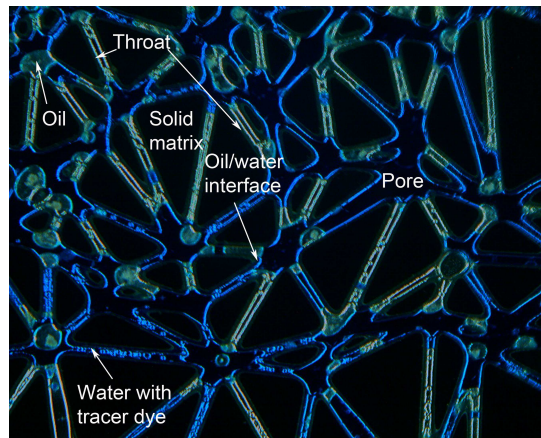
7.4 Concluding Remarks

A novel concept for miniaturization approach towards reservoir engineering and study of waterflooding techniques on a chip related to oil recovery has been presented in this work. Instead of the usual approach of core-flooding or experimentation in micro-models containing random pore-network representing porous medium, a methodology has been described where reservoir-rock is converted to a microfluidic chip for pore-scale study of oil displacement experiments. Sample core of such rock-specimen is characterized and reconstructed

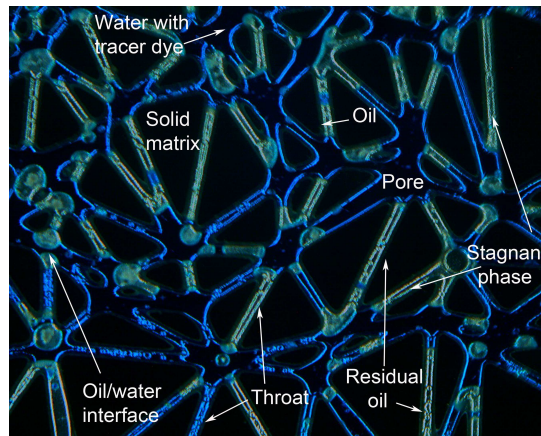
using advanced microscopy such as FIB-SEM. Based on this reconstruction, a pore network is designed and fabricated on silicon, which geometrically represents the real pore space. Various parameters such as mean pore size and depth of the network have been designed in a manner, such that this network is the most precise representation of an oil reservoir, and the term ‘Reservoir-on-a-Chip’ (ROC) for this fabricated microfluidic device has been coined. Waterflooding experiments have been performed in this ROC. It is observed that, invading water-phase cannot displace oil from all the pore-throats in the chip and oil remains as a stagnant phase at different locations. The analysis of recovery curve based on the fraction of oil recovered reveals similar type of oil-displacement pattern as obtained in a core-scale flooding experiment, which underlines the realization of the concept addressed in this study.



(a)



(b)



(c)

Figure 7.3 – Distribution of oil phase (green color) and water phase (blue color) in the pore network during waterflooding experiments. (a) The presence of oil phase at the start of the waterflooding process ($t=0$); (b) Relative positions of oil and water phases at $t = 5$ mins; (c) Relative positions of oil and water phases at $t = 13$ mins. The presence of trapped oil is observed at the later part of the waterflooding process

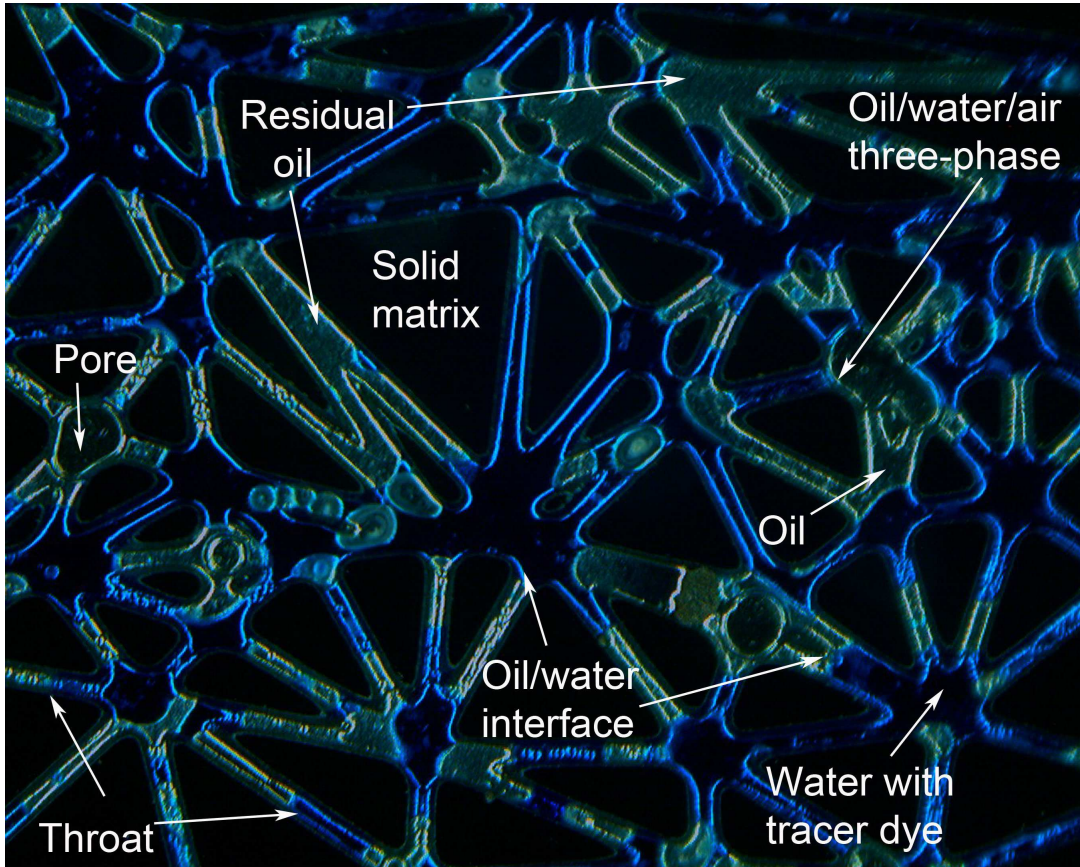


Figure 7.4 – A different section of the pore network capturing the same dynamics of the oil and water phases at $t = 10$ min.

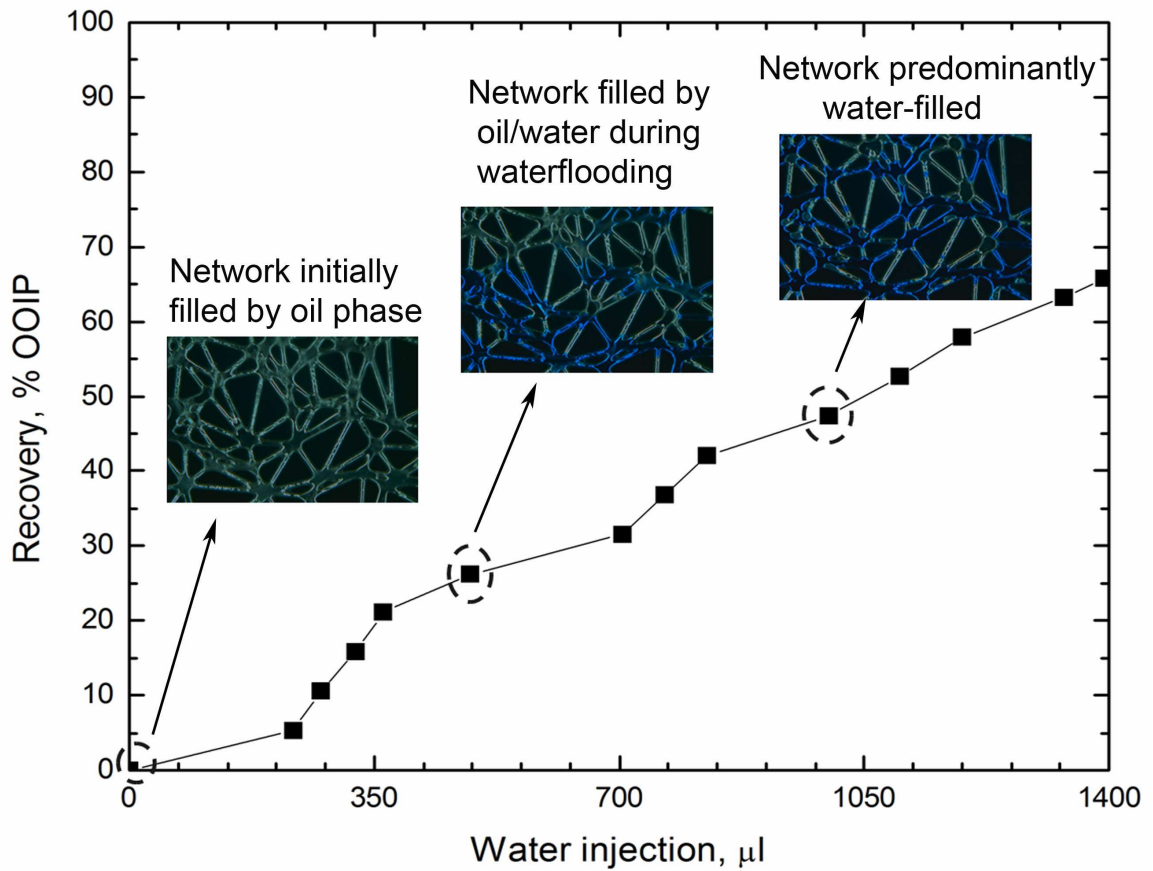


Figure 7.5 – Fraction of oil recovered in terms of original oil in place (OOIP) by injecting water at a constant flow rate of $100 \mu\text{l}/\text{min}$, which is analogous to recovery curve used in reservoir engineering (Hadia et al., 2007); Insets show images of oil (green colour)/water (blue colour) phases corresponding to different time instants during the waterflooding process.

Chapter 8

Conclusions and Future Work

In this chapter, the contribution of this study to the discipline of Enhanced Oil Recovery (EOR) is discussed with a few suggestions for future approaches based on ‘Reservoir-on-a-Chip’. Oil-bearing reservoir-rocks have been characterized in detail in this work. Various shortcomings and misleading natures of the already present methods of pore space definition are found out. Robust sample preparation methods along with state-of-the-art microscopy methods are established during the course of this study. Sandstone pore structures have been described with precise detailing of pore size and pore connectivity. Thus, the 3D reconstruction of sandstone pore space contains considerable amount of real information than contemporary studies. The major conclusion drawn from this part of the study is: pore structure smaller than 5-10 μm size is absent in Berea sandstone, and the solid matrix of this rock material is devoid of any submicron-scale pore within it.

A comprehensive sample preparation and characterization method has been developed for carbonate specimens. Though FIB-SEM has been used previously for such rock-structures, the resolution of image capturing and serial-sectioning techniques proposed in this work brings a significant difference to the final picture of the pore space. For the first time, nanometre-scale pores in dolomitic limestone are characterized and their evolution inside the rock-structure from nm to μm scale structure is tracked. As in the case of sandstone, the reconstruction signifies a very realistic representation of the dolomite rock structure, verified by comparing the calculated porosity of this pore space with the bulk porosity of dolomite specimens.

A series of pore networks has been designed, based on the characterizations of reservoir-cores and hence, resembles a real reservoir best. This pore network is realistic as the co-ordination number is high in the network design, and recent studies have proved that in real reservoir rocks, this number can be as high as 13. Microfabrication recipes have been categorically applied for silicon and quartz substrates individually, for most efficient pattern-transfer so that network data is not lost in the fabrication process. Unforeseen depth in quartz fabrication has been reported for such a complex series of networks, while the fabrication in silicon has been achieved with economical motive. The design of the depth of these networks enables one to perform fluid transport experiments in a porous medium equivalent of a real reservoir-rock. This novel miniaturization approach has been combined with methods of microfluidic connection, and a complete chip is fabricated. The device is a lab-scale representation of porous reservoir rock, and for the first time it is achieved with minimal change to the inherent pore-structure of such rock-cores.

‘Reservoir-on-a-Chip’ (ROC), fabricated on silicon, has been used for performing waterflooding experiments. Waterflooding and other investigations of oil-displacement in a fabricated micro-model have been attempted in literature, but based on the realistic nature of pore network in this microfluidic device, a recovery curve has been prepared from the oil-displacement data. It is observed that the primary outcome of the recovery curve signifies a pattern followed in core-scale flooding of reservoir-rocks. Hence, it can be concluded that the realization of ‘Reservoir-on-a-Chip’ has been demonstrated during the course of this study.

The following approaches would be relevant for future studies based on ‘Reservoir-on-a-Chip’:

1. Only single cores of sandstone and carbonate have been considered in this study, and based on that the reconstructions and subsequent characterizations have been performed. However, the porosity and pore distribution would vary in the rock cores depending on the place of their occurrence. Hence, studying more number of cores from a variety of sedimentary history with the methods proposed in this study would define a rock structure in more general manner. Hence, it would be possible to design pore network capturing wider

range of information.

2. The waterflooding experiments have been performed in silicon ROCs in this study, for a primary proof of concept. Quartz ROCs have been fabricated with the goal of superior visualization of fluid transport, and would be an interesting scope of further studies.

3. No surface treatment methods have been considered in this study. Actual reservoir-rocks influence the recovery of oil by their selective affinity to a certain fluid, and that can be simulated in various flooding experiments. Existing surface-treatment method can be applied to turn the ROC hydrophilic or hydrophobic and then compare the nature of oil recovery curves for these cases.

Bibliography

- R. Hazlett. Simulation of capillary-dominant displacements in microtomographic images of reservoir rocks. *Transport in Porous Media*, 20:21–35, 1995.
- J.R. Wilson, J.S. Cronin, A.T. Duong, Rukes, Chen S., H.-Y., K. Thornton, D.R. Mumm, and S. Barnett. Effect of composition of $\text{La}_{0.8}\text{Sr}_{0.2}\text{MnO}_3\text{-Y}_2\text{O}_3$ -stabilized ZrO_2 cathodes. correlating three-dimensional microstructure and polarization resistance. *Journal of Power Sources*, 195(7):1829–1840, 2010.
- R. Wirth. Focused ion beam (FIB) combined with SEM and TEM: Advanced analytical tools for studies of chemical composition, microstructure and crystal structure in geomaterials on a nanometre scale. *Chemical Geology*, 261(3-4):217–229, 2009.
- N.S.K. Gunda, H. Choi, A. Berson, B. Kenney, K. Karan, J.G. Pharoah, and S.K. Mitra. Focused ion beam-scanning electron microscopy on solid-oxide fuel-cell electrode: Image analysis and computing effective transport properties. *Journal of Power Sources*, 196(7):3592 – 3603, 2011.
- A. S. Al-Kharusi and M.J. Blunt. Network extraction from sandstone and carbonate pore space images. *Journal of Petroleum Science and Engineering*, 56(4):219 – 231, 2007.
- T. Ahmed. Principles of waterflooding. In *Reservoir Engineering Handbook (Fourth Edition)*, pages 909 – 1095. Gulf Professional Publishing, Boston, fourth edition edition, 2010.
- G.A. Pope. Application of fractional flow theory to enhanced oil recovery. *Society of Petroleum Engineers of AIME Journal*, 20(3):191–205, 1980.

- S.E. Buckley and M.C. Leverett. Mechanism of fluid displacement in sands. *Transactions of the American Institute of Mining and Metallurgical Engineers*, 146:107–116, 1942.
- S.P. Bigg and C.A. Koch. Water flooding of oil fields in wyoming. *US Bureau of Mines Reports*, 1970.
- F.F. Craig. The reservoir engineering aspects of water flooding. *New York American Institute of Minerals, Metallurgy and Petroleum Engineers Inc.*, 2:202–213, 1971.
- J.O. Jaber, S.D. Probert, and P.T. Williams. Evaluation of oil yield from Jordanian oil shales. *Energy*, 24(9):761 – 781, 1999.
- M. J. Kaiser. Hydrocarbon production forecast for committed assets in the shallow water outer continental shelf of the gulf of mexico. *Energy*, 34(11): 1813 – 1825, 2009.
- N. Mungan. Enhanced oil recovery using water as driving fluid. *World Oil*, 192:209–220, 1981.
- Y. Ghomian, G.A. Pope, and K. Sepehrnoori. Reservoir simulation of CO₂ sequestration pilot in Frio brine formation, USA Gulf Coast. *Energy*, 33(7): 1055 – 1067, 2008.
- K. Damen, A. Faaij, F. van Bergen, J. Gale, and E. Lysen. Identification of early opportunities for CO₂ sequestration–worldwide screening for CO₂-EOR and CO₂-ECBM projects. *Energy*, 30(10):1931 – 1952, 2005.
- S. G. Sayegh and D. B. Fisher. Enhanced Oil Recovery by CO₂ Flooding in Homogeneous and Heterogeneous 2D Micromodels. *Journal OF Canadian Petroleum Technology*, 48(8):30–36, 2009.
- V. Alvarado and E. Manrique. Enhanced Oil Recovery: An Update Review. *Energies*, 3(9):1529–1575, 2010.
- Q. Liu, M. Dong, S. Ma, and Y. Tu. Surfactant enhanced alkaline flooding for Western Canadian heavy oil recovery. *Colloids and Surfaces A: Physicochemical and Engineering Aspects*, 293(1-3):63 – 71, 2007.

- L. Thibodeau and G.H. Neale. Effects of connate water on chemical flooding processes in porous media. *Journal of Petroleum Science and Engineering*, 19(3-4):159–169, 1998.
- T. Babadagli. Development of mature oil fields - A review. *Journal of Petroleum Science and Engineering*, 57(3-4):221–246, 2007.
- C.E. Thomas, C.F. Mahoney, and G.W. Winter. *Petroleum Engineering Handbook*. Society of Petroleum Engineers, Dallas, 1989.
- D. Tiab and E.C. Donaldson. *Petrophysics: Theory and practice of measuring reservoir rock and fluid transport properties*. Gulf P, 2004.
- W. A. Kalender. X-ray computed tomography. *Physics In Medicine and Biology*, 51(13):R29–R43, 2006.
- S. J. Schambach, S. Bag, L. Schilling, C. Groden, and M. A. Brockmann. Application of micro-ct in small animal imaging. *Methods*, 50(1):2–13, 2010.
- E. Verges, D. Tost, D. Ayala, E. Ramos, and S. Grau. 3D pore analysis of sedimentary rocks. *Sedimentary Geology*, 234(1-4):109–115, 2011.
- X. F. Liu, J. M. Sun, and H. T. Wang. Reconstruction of 3-D digital cores using a hybrid method. *Applied Geophysics*, 6(2):105–112, 2009.
- C. H. Arns, F. Bauget, A. Ghous, A. Sakellariou, T. J. Senden, A. P. Sheppard, R. M. Sok, W. V. Pinczewski, J. C. Kelly, and M. A. Knackstedt. Digital core laboratory: Petrophysical analysis from 3D imaging of reservoir core fragments. *Petrophysics*, 46(4):260–277, 2005.
- M. L. Turner, L. Knufing, C. H. Arns, A. Sakellariou, T. J. Senden, A. P. Sheppard, R. M. Sok, A. Limaye, W. V. Pinczewski, and M. A. Knackstedt. Three-dimensional imaging of multiphase flow in porous media. *Physica A-Statistical Mechanics and Its Applications*, 339(1-2):166–172, 2004.
- H. Okabe and M.J. Blunt. Prediction of permeability for porous media reconstructed using multiple-point statistics. *Physical Review E*, 70(6):066135, 2004.
- K. Mogensen, E. H. Stenby, and D. E. Zhou. Studies of waterflooding in low-permeable chalk by use of x-ray ct scanning. *Journal of Petroleum Science and Engineering*, 32(1):1–10, 2001.

- J. Orloff. Focused ion beam characterization techniques. In K. H. Jrgen Buschow, Robert W. Cahn, Merton C. Flemings, Bernard Ilschner (print), Edward J. Kramer, Subhash Mahajan, , and Patrick Veysire (updates), editors, *Encyclopedia of Materials: Science and Technology*, pages 3226 – 3231. Elsevier, 2001.
- S. Barnett, J. Wilson, W. Kobsiriphat, H. Chen, R. Mendoza, J.M. Hiller, D. Miller, K. Thornton, P. Voorhees, and S. Adler. Three-dimensional analysis of solid oxide fuel cells using focused ion beam-scanning electron microscopy. *Journal of Microscopy Microanalysis*, 13:596–597, 2007.
- L. Holzer, B. Munch, M. Rizzi, R. Wepf, P. Marschall, and T. Graule. 3D-microstructure analysis of hydrated bentonite with cryo-stabilized pore water. *Applied Clay Science*, 47(3-4):330–342, 2010.
- E. Meyer, H. Hug, and R. Bennewitz. *Scanning Probe Microscopy: The Lab on a Tip*. Springer, 2004.
- D. Williams and C. Carter. *Transmission Electron Microscopy-a Text book for Materials Science*. Cambridge University Press, New York., 1996.
- E. Principe. *Focused Ion Beam system: Basics and Applications*. Plenum Press, Cambridge, UK., 2007.
- P. G. Kotula, M. R. Keenan, and J. R. Michael. Tomographic spectral imaging with multivariate statistical analysis: Comprehensive 3D microanalysis. *Microscopy and Microanalysis*, 12(1):36–48, 2006.
- J. Russ. *The Image Processing Handbook*. CRC Press, Boca Raton, Florida. third edition., 1999.
- R. Gonzales and R. Woods. *Digital Image Processing*. Prentice Hall, New Jersey. second edition., 2002.
- J. R. Wilson, W. Kobsiriphat, R. Mendoza, H. Y. Chen, J. M. Hiller, D. J. Miller, K. Thornton, P. W. Voorhees, S. B. Adler, and S. A. Barnett. Three-dimensional reconstruction of a solid-oxide fuel-cell anode. *Nature Materials*, 5(7):541–544, 2006.
- B. Adams, S. Wright, and K. Kunze. Orientation imaging: The emergence of a new microscopy. *Metallurgy Transactions A*, 24:819–831, 1993.

- R. Schwarzer. Automated crystal lattice orientation mapping using a computer-controlled sem. *Micron*, 24:249–265, 1997.
- A. Bastos, S. Zaefferer, and D. Raabe. Three-dimensional EBSD study on the relationship between triple junctions and columnar grains in electrodeposited Co-Ni films. *Journal of Microscopy*, 230:497–498, 2008.
- J. Konrad, S. Zaefferer, and D. Raabe. Investigation of orientation gradients around a hard laves particle in a warm-rolled fe3al-based alloy using a 3d ebsd-fib technique. *Acta Materialia*, 54(5):1369–1380, 2006.
- M. Calcagnotto, D. Ponge, E. Demir, and D. Raabe. Orientation gradients and geometrically necessary dislocations in ultrafine grained dual-phase steels studied by 2D and 3D EBSD. *Materials Science and Engineering A-structural Materials Properties Microstructure and Processing*, 527(10-11):2738–2746, 2010.
- N. Zaafarani, D. Raabe, R. Singh, F. Roters, and S. Zaefferer. Three dimensional orientation microscopy in a focused ion beam-scanning electron microscope: A new dimension of microstructure characterization. *Metal. Mater. Trans. A*, 39:1863–1876, 2006.
- L. Holzer, F. Indutnyi, P. H. Gasser, B. Munch, and M. Wegmann. Three-dimensional analysis of porous BaTiO₃ ceramics using FIB nanotomography. *Journal of Microscopy-oxford*, 216:84–95, 2004.
- L. Tomutsa and D.T. Silin. Nanoscale pore imaging and pore scale fluid flow modeling in chalk. *Lawrence Berkeley National Laboratory*, 2004.
- C.H. Sondergeld, R.J. Ambrose, C.S. Rai, and J. Moncrieff. Microstructural studies of gas shales. In *SPE Unconventional Gas Conference Pittsburgh, Pennsylvania*,, 2010.
- M.A. Knackstedt, S. Latham, M. Madadi, A. Sheppard, and T. Varslot. Digital rock physics: 3D imaging of core material and correlations to acoustic and flow properties. *Leading Edge*, 28:28–33, 2009.
- H.J. Lemmens, A.R. Butcher, and P.W.S.K. Botha. FIB/SEM and automated mineralogy for core and cuttings analysis. In *Russian Oil and Gas Technical Conference and Exhibition Moscow, Russia*, 2010.

- I. Fatt. The Network Model of Porous Media.1. Capillary Pressure Characteristics. *Transactions of the American Institute of Mining and Metallurgical Engineers*, 207(7):144–159, 1956a.
- I. Fatt. The Network Model of Porous Media.3. Dynamic Properties of Networks With Tube Radius Distribution. *Transactions of the American Institute of Mining and Metallurgical Engineers*, 207(7):164–181, 1956b.
- I. Fatt. The Network Model of Porous Media.2. Dynamic Properties of A Single Size Tube Network. *Transactions of the American Institute of Mining and Metallurgical Engineers*, 207(7):160–163, 1956c.
- P.E. Oren, S. Bakke, and O.J. Arntzen. Extending predictive capabilities to network models. *Society of Petroleum Engineers Journal*, 3:324–336, 1998.
- T.R. Lerdahl, P.E. Oren, and S. Bakke. A predictive network model for three-phase flow in porous media. In *Proceedings of the SPE/DOE Symposium on Improved Oil Recovery, Tulsa, OK*, 2000.
- V. Mani and K.K. Mohanty. Pore-level network modeling of three-phase capillary pressure and relative permeability curves. *Society of Petroleum Engineers Journal*, 3:238–248, 1998.
- D. H. Fenwick and M. J. Blunt. Three-dimensional modeling of three phase imbibition and drainage. *Advances In Water Resources*, 21(2):121–143, 1998.
- M.J. Blunt. Physically-based network modeling of multiphase flow in intermediate-wet porous media. *Journal of Petroleum Science and Engineering*, 20:117–125, 1998.
- D. Zhou, L.A. Dillard, and M.J. Blunt. A physically based model of dissolution of nonaqueous phase liquids in the saturated zone. *Transport in Porous Media*, 39:227–255, 2000.
- R.G. Hughes and M.J. Blunt. Network modeling of multiphase flow in fractures. *Advances in Water Resources*, 24(3-4):409 – 421, 2001.
- A.B. Dixit, S.R. McDougall, K.S. Sorbie, and J.S. Buckley. Pore-scale modeling of wettability effects and their influence on oil recovery. *SPE Reservoir Eval Eng*, 2:25–36, 1999.

- S. Oveysi and M. Pini. Direct pore-level modeling of incompressible fluid flow in porous media. *Journal of Computational Physics*, 229(19):7456–7476, 2010.
- Y. Zaretskiy, S. Geiger, K. Sorbie, and M. Forster. Efficient flow and transport simulations in reconstructed 3D pore geometries. *Advances In Water Resources*, 33(12):1508–1516, 2010.
- M.J. Blunt. Flow in porous media – pore-network models and multiphase flow. *Current Opinion in Colloid & Interface Science*, 6(3):197 – 207, 2001.
- H. Dong and M.J. Blunt. Pore-network extraction from micro-computerized-tomography images. *Physical Review E*, 80:0363071–11, 2009.
- G. Lovoll, Y. Meheust, K. J. Maloy, E. Aker, and J. Schmittbuhl. Competition of gravity, capillary and viscous forces during drainage in a two-dimensional porous medium, a pore scale study. *Energy*, 30(6):861–872, 2005.
- N. Hadia, L. Chaudhari, A. Aggarwal, S. K. Mitra, M. Vinjamur, and R. Singh. Experimental and numerical investigation of one-dimensional waterflood in porous reservoir. *Experimental Thermal and Fluid Science*, 32(2):355–361, 2007.
- P. van Zant. *Microchip Fabrication*. McGraw-Hill Publishers, New York, 2006.
- M. Datta and D. Landolt. Fundamental aspects and applications of electrochemical microfabrication. *Electrochimical Acta*, 45:2535–2558, 2000.
- L.T. Romankiw. A path: from electroplating through lithographic masks in electronics to liga in mems. *Electrochimical Acta*, 42:2985–3005, 1997.
- B. Lochel, A. Maciossek, H. J. Quenzer, and B. Wagner. Ultraviolet depth lithography and galvanofoming for micromachining. *Journal of the Electrochemical Society*, 143(1):237–244, 1996.
- W.J. Lloyd and H.H. Taub. *Output Hardcopy Devices*. Academic Press, NY, 1988.
- A. Chatnever and J.C. Calhoun Jr. Visual examinations of fluid behaviour in porous media:part 1. *Petroleum Transactions, AIME*, 149-156:1952, 195.

- J. Bonnet and R. Lenormand. Constructing micromodels for study of multiphase flow in porous-media. *Revue De L Institut Francais Du Petrole*, 32(3):477–480, 1977.
- R. Lenormand, E. Touboul, and C. Zarcone. Numerical-models and experiments on immiscible displacements in porous-media. *Journal of Fluid Mechanics*, 189:165–187, 1988.
- R. Lenormand and C. Zarcone. Capillary fingering - percolation and fractal dimension. *Transport In Porous Media*, 4(6):599–612, 1989.
- R. Lenormand. Applications of fractal concepts in petroleum engineering. *Physica D*, 38(1-3):230–234, 1989.
- S. Martinoia, M. Bove, M. Tedesco, B. Margesin, and M. Grattarola. A simple microfluidic system for patterning populations of neurons on silicon micro-machined substrates. *Journal of Neuroscience Methods*, 87(1):35–44, 1999.
- R.L. Smith, D.J. Fulmer, and S.D. Collins. Electrochemical microfabrication. *Proceedings of The Electrochemical Society, Princeton, NJ*, 92:203, 1992.
- D. Hoffman, J. OBrien, D. Brennan, and M. Loughran. Optically encoded silicon microbeads:detection and characterisation in a microfluidic system. *Sensors and Actuators B*, 122:653–658, 2007.
- Y. Suzuki, M. Yamada, and M. Seki. Sol-gel based fabrication of hybrid microfluidic devices composed of pdms and thermoplastic substrates. *Sensors and Actuators B: Chemical*, 148(1):323 – 329, 2010.
- Z. Zhang, P. Zhao, and G. Xiao. The fabrication of polymer microfluidic devices using a solid-to-solid interfacial polyaddition. *Polymer*, 50(23):5358 – 5361, 2009.
- L. Romoli, G. Tantussi, and G. Dini. Experimental approach to the laser machining of pmma substrates for the fabrication of microfluidic devices. *Optics and Lasers in Engineering*, 49(3):419 – 427, 2011.
- C. Perrin, P. Tardy, K. Sorbie, and J. Crawshaw. Experimental and modeling study of newtonian and nonnewtonian fluid flow in pore network micromodels. *Journal of Colloid and Interface Science*, 295:542–550, 2006.

- M. Ferer, G.S. Bromhal, and D.H. Smith. Crossover from capillary fingering to compact invasion for two-phase drainage with stable viscosity ratios. *Advances in Water Resources*, 30(2):284 – 299, 2007.
- M. Fuerstman, P. Deschateles, R. Kane, P. Schwartz, A.. Kenis, J. Deutch, and G. Whitesides. Solving mazes using microfluidic networks. *Langmuir*, 19:4714–4722, 2003.
- C. U. Hatiboglu and T. Babadagli. Experimental and visual analysis of diffusive mass transfer between matrix and fracture under static conditions. *Journal of Petroleum Science and Engineering*, 74(1-2):31–40, 2010.
- P. E. Oren and W. V. Pinczewski. Fluid distribution and pore-scale displacement mechanisms in drainage dominated 3-phase flow. *Transport In Porous Media*, 20(1-2):105–133, 1995.
- M. I. J. van Dijke, K. S. Sorbie, A. Sohrabi, and A. Danesh. Simulation of wagg floods in an oil-wet micromodel using a 2-D pore-scale network model. *Journal of Petroleum Science and Engineering*, 52(1-4):71–86, 2006.
- D. Broseta, F. Medjahed, J. Lecourtier, and M. Robin. Polymer adsorption/retention in porous media: effects of core wettability and residual oil. *SPE Adv. Technol. Ser.*, 3:103–112, 1995.
- H. M. Meybodi, R. Kharrat, and X. Wang. Study of microscopic and macroscopic displacement behaviours of polymer solution in water-wet and oil-wet media. *Transport In Porous Media*, DOI 10.1007/s11242, 2011.
- V. Berejnov, N. Djilali, and D. Sinton. Lab-on-chip methodologies for the study of transport in porous media: energy applications. *Lab On A Chip*, 8(5):689–693, 2008.
- C.L. Perrin, H. Watt-U, K.S. Sorbie, and P.M.J. Tardy. Micro-piv: A new technology for pore scale flow characterisation in micromodels. In *SPE Europepec/EAGE Annual Conference, Madrid, Spain*, 2005.
- A.C. Gunde, B. Bera, and S.K. Mitra. Investigation of water and CO₂ flooding using micro-CT images of Berea sandstone core by Finite Element Method. *Energy*, 35:5209–5216, 2010.

- B. Bera, N.S.K. Gunda, N.K. Karadimitriou, S.K. Mitra, and S.M. Hasanizadeh. Reservoir-on-a-Chip (ROC): A new paradigm in Reservoir Engineering. *Lab On A Chip*, LC-ART-06-2011-020556, 2011a.
- B. Bera, N.S.K. Gunda, S.K. Mitra, and D. Vick. Characterization of nanometre-scale porosity in reservoir carbonate rock by Focused Ion Beam-Scanning Electron Microscopy (FIB-SEM). *Journal of Microscopy and Microanalysis*, MAM-11-083, 2011b.
- B. Bera, N.S.K. Gunda, and S.K. Mitra. Fabrication of pore-network structures in silicon and quartz substrates. *Journal of Micromechanics and Micromachining*, JMM/394050/PAP/166956, 2011c.
- B. Bera, S.K. Mitra, and D. Vick. Understanding the microstructure of berea sandstone by the simultaneous use of micro-computed tomography (micro-CT) and focused ion beam-scanning electron microscopy (FIB-SEM). *Micron*, 42:412–418, 2011d.
- J. Goldstein, D. Newbury, D. Joy, C. Lyman, P. Echlin, E. Lifshin, L. Sawyer, and J. Michael. *Scanning Electron Microscopy and X-Ray Microanalysis*. Plenum Publishers, New York, 2003.
- R.L. Panton. *Incompressible Flow*. John Wiley & Sons, 2005.
- J.U. Brackbill, D.B. Kothe, and C. Zemach. A continuum method for modeling surface tension. *Journal of Computational Physics*, 100:335–354, 1992.
- O. Schenk and K. Gartner. Solving unsymmetric sparse systems of linear equations with pardiso. *Future Generation Computer*, 20:475–487, 2004.
- A. A. Heiba, M. Sahimi, L. E. Scriven, and H. T. Davis. Percolation theory of two-phase relative permeability. *Chem. Eng. Sci.*, 41:2123–2136, 1986.
- H. K. Dahle and M. A. Celia. A dynamic network model for two-phase immiscible flow. *Computational Geosciences*, 3:1–22, 1999.
- D.L. Keefer and S.E. Bodily. Three-point approximations for continuous random variables. *Management Science*, 29:595–609, 1983.